Novel hydrogeologic characterization methods: utilizing the analytic element method in hydrogeophysical studies

by

Weston Koehn

B.S., Kansas State University, 2014

AN ABSTRACT OF A DISSERTATION

submitted in partial fulfillment of the requirements for the degree

DOCTOR OF PHILOSOPHY

Department of Civil Engineering
College of Engineering

KANSAS STATE UNIVERSITY
Manhattan, Kansas

2020

Abstract

An accurate conceptualization of groundwater-surface water connectivity is critical for quantification of fluxes between rivers and aquifers. Point based hydrologic data provides a useful indicator to delineate an aquifers response to changes in streamflow; however, supplementary hydrogeologic information is often needed to fully constrain connectivity patterns due to the presence of focused recharge pathways. Electrical resistivity tomography (ERT) is a near surface geophysical method that determines the electrical resistivity distribution within the earth. Electrical resistivity is an intrinsic material property that is strongly correlated to hydrogeologic properties (e.g., water content, porosity, pore fluid salinity, clay content). The spatial and temporal distribution of electrical resistivity provides insight into the hydrologic state of sediments. Ultimately, changes in electrical resistivity across space and time provide of level of understanding about hydrogeologic processes that is unmatched by the analysis of point based hydrologic measurements alone. ERT surveys were conducted along the Arkansas River in Western Kansas to depict the hydrologic state of riverbed sediments, and to gain insight on the hydrologic response of the sediments across changes in streamflow and the hydrogeologic landscape. The electrical resistivity profiles revealed large contrasts in resistivity beneath portions of the inundated riverbed, indicating different regimes of groundwater-surface water (gw-sw) connectivity persist both spatially and temporally. Although the initial results of the study indicated that ERT can be used to observe differences in gw-sw connectivity through time and space, a more rigorous hydrogeologic interpretation of ERT surveys is needed to bridge the gap between quantitative groundwater models and the information provided by geophysical earth models. This motivated the inclusion of the Analytic Element Method (AEM) into geophysical inversion and ERT survey design to further advance the ability of near surface geophysics to fully exploit the hydrogeologic information inherent geophysical data. Electrical conduction through soil was modelled using the AEM. Soil was represented using interconnected rectangular elements, each with a constant electrical resistivity. The

forward response of an ERT array was generated over layered resistivity models. The AEM model matched electrostatic boundary an interface conditions to high accuracy for lowly and highly resistivity layers, as well as for isolated inclusions within uniform backgrounds. The implementation of a particle swarm optimization scheme was used to reconstruct resistivity models from synthetic data, which were in good agreement with the known model within the theoretical depths investigation of the simulated array. Resistivity models constructed from field data were highly dependent on the norm used. Simulations that used the root mean square percentage error as the norm significantly underestimated the voltage potentials measured near the source pair. This is attributed to the fact that voltage potentials measured at large dipole separations can potentially be given a higher weight as the residual is normalized by the true value, which can be small for large arrays. Simulations using the root mean square error (RMSE) as the norm produced 1D resistivity models whose response better matched the voltage potentials derived from low dipole separations. The RMSE heavily penalizes larger residuals, thus, the RMSE simulations provided solutions whose responses better match observations calculated at small dipole separations (larger voltage potentials) as more importance was placed on matching larger voltage measurements. The significance of this research in regards to advancing geophysical inversion techniques is two fold. The first significant contribution is that the numerical accuracy of AEM solutions are not dependent upon the discretization of a computational grid, thus, a complex discretization is not required to achieve a sound hydrogeologic interpretation of ERT data unless necessitated by the data. Although the earth is inherently complex, a finely discretized model leads to a large number of parameters that need to be estimated. An equally good explanation of the subsurface may be provided by analytic elements, removing the requirement of finely discretized regions to achieve numerical stability. The second major contribution is that the RMSE or MAE should be used as the norm for models using a single objective function to provide the most realistic representation of earth models. Ultimately, the AEM-PSO scheme improves the hydrogeologic information that can be inferred from ERT data, and furthers the ability of ERT to serve as an effective in-situ hydrogeologic characterization method.

Novel hydrogeologic characterization methods: utilizing the analytic element method in hydrogeophysical studies

by

Weston J Koehn

B.S., Kansas State University, 2014

A DISSERTATION

submitted in partial fulfillment of the requirements for the degree

DOCTOR OF PHILOSOPHY

Department of Civil Engineering
College of Engineering

KANSAS STATE UNIVERSITY
Manhattan, Kansas

2020

Approved by:

Co-Major Professor
Stacey E. Tucker-Kulesza

Approved by:

Co-Major Professor
David R. Steward

Copyright

Abstract

An accurate conceptualization of groundwater-surface water connectivity is critical for quantification of fluxes between rivers and aquifers. Point based hydrologic data provides a useful indicator to delineate an aquifers response to changes in streamflow; however, supplementary hydrogeologic information is often needed to fully constrain connectivity patterns due to the presence of focused recharge pathways. Electrical resistivity tomography (ERT) is a near surface geophysical method that determines the electrical resistivity distribution within the earth. Electrical resistivity is an intrinsic material property that is strongly correlated to hydrogeologic properties (e.g., water content, porosity, pore fluid salinity, clay content). The spatial and temporal distribution of electrical resistivity provides insight into the hydrologic state of sediments. Ultimately, changes in electrical resistivity across space and time provide of level of understanding about hydrogeologic processes that is unmatched by the analysis of point based hydrologic measurements alone. ERT surveys were conducted along the Arkansas River in Western Kansas to depict the hydrologic state of riverbed sediments, and to gain insight on the hydrologic response of the sediments across changes in streamflow and the hydrogeologic landscape. The electrical resistivity profiles revealed large contrasts in resistivity beneath portions of the inundated riverbed, indicating different regimes of groundwater-surface water (gw-sw) connectivity persist both spatially and temporally. Although the initial results of the study indicated that ERT can be used to observe differences in gw-sw connectivity through time and space, a more rigorous hydrogeologic interpretation of ERT surveys is needed to bridge the gap between quantitative groundwater models and the information provided by geophysical earth models. This motivated the inclusion of the Analytic Element Method (AEM) into geophysical inversion and ERT survey design to further advance the ability of near surface geophysics to fully exploit the hydrogeologic information inherent geophysical data. Electrical conduction through soil was modelled using the AEM. Soil was represented using interconnected rectangular elements, each with a constant electrical resistivity. The

forward response of an ERT array was generated over layered resistivity models. The AEM model matched electrostatic boundary an interface conditions to high accuracy for lowly and highly resistivity layers, as well as for isolated inclusions within uniform backgrounds. The implementation of a particle swarm optimization scheme was used to reconstruct resistivity models from synthetic data, which were in good agreement with the known model within the theoretical depths investigation of the simulated array. Resistivity models constructed from field data were highly dependent on the norm used. Simulations that used the root mean square percentage error as the norm significantly underestimated the voltage potentials measured near the source pair. This is attributed to the fact that voltage potentials measured at large dipole separations can potentially be given a higher weight as the residual is normalized by the true value, which can be small for large arrays. Simulations using the root mean square error (RMSE) as the norm produced 1D resistivity models whose response better matched the voltage potentials derived from low dipole separations. The RMSE heavily penalizes larger residuals, thus, the RMSE simulations provided solutions whose responses better match observations calculated at small dipole separations (larger voltage potentials) as more importance was placed on matching larger voltage measurements. The significance of this research in regards to advancing geophysical inversion techniques is two fold. The first significant contribution is that the numerical accuracy of AEM solutions are not dependent upon the discretization of a computational grid, thus, a complex discretization is not required to achieve a sound hydrogeologic interpretation of ERT data unless necessitated by the data. Although the earth is inherently complex, a finely discretized model leads to a large number of parameters that need to be estimated. An equally good explanation of the subsurface may be provided by analytic elements, removing the requirement of finely discretized regions to achieve numerical stability. The second major contribution is that the RMSE or MAE should be used as the norm for models using a single objective function to provide the most realistic representation of earth models. Ultimately, the AEM-PSO scheme improves the hydrogeologic information that can be inferred from ERT data, and furthers the ability of ERT to serve as an effective in-situ hydrogeologic characterization method.

Contents

List of Figures

List of Tables

Acknowledgments

Firstly, I would like to thank my co-advisors, Dr. David R. Steward and Dr. Stacey E. Tucker-Kulesza. The work I performed in this dissertation is an extension of the technical training I have received from them. Their patience, mentorship, and continued support allowed me to navigate through this humbling journey, for which I will be ever grateful.

Secondly, I would like to thank my mother, Sondra J. Koehn. Sondra was an instrumental part of the field work conducted in Western Kansas, and I could not have done it without her willingness to step forward and help. I know she enjoyed our time out by the Ark river and walking through the Tamarisk bushes with all the resistivity equipment. Thirdly, I would like to thank my father, Danny J. Koehn. I ascribe my work ethic and fierce determination to him, and sincerely appreciate the continued words of support he provided me with. Fourthly, I would like to thank my brother, Heath A. Koehn. His colorful personality and whimsical sense of humor often reminded me of the joys in life.

Lastly and most importantly, I would like to thank, Keri A. Heston ("Koehn" to be someday because my first name can't rhyme with my last name) for the constant support and encouragement she has provided me with through this arduous journey. She has spent countless hours at night listening to me ramble on about who knows what. Thank you for always being there to celebrate my achievements and to pick me up during times of despair.

Chapter 1

Introduction

Groundwater depletion is a globally occurring problem that inhibits ecosystems to sustain services they provide to all of humanity. The impact of declining groundwater levels across the High Plains Aquifer region have been manifested through decreased magnitudes of streamflow as the dynamic relationship exhibited by groundwater and surface water is directly linked to the rate and extent of groundwater depletion (Whittemore, 2002). River systems have transitioned from perennial to ephemeral flows in many areas overlying the High Plains Aquifer where the rate of groundwater withdrawals exceed natural recharge (Whittemore, 2002). This is especially true across western Kansas along the Arkansas River and Cimarron River, where losing conditions predominate as a result of declining groundwater levels adjacent to these rivers (Auvenshine, 2018). Although Steward and Allen (2016) established the mechanisms and driving forces of groundwater depletion within this region, the understanding of how groundwater and surface water interact through time and space is less understood.

The overarching goal of this research is to improve the understanding of how groundwater and surface water interact across different hydrologic settings using ERT surveys and a novel two-dimensional inversion scheme utilizing the analytic element method (AEM) and a particle swarm optimization (PSO) scheme. A review of pertinent literature regarding ERT and the AEM is first provided in Chatper 2 to explain current inversion strategies and traditional applications of the AEM. The hydrogeologic characterization of the study area is given in Chapter 3, along with the hydrogeologic understanding provided by ERT surveys. The temporal analysis of ERT surveys using commercial geophysical inversion software is outline in Chapter 4. Chapter 5 presents the methods used to conduct ERT surveys, along with the numerical treatment of the inverse problem using the AEM-PSO scheme. Chapter 6 demonstrates how the Analytic Element Method (AEM) can be used to accurately deduce the response of electrical fields within the earth across various hydrogeologic environments. Chapter 7 examines the ability of a global optimization scheme (Particle Swarm Optimization) to reproduce layered resistivity models for synthetic and field data, and explores the impact different objective functions have on recovered models. Ultimately, the improved interpretation of electrical resistivity tomography (ERT) surveys in regards to hydrogeologic properties facilitates our ability characterize governing mechanisms of focused recharge through riverbeds where hydrologic data is difficult to collect. This is significant to hydrologic studies aimed at improving the conceptualization of groundwater-surface water (gw-sw) exchange mechanisms (Nyquist et al., 2008; Brownbill et al., 2011; Koehn et al., 2019). Additionally, the ability to design ERT survey configurations to better image geologic structures is relevant in geotechnical engineering (Merritt et al., 2014; Karim and Tucker-Kulesza, 2018; Tucker-Kulesza et al., 2019), and geoenvironmental engineering (Ogilvy et al., 2002; Kemna et al., 2002).

In situ characterization of hydraulic properties at the riverbed scale provides information about the prevailing state of gw-sw connection regimes, and the mechanisms governing the gw-sw exchange fluxes. Focused recharge through riverbeds is difficult to characterize from point-based hydrologic data. The response of an aquifer adjacent to a surface water feature may not be informative of the true hydrologic conditions between the streambed and groundwater table (Brunner et al., 2017). Figure 1.1 shows two hydrogeologic conceptualizations of the river-aquifer system along the Arkansas River in western Kansas.

Although monitoring wells adjacent to a river, as shown in Figure 1.1, may provide information about the aquifer response to streamflow, there is still a lack of information regarding the hydrogeologic state of sediments between the riverbed and groundwater table. With a push to develop more process-based models of gw-sw exchanges (e.g.,Brunner et al. (2017)), there is a clear need to develop in situ characterization techniques capable of distinguishing the governing mechanisms of gw-sw exchange where focal points of recharge occur. Electrical resistivity is an intrinsic ma-

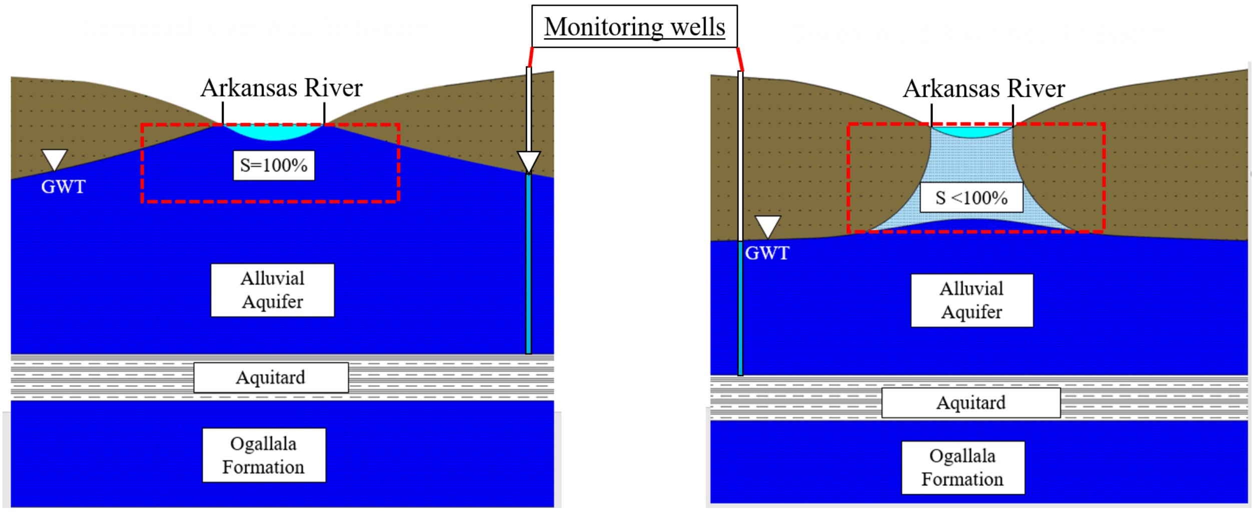

Figure 1.1: Two hydrogeologic conceptualizations of the Arkansas River and underlying aquifer units.

terial property which quantifies how strongly a material can oppose the flow of electrical current. Hydrogeologic and environmental factors such as the water content, porosity, salinity, clay content, pore geometry, and pore-fluid temperature control the electrical resistivity soil and rock (Everett, 2013). The application of near surface geophysics in hydrological studies has become increasingly popular over the past two to three decades, particularly to studies aimed at characterizing the interactions between groundwater and surface water (Binley et al., 2015; Robinson et al., 2008). Numerous studies have used ERT to characterize groundwater systems (Descloitres et al., 2008; Nyquist et al., 2008; Schwartz and Schreiber, 2009; Crook et al., 2008). ERT surveys can supplement direct observations of hydrologic state variables (i.e., hydraulic head, piezometric head) to improve the understanding of how soil and hydraulic properties vary spatially (e.g., (Chaudhuri et al., 2013)). Although well established and highly effective for many geological systems, traditional numerical methods utilized in the processing of geophysical data have a limited ability to detect sharp soil heterogeneities at the field scale as a result of numerical deficiencies associated with standard inversion procedures (Loke et al., 2003). More specifically, a sharp change in a physical property (e.g., hydraulic conductivity) may require the computational grid in a discretized method to be altered. This can lead to significant increases in computing requirements and inaccuracies in the local solution if an insufficient number of elements are utilized. Haitjema et al. (2001) demonstrated this for groundwater flow when comparing the results of MODFLOW to exact solutions. Results showed that flow pedictions near localized recharge sources were highly dependent upon the cell size used, and that small cell sizes are needed to accurately predict groundwater flow rates and travel times. This same notion applies to the numerical simulation of electric current flow. The impact of cell size on not only the numerical accuracy of forward simulations, but on the recovered model generated from the inversion process has been well documented in classic geophysical literature (e.g.,(Loke et al., 2003; Constable et al., 1987)) that is still relevant today. However, few studies to date have explored the benefits using of a grid free method, such as the AEM, in geophysical inversion. Therefore, this dissertation is geared towards the advancement geophysical inversion by utilizing the AEM, which provides a mathematically robust foundation for electrical conduction through various soil settings.

The Analytic Element Method was developed by Otto Strack in the 1970s, and is mainly utilized for modelling groundwater systems (Haitjema, 1995; Strack, 2003; Hunt, 2006; Steward and Allen, 2013; Steward, 2015, 2020a). Other applications include vadose zone modelling (Bakker and Nieber, 2004; Steward, 2016), and coastal hydraulics (Steward, 2018, 2020b). The AEM provides near exact solutions to boundary value problems, and the solution accuracy is independent of discretization. The research reported here utilizes the AEM to simulate electrical conduction through rectangular soil elements through the superposition of analytic solutions. Rectangle boundary and interface conditions are matched to high accuracy by utilizing robust mathematical formulations called influence functions that surpass the ability of traditional simulation methods distribute sharp gradients in potential fields. The PSO framework provides the ability to reduce the model dependency on the initial parameterization, and to exploit the global solution within a highly complex parameter space. A strength of the AEM is its ability to incorporate local details into a large model domain without altering the computational grid (Hunt, 2006). The ability of the AEM to handle local discontinuities across multiple scales is demonstrated in Chapter 6.

Although it is not the goal of this study to provide a direct relationship between hydrologic state variables and geophysical properties, the power of the AEM in hydrogeophysical applications may mitigate some of the uncertainty associated with inferring hydrologic information form near surface geophysical data. The AEM provides the ability to obtain more realistic representations of subsurface hydrogeologic conditions from ERT data, which advances the ability to conceptualize gw-sw exchange mechanisms when coupled with hydrologic data. Additionally, the AEM also provides a numerically robust method to improve the design of ERT surveys to better depict relevant subsurface features.

Chapter 2

Literature Review

2.1 Electrical Resistivity Tomography

Electrical resistivity tomography (ERT) is a near surface geophysical method that is used to to determine the resistivity distribution of the subsurface. The primary uses of ERT include but are not limited to site characterization, groundwater investigations, environmental studies, and archealogical studies (Everett, 2013). The primary use of ERT in this study is geared towards developing a better understanding of groundwater-surface water (gw-sw) connectivity regimes and riverbed hydrogeology.

The governing equations of electrostatics are now introduced to show their relationship to the governing DC resistivity problem. These equations are expanded upon later as they are implemented with the AEM. The flow of electrical current is governed by Ohm's Law

$$V = IR\frac{A}{L} \tag{2.1}$$

where V is voltage in volts, I is current in Amperes, R is the resistance in Ohms, A is the cross sectional area of the conducting surface, and L is the length of the conducting surface. Electrical resistivity, ρ, is an intrinsic material property that quantifies a materials ability to resist the flow of electrical current. Electrical resistivity serves as constant of proportionality and is related to the resistance of material

$$\rho = R\frac{A}{L} \tag{2.2}$$

where all variables have been previously defined. The electrical conductivity σ is the reciprocal of the electrical resistivity. Ohm's law can also be written in the following fundamental form

$$\vec{J} = \sigma\vec{E} \tag{2.3}$$

where $\vec{J}$ is the current density and $\vec{E}$ is the electric field intensity. The electric field $\vec{E}$ is an irrational field, thus, it can be computed by minus the gradient the electric potential

$$\vec{E} = -\nabla\Phi \tag{2.4}$$

where Φ is the electric potential (also known as voltage) and ∇ is the gradient operator. Equation (2.4) can be substituted into equation (2.3) to relate the current density to the electric potential

$$\vec{J} = -\sigma\nabla\Phi. \tag{2.5}$$

The forward problem in DC resistivity studies is generally formed by representing a point source with a dirac delta function

$$\nabla \cdot \vec{J} = I\delta(\vec{r} - \vec{r_s}) \tag{2.6}$$

where δ is the dirac delta function, r represents vectorial position of any point within the domain, and r_s represents the vectorial position of the current source. The fundamental 2D DC resistivity differential equation is obtained by substituting equation (2.6) into Eq.(2.7)

$$\nabla \cdot (-\sigma(x,z)\nabla\Phi) = I\delta(\vec{r} - \vec{r_x})\delta(\vec{r} - \vec{r_y})\delta(\vec{r} - \vec{r_z}) \tag{2.7}$$

where the conductivity, σ, is assumed to be constant perpendicular to the x-z half space (McGillivray, 1992). There are two types of boundary conditions commonly used to solve the forward problem (i.e., Nuemann and Dirichlet). Nuemann conditions speficiy a value of the normal component electric field at exterior boundaries, and can be written in terms of the electric potential

$$\frac{\partial \Phi(x, y, 0)}{\partial z} = 0. \tag{2.8}$$

Dirichlet conditions specify the value of the potential to be zero at infinity, and can be written

$$\lim_{\vec{r} \to \infty} \Phi(r) = 0. \tag{2.9}$$

where r is

$$r = \sqrt{x^2 + y^2 + z^2}. \tag{2.10}$$

A formulation of the DC resistivity problem using the AEM is discussed in Chapter 5.

2.1.1 Apparent Resistivity and Array Types

Apparent resistivity measurements are conducted by injecting electrical current into the subsurface through a pair of electrodes (current source and sink) and measuring the resulting voltage difference across a separate pair of surface electrodes (potential electrode pair). Repeated sets of measurements across various electrode combinations are conducted to produce an apparent resistivity psuedosection. Apparent resistivity is defined as the resistivity of a homogeneous half space (Loke et al., 2003). The relationship below relates the measured surface voltage potential/injected current to the apparent resistivity for a four electrode array

$$\rho_a = k\frac{\Delta V}{I} \tag{2.11}$$

where ρ_a is the apparent resistivity, k is the geometric factor, ΔV is the measured voltage potential at the surface, and I is the injected current. The geometric factor is different for all array types. The geometric factor for a dipole-dipole array can be written as follows

$$k = 2\pi(r_{C1P1} - r_{C2P1} - r_{C1P2} + r_{C2P2}) \tag{2.12}$$

where r is the distance between the corresponding potential, P, and current, C, electrode combinations. The apparent resistivity distribution will vary for the same section if measured using different array types, and is not indicative of the true resistivity distribution of the earth (Loke et al., 2013). Some commonly used inverse methods to determine the true earth resistivity will be discussed in the subsection 2.1.3 along with some more recent advances in the field of non-linear geophysical problems.

The configuration of the potential and current electrodes is dependent upon the array type chosen to conduct the survey. All arrays have advantages and disadvantages regarding their spatial sensitivity, data coverage, acquisition time, and depth of investigation. The sensitivity of an array is defined as the ability for the specific array to detect spatial changes in resistivity within certain regions of the subsurface (Edwards, 1977). An array with good horizontal resolution (e.g., Dipole-Dipole) is sensitive to horizontal changes in resistivity, and is better suited to map vertical features. Conversely, an array with good vertical resolution (i.e., Schlumberger array) is sensitive to changes in resistivity in the vertical direction, which provides the ability to map horizontally stretching features (e.g., layered systems) (Loke, 2011). It is quite common to construct a hybrid array capable of providing a mixture of good horizontal and vertical resolution to provide optimal spatial coverage.

The invention of multi-electrode data acquisition systems greatly improved the ability to collect ERT data in a timely manner (Wilkinson et al., 2012). Current systems are capable of measuring eight voltage potentials across parallel channels for a single source pair for specific array types (e.g., dipole-dipole array). For this reason, the dipole-dipole array has a fast data acquisition time, however, it is more sensitive to noise than other array types (e.g., Wenner) (Loke, 2011). The current and potential electrode configurations for three different array types (i.e., dipole-dipole, Wenner, Schlumberger) are shown in Figure 2.1. The Wenner array (Figure 2.1C) has much longer data acquisition time as only one voltage potential is measured per current pair.

An apparent resistivity psuedosection generated from a 28 electrode dipole-dipole survey (max-

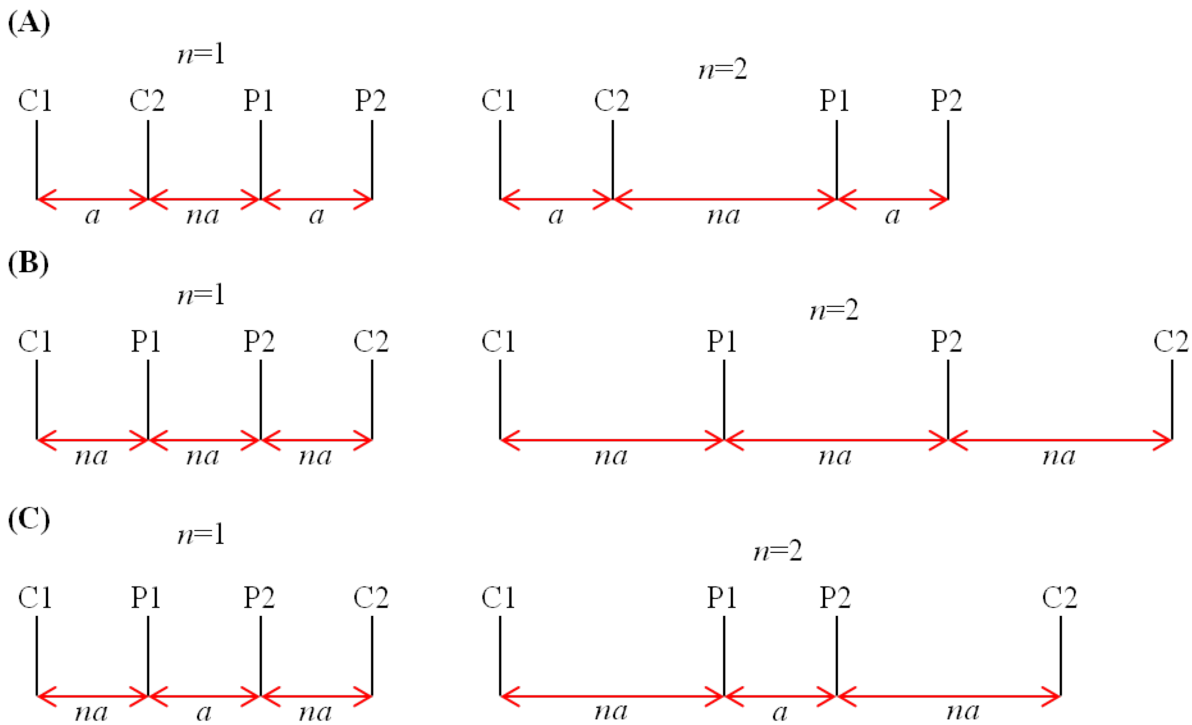

Figure 2.1: Electrode configurations for a dipole separation (n) of 1 and 2 for three different four electrode array types; (A) Dipole-Dipole array; (B) Wenner Array; (C) Schlumberger Array. C1 and C2 represent the electrodes injecting current into the earth and P1 and P2 represent the electrodes that the voltage potential is measured across.

imum electrode spacing (a) equal to 3) is illustrated in Figure 2.2. A psuedosection is created by plotting data points at an appropriate depth and lateral position. There have been numerous metrics for the appropriate depth to associate with each measurement (e.g., (Roy and Apparao, 1971; Edwards, 1977). The data points in the psuedosection shown by Figure 2.2 are plotted at their median depth of investigation (Edwards, 1977).It is important note how the resolution of data decreases with depth for this particular array type, which is evident in Figure 2.2 by the increase in vertical spacing between the blue circles between -2 m and -5.5 m. All arrays vary in their ability to detect changes in resistivity within specific regions of the subsurface. The sensitivity of an ERT array is defined as the ability for the array to detect spatial changes in resistivity within a specific region of the subsurface (Loke, 2011; Mcgillivray and Oldenburg, 1990; Wilkinson et al., 2012). The sensitivity of an array is determined by computing the Frechet derivative. Analytical expressions for Frechet derivatives exist for homogeneous half spaces, however, layered earth models require

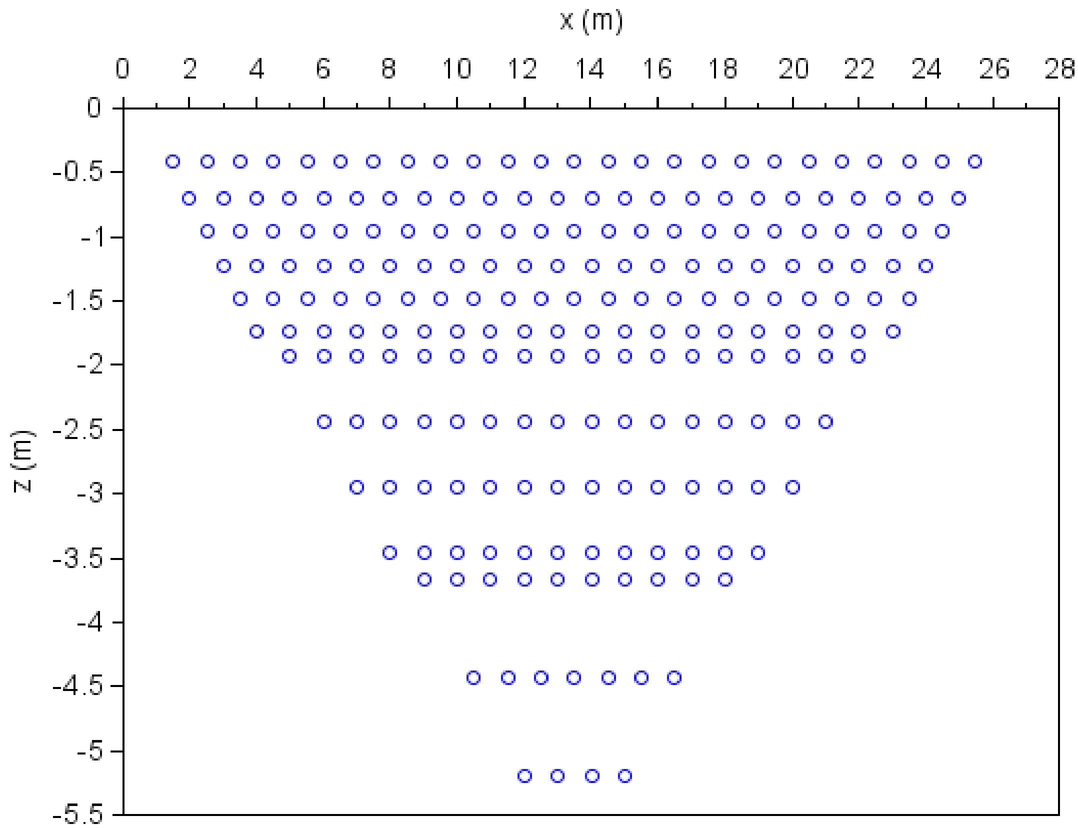

Figure 2.2: Plotted apparent resistivity psuedosection generated from a 28 electrode dipole-dipole array with a maximum electrode spacing (a) of 3 and maximum dipole seperation (n) of 6.

numerical techniques to compute the cumulative spatial sensitivity of an array. Conceptually, the sensitivity can be framed as the calculated change in the forward response relative to a change in the resistivity model. The concept of sensitivity is used to calculate the depth of investigation for specific arrays. Roy and Apparao (1971) developed an analytical expression for the Frechet derivative considering a 1D resistivity problem,

$$F_{1D} = \frac{2}{\pi} \frac{z}{(a^2 + 4z^2)^{1.5}} \tag{2.13}$$

where F_{1D} is the change in the calculated response (potential) relative to a perturbation in the model (resistivity), a is the spacing between a single current and single potential electrode, and z is the axis normal to the earth's surface. A plot of the function shows the depth and spacing combination at which the sensitivity of a specific array is maximized. This expression is also known as the depth of investigation metric, and can be used to calculate the depth at which the maximum sensitivity occurs for a specific array type (the depth that most heavily influences the potential measured at the surface). Edwards (1977) modified this expression to provide an estimate of the median depth of investigation, which is commonly used in inverse modelling of DC resistivity data to determine whether recovered resistivity structure is worthy of interpretation or should be considered as a mathematical artifact. It should be noted that the analytical relationships for depth of investigation were developed for homogeneous earth models, thus, stratified and layered media may affect the true depth of investigation (Loke, 2011).

2.1.2 Hydrogeologic Factors that influence electrical resistivity

The electrical resistivity of soil and rock is influenced by a wide array of hydrogeologic variables (e.g., water content, porosity, pore fluid salinity, clay content, mineralogy, and pore connectivity) (Everett, 2013). Table 2.1 provides the range of resistivity values that are commonly encountered in engineering studies.

Table 2.1: Resistivity ranges of common geomaterials. These values were compiled from the following studies: (Everett, 2013; Sharma, 1997; Palacky, 1987)

Geomaterial	**Resistivity** ($\Omega\ m$)
Sand	20-200
Gravel	100-1,000
Shale	10-50
Limestone	50-5,000
Clay	10-20
Groundwater	1-100
Alluvium	10-300

The two main types of electrical conduction that occur in near surface sediments are electrolytic conduction and electronic conduction. Electrolytic conduction occurs through the ions within the pore fluid saturating a material, while electronic conduction occurs due to the flow of electrons through highly conductive material Loke (2011). The following section will introduce some well established relationships that are commonly used in the field of hydrogeophysics.

Petrophysical and Hydraulic-Electrical Relationships

Petrophysical relationships link hydrologic state variables of rock and soil to their geophysical properties. One of the most widely used petrophysical relationships is Archie's Law (Archie, 1942). Archie's law is mainly used for determining the water and hydrocarbon saturation in rock formations (Glover, 2016). Archie's law for fully saturated media is

$$\rho_b = \rho_f \Theta^{-m} \tag{2.14}$$

where ρ_b is the bulk resistivity of the sample, ρ_f is the pore fluid resistivity, Θ is the porosity of the sample, and m is the cementation factor. Archie (1942) found that the cementation factor m ranges between 1.8 to 2.0 for consolidated sandstones, and 1.3 for unconsolidated sands. The relationship is commonly written in the following form

$$F = \Theta^{-m} \tag{2.15}$$

where F is the formation factor, which is equivalent to the ratio of the bulk resistivity, ρ_b, to the pore fluid resistivity, ρ_f. Additionally, Archie (1941) developed a form of the relationship for partially saturated samples

$$F = \Theta^{-m} S^{-n} \tag{2.16}$$

where S is the fraction of voids that are filled with fluid (degree of saturation), and n is the saturation exponent that is approximately 2.0 for fully saturated samples down to saturations as low as 15%. Another widely used petrophysical relationship is the Waxman-Smits (WS) (Waxman et al., 1968) conductivity model

$$\sigma_b = \frac{S_w^n}{F}(\sigma_w + \frac{BQ_v}{S_w}) \tag{2.17}$$

where σ_b is the bulk electrical conductivity, S_w is the water saturation, n is the saturation exponent (tortuosity exponent), B is the ionic conductance, and Q_v is the cation exchange capacity. The advantage of the WS model is that it can account for clay rich materials, whereas Archie's law is only valid for clay free materials as it considers only pore electrolytes as electrical conductors (Greve et al., 2013).

Numerous studies (Binley et al., 2005; Slater, 2007; Doussan and Ruy, 2009; Slater et al., 2014) have attempted to link petrophysical relationships to classical relationships describing the hydraulic conductivity of soil relationships (i.e., Kozeny-Carmen Eq.). The Kozeny-Carmen Eq. is

$$K = \frac{\rho_w g}{\mu} \frac{\phi^3 d_{10}^2}{180(1-\phi^2)} \tag{2.18}$$

where K is the saturated hydraulic conductivity of the medium, ρ_w is the density of water, g is the acceleration of gravity, μ is the dynamic viscosity of water, ϕ is the porosity of the sample, and d_{10} is the particle diameter of which 10 % of the sample mass is finer than. According to Slater et al. (2014), that $d_5 0$ and $d_6 0$ may be used in place of $d_1 0$, as no widely accepted standard for the effective particle diameter exists. Revil and Florsch (2010) derived an equation to predict K from electrical properties

$$K = \frac{\rho_w g}{\mu} \frac{d_e f f^2}{32m^2 F(F-1)^2} \tag{2.19}$$

where $d_e f f$ is the best approximation of the effective grain diameter for the samples. This allows for K to be predicted from the formation factor ,F.

2.1.3 Geophysical Inversion

As a result of the ill-posed nature of the DC resistivity problem, numerous resistivity distributions may produce an acceptable fit to observed data. To mitigate this, Tikhonov regularization (Tikhonov and Arsenin, 1977) is used to provide structural constraints on model parameters (resistivity contrasts or lack thereof across small spatial scales) to reduce the non-uniqueness of the problem. Some level of noise is inherent in all voltage measurements/resistance measurements due to insufficient electrode-ground contact. This also contributes to the non-uniqueness of the solution.

Constable et al. (1987) developed one of the most widely used algorithms for interpreting DC resistivity data. It is based on the principles of parsimony derived from "Occam's razor", and it was this notion that provided Constable et al. (1987) with the inspiration to name their algorithm "Occam's Inversion". Occam's inversion seeks to construct the smoothest resistivity model (smooth in the sense that resistivity values vary gradually in a piece-wise manner in space) whose response (calculated apparent resistivity values) matches the observed data to a predefined degree of misfit. This approach was used to remove complex model features not required to fit the observed data, and to stabilize the solution (Constable et al., 1987). Alternative algorithms may fit observed data equally well in terms of misfit (generally root mean squared error (RMSE)), however, they may be overly complex, and computationally expensive relative to the information they provide for less complex resistivity distributions.

A least squares solution is used to find the optimal set of parameters that best fit the data. The DC resistivity problem is non-unique due to the complexity of the earth and measurement noise. Thus, minimizing the sum of the squared residuals is a very natural way to approach the problem. The general least squares equation for a non-linear inverse problem can be written

$$A^T A c = b A^T \tag{2.20}$$

where A is the jacobian matrix, b is the solution matrix of specified values, and c is the coefficient matrix. Taking the inverse of the left hand side provides the solution form of the least squares problem.

$$c = b A^T (A^T A)^{-1} \tag{2.21}$$

The smoothness constrained regularized least squares inversion equation for DC resistivity (Constable et al., 1987; Loke et al., 2003) is given by

$$(A_i^T A_i + \lambda W^T W)\Delta r_i = A_i^T g_i - \lambda_i W^T W r_{i-1} \tag{2.22}$$

where λ is a spatial weighting factor or regularization parameter (Tikhonov and Arsenin, 1977)

, r_i is the logarithm of the resistivity values of the current iteration, r_{i-1} is the logarithm of the resistivity values of the previous iteration, Δr_i is the change in the model parameters (resistivity values) at the current iteration, and g_i is the difference between the logarithm of the calculated and observed resistivity values at the current iteration (deGroot Hedlin and Constable, 1990). The spatial weighting factor λ penalizes the model if there is a large change in the model parameters between adjacent cells. This weighting factor is used to mitigate the development of discontinuous resistivity bodies. Although a smooth model inversion is a widely accepted method for inverting DC resistivity data, it has been shown that it is not the optimal method for reconstructing an earth model where sharply contrasting resistivity bodies exist (Loke et al., 2003; de Groot-Hedlin and Constable, 2004). The next section discusses the use of an L1-norm based inversion scheme, and how it can be applied in certain geologic scenarios to improve earth model reconstruction.

The L1 norm based or "Robust" inversion scheme is very similar to the smooth model inversion. The major difference is that the routine seeks to minimize the absolute value of the data misfit as opposed to the sum of the square of the data misfit. Additionally, the model is not penalized for containing sharp changes in model parameters between adjacent model cells. This allows for the algorithm to reconstruct earth models that contain sharply contrasting resistivity bodies (Loke et al., 2003). The L1 norm based inversion equation is given by

$$(A_i^T R_d A_i + \lambda W^T R_m W)\Delta r_i = A_i^T R_d g_i - \lambda_i W^T R_m W r_{i-1} \tag{2.23}$$

where R_d and R_m are weighting matrices that give an equal value of importance to the misfit and roughness of the model. Günther and Rücker (2015) built upon the original work of McGillivray (1992); Constable et al. (1987) of the inversion methods. These methods use a variety of techniques to improve the interpretation of DC resistivity data by allowing for local mesh refinements. One of the more recent advances in ERT inversion is the use of a flexible grid geometry to discretize the model space in areas where complex features may exist. Günther et al. (2006) and Rücker et al. (2006) developed a method of flexible grid discretization that provides high numerical accuracy near discontinuities and point sources as the mesh may be locally refined. The added flexibility that this method provides is an attractive way to improve the accuracy of the forward solution;

however, the accuracy of this method is still dependent on the the discretization of a computational grid, unlike the AEM.

Global optimization (GO) schemes are less commonly applied to geophysical data; however, there are many advantages to using a global scheme for complex objective functions (Sen and Stoffa, 2013). For one, many schemes make the solution independent of a starting model given uniform coverage of the parameter space (Schwarzbach et al., 2005). Two of the most popular meta-heuristic optimisation techniques are the Genetic Algorithm and Simulated Annealing (Sen and Stoffa, 2013). Particle swarm optimization (PSO) fits in the class of evolutionary algorithms (Eberhart and Kennedy, 1995). PSO has previously been used in the inversion of geophysical data (Shaw and Srivastava, 2007; Godio and Santilano, 2018), however, it remains a growing area of interest as it is relatively new compared to the numerous local optimization schemes commonly employed. Pekşen et al. (2014) utilized a form of PSO along with the analytical solution for a layered anisotropic halfspace to determine layer resistivity values. The use of PSO will be discussed in detail in Chapter 6, and results from PSO simulations applied to DC resistivity data are presented in Chapter 8. .

Objective Functions

Determining an appropriate type of objective function to minimize is vital to the ability of an optimization scheme to produce a physically realistic set of model parameters (Oldenburg and Li, 1999). Most geophysical inversion schemes utilize a multi-part objective function that encourages the model to exhibit smooth or rough spatial variations. One of the underlying goals of this work is to evaluate the performance of a single part objective function void of factors that alter the spatial continuity of resistivity values.

The general objective function to be minimized for DC resistivity inversion (local optimization schemes) assuming data noise follows a Gaussian distribution can be written

$$F_1(m) = \frac{d_{obs} - f(m)}{\sqrt{n-1}s} \tag{2.24}$$

where d_{obs} is the observed apparent resistivity values, $f(m)$ is the calculated apparent resistivity values based upon the iteratively determined model parameters (resistivity values), n is the number of data points, and s is the standard deviation of the estimated data noise. However, the use of a multi-objective function is commonly applied to distinguish the effects of noise from signal on the recovered model (Schwarzbach et al., 2005). The second objective function generally minimized in DC resistivity inversion is a measure of the model roughness across the commonly applied finite element/finite difference grid. For a 2D resistivity distribution, the second part of the objective function is expressed by either the L1-norm or L2-norm criteria, which can be expressed in integral from

$$F_2(m) = \int \left(\left|\frac{\partial m}{\partial x}\right| + \left|\frac{\partial m}{\partial y}\right|\right) dxdz. \tag{2.25}$$

There is much debate in regards to the best form of a single objective function to use for optimization problems across many fields of study. Two popular error metrics commonly used to assess model performance are the Root Mean Squared Error (RMSE) and the Mean Absolute Error (MAE), which are written,

$$RMSE = \sqrt{\frac{\Sigma_{i=1}^{N}(d_i^{calc} - d_i^{obs})^2}{N}} \tag{2.26}$$

and

$$MAE = \frac{\Sigma_{i=1}^{N}|(d_i^{calc} - d_i^{obs})|}{N} \tag{2.27}$$

where d_i^{calc} and d_i^{obs} are the calculated and observed values, and N is the total number of observations. Willmott and Matsuura (2005) argue that the use of MAE is superior to that of RMSE as it provides a more true measure of average model performance. Chai and Draxler (2014) argue that neither metric is superior to one another as their usefulness depends upon the nature of the error distribution. It is important to note that RMSE may be written in various forms and that each form has implications for the behavior of optimization schemes. One of the more widely reported forms of misfit in geophysics is the root mean squared percentage error (RMPSE), as its magnitude is not dependent upon the units of the observed and predicted values. Thus, different inversion schemes are often compared using this value.

$$RMSPE = \sqrt{\frac{\Sigma_{i=1}^{N}\left(\frac{\overset{calc}{d_i} - \overset{obs}{d_i}}{\overset{obs}{d_i}}\right)^2}{N}} * 100\% \quad (2.28)$$

Each residual error is normalized by the observation. This means that two errors of equal magnitude for two different observations will not carry the same weight. An alternative way to evaluate data misfit is to use the root mean square logarithmic error (RMSLE)

$$RMSLE = \sqrt{\frac{\Sigma_{i=1}^{N}\left(log(\overset{calc}{d_i}) - log(\overset{obs}{d_i})\right)^2}{N}}. \quad (2.29)$$

The mathematical properties of logarithms make this form of the error metric more sensitive to equal magnitudes of error depending upon whether the predictions are greater than or less than the observation. This form of metric can be used to nullify the effect of outliers that over predict the data. The RMSE heavily penalizes large outliers regardless of the type of error. The four error metric described above will be implement within the optimization scheme described in Chapter 4, and their impact on recovered models will be discussed.

2.2 Analytic Element Method

The AEM is a computational method used to solve partial differential equations by superimposing analytical solutions (elements) within an infinite or finite domain. Control points located along the border of elements contain coefficients that are adjusted to satisfy boundary and interface/continuity conditions. A major strength of the AEM is that the solution accuracy (in terms of how well the boundary and interface conditions are met) is independent of the discretization of a computational grid (Strack, 2003). This allows for local details to be included within large domains without altering the computational grid. In the traditional use of the AEM within the field of groundwater, elements represent physical hydrologic features (i.e., aquitards, aquicludes, heterogeneities, fractures, rivers, lakes, wells). The method has been developed mainly for problems in groundwater engineering (Haitjema, 1995; Strack, 2003; Steward et al., 2011; Steward and Allen, 2013; Gaur et al., 2011) and coastal engineering (Steward, 2018, 2020b). Steward and Allen (2013) developed a computational method for a grid of interconnected rectangular elements to evaluate groundwater flow from local to regional scales across the High Plain Aquifer region. The computational framework developed in Steward (2020a) serves as the basis for the computational methods for the electrostatic boundary value problems that are explored in this research.

Very little research has been conducted using the AEM in the field of near surface geophysics. Furman et al. (2002, 2004) utilized the AEM to compute the cumulative spatial sensitivity of ERT arrays through a perturbation analysis. Their studies determined the optimal set of electrode configurations for distinguishing subsurface features at specific locations. Although this was the first work utilizing the AEM in ERT studies, no recent advances have since been made. Furman et al. (2007) stated that they would not use the AEM in their future work due to the absence of a solution method for layered systems. A separation of variables solution for rectangular elements has been adapted here from Steward and Allen (2013) to solve for the 2D electric potential and electric field distribution within a series of interconnected rectangular elements. Rectangular elements provide a flexible way to incorporate heterogeneity and layering into the analysis of electrical conduction using the AEM. The ability of the AEM to accurately match interface conditions where locally steep electric potential gradients exist is one of the main advantages it has over traditional numerical techniques used to simulate electric current flow (Furman et al., 2002). Haitjema et al. (2010) demonstrated the numerical advantages of the AEM over a finite element based groundwater model across sharp changes in transport properties. Given the commonalities between groundwater flow and electrical conduction, similar advantages may exist when solving for the electric flow field through heterogeneous bodies. An in depth analysis of electrical conduction through various subsurface geometries is provided in Chapter 6.

Chapter 3

Conceptualizing Groundwater-Surface Water Interactions within the Ogallala Aquifer Region using Electrical Resistivity Imaging

This article was published in the Environmental and Engineering Geophysical Society's *Journal of Environmental and Engineering Geophysics* in June 2019. The full citation is:

Koehn, W. J., Tucker-Kulesza, S. E., Steward, D. R. (2019). Conceptualizing Groundwater-Surface Water Interactions within the Ogallala Aquifer Region using Electrical Resistivity Imaging. Journal of Environmental and Engineering Geophysics, 24(2), 185-199.

https://doi.org/10.2113/JEEG24.2.185.

3.1 Abstract

Dynamic interactions between rivers and aquifers are controlled by the underlying hydrogeologic environment, as well as the type of hydrologic connection between the riverbed and saturated zone. The Arkansas River supplies groundwater to a heavily exploited region of the Ogallala Aquifer across Western Kansas. Site characterizations of this region using existing well and borehole data reveal large scale geologic features that significantly impact recharge processes, such as the Bear Creek fault. However, the existing hydrogeologic data do not provide the level of detail needed to fully understand the contribution of the losing river system to Arkansas Alluvial aquifer recharge. Knowledge about riverbed hydrogeology is acquirable using electrical resistivity imaging (ERI) surveys. ERI surveys and soil sample analysis were conducted at three sites along the Arkansas River to characterize the hydrogeologic environment within the Arkansas River Alluvial aquifer, which overlies the Ogallala aquifer. Temporal changes in electrical resistivity served as an indicator of the hydrologic response of the alluvial sediments to changes in river discharge as different patterns of water movement from the Arkansas River to Arkansas River Alluvial aquifer were observed. The ERI surveys revealed both fully connected and disconnected regions between the riverbed and groundwater table. The results supplement the existing geologic characterization of this region, and provide a more spatially detailed view of the hydrogeologic environment that has a direct causative effect on groundwater surface water interactions. Understanding the behavior of river-aquifer interactions is vital to the ability to predict the future holds of this important groundwater system.

3.2 Introduction

The dynamic equilibrium achieved by groundwater and surface water within the Ogallala aquifer region has been greatly affected by widespread depletion over much of the past century (Gutentag et al., 1984). The Arkansas River overlies the Ogallala aquifer in Western Kansas and was a gaining stream fed by groundwater prior to the development of widespread irrigated agriculture. Groundwater withdrawals in excess of natural recharge have depleted groundwater levels, and the Arkansas River is now predominantly a losing river in areas overlying the Ogallala formation (Whittemore, 2002; Steward and Allen, 2016). Steward and Allen (2016) demonstrated that the Ogallala Aquifer has crossed the threshold of peak groundwater depletion, and society is no longer capable of extracting the same levels of groundwater to sustain this agricultural region. Furthermore, recharge through the terrestrial farming ecosystem would require hundreds of years to replenish depletion by historical natural recharge processes (Steward et al., 2013). Thus, losing rivers overlying the Ogallala aquifer, such as the Arkansas River in Western Kansas, play an important role in the regional water balance as they serve as primary sources of groundwater recharge (Whittemore, 2002). The ability to conceptualize different flow regimes existing between surface water and groundwater is vital when modeling stream aquifer interactions; however, the existing hydrogeologic understanding of the alluvial environment through which Arkansas River recharge occurs is too general based on existing well and borehole data to elucidate complex alluvial recharge processes.

Accurate modeling of groundwater surface water interactions depends on the ability to characterize subsurface hydraulic properties, and knowledge about the flow regime existing between the surface water body and underlying formation (Sophocleous, 2002; Brunner et al., 2011). Traditional hydrologic field tests, such as pumping tests and slug tests, reveal the hydraulic conductivity of an aquifer segment near a borehole, however, they provide little insight into the spatial distribution of the aquifer hydraulic conductivity (Slater, 2007). Furthermore, inferences based upon hydrologic data (i.e., groundwater head) collected adjacent to a stream may neglect the presence of an unsaturated zone between the surface water body and the groundwater table beneath the streambed, which significantly impacts infiltration rates (Brunner et al., 2009). The presence of an unsaturated zone between the streambed and groundwater table means the river-aquifer system is disconnected (Sophocleous, 2002). Physically, this means that the infiltration rate of surface water is independent of the groundwater table elevation (Brunner et al., 2009). Conversely, a saturated zone is present beneath the streambed and groundwater table in a fully connected system.

Many studies have examined the affect stream-aquifer connectivity has on the magnitude and rate of aquifer recharge, as well as the hydrogeologic conditions necessary for connection and disconnection to occur. One of the first studies to analyze disconnection was Reisenauer (1963), who showed numerically that under steady state conditions, an inverted water table (IWT) may form beneath a streambed in the absence of a clogging layer. Brunner et al. (2009) developed the criteria necessary to achieve stream-aquifer disconnection under steady state conditions in the presence of a clogging layer (i.e., streambed layer with lower hydraulic conductivity relative to the underlying aquifer material). Shanafield et al. (2012) simulated the transient water table response of a connected and disconnected stream aquifer system to examine its sensitivity to the following parameters: stream width, aquifer saturated hydraulic conductivity, streambed saturated hydraulic conductivity, and the of amount available moisture storage within the unsaturated zone. Xie et al. (2014) and Xian et al. (2017) analyzed the development of an IWT within and beneath a streambed for various connection scenarios. While previous studies show the hydrogeologic criteria that affect stream-aquifer connectivity, field methods to detect different connection regimes are still needed. Recharge rates through unsaturated soils are highly variable and difficult to estimate with direct measurements of vadose zone properties (Nimmo et al., 2006). Moreover, conducting field measurements near local recharge areas is not always possible due to site conditions, limited access, or excessive cost.

Developing geophysical methods to accurately map streambed hydraulic properties is a popular research area within the field of hydrogeophysics (Binley et al., 2015; Loke et al., 2013). While the goal of this study is not to quantify streambed hydraulic properties with ERI, the depiction of the hydrologic state beneath the riverbed will significantly improve the conceptualization of river-aquifer connectivity. Electrical resistivity is an intrinsic property that quantifies a materials ability to oppose the flow of electrical current. Hydrogeologic and environmental factors such as the water content, porosity, salinity, clay content, pore geometry, lithology, and pore-fluid temperature control the electrical resistivity of a medium (Everett, 2013). ERI surveys can be used to delineate groundwater discharge areas (Nyquist et al., 2008), recharge pathways through mantled sinkholes (Schwartz and Schreiber, 2009), and riverbed sediment architecture (Crook et al., 2008). Daily et al. (1992) showed that ERI can effectively map changes in water content within the vadose zone by analyzing the temporal changes in electrical resistivity in response to an infiltration event. Slater and Lesmes (2002) demonstrated that complex electrical conductivity can be used to predict the saturated hydraulic conductivity of a medium. More recently, Slater et al. (2014) showed that geophysically derived saturated hydraulic conductivity estimates were consistent with saturated hydraulic conductivity values measured in the laboratory. Rucker (2009) coupled synthetic electrical resistivity models with an infiltration model to track the movement of a wetting front through porous media. Dunbar et al. (2015) conducted a series of ERI surveys to characterize a shallow groundwater system within an agricultural setting. Brownbill et al. (2011) employed ERI surveys along a losing reach of river to gain insight on the interconnection between groundwater and surface water. These previous studies are prime examples of how ERI can be utilized to exploit different components of groundwater systems, and support the application of such an approach to examine river-aquifer connectivity.

Complex interactions occurring between the Arkansas River and underlying Arkansas River Alluvial aquifer were explored in this study with existing hydrologic data (i.e, stream discharge and aquifer response data) and ERI surveys of riverbed sediments. Analysis of existing monitoring well data collected within the Arkansas River Alluvial aquifer illustrated the dynamic response of the water table to changes in river discharge across the study region. Differences in the magnitude and rate of the water table response were used to construct hypothesized conceptualizations of the connection regime (fully connected and disconnected) between the Arkansas River and Arkansas River Alluvial aquifer at three different locations. ERI surveys were conducted at these specific locations to collect more localized hydrogeologic information beneath the riverbed to examine the validity of the hypotheses. The electrical resistivity distribution below the riverbed identified the approximate depth of the water table below the riverbed, and revealed lowly and highly resistive areas beneath the inundated riverbed. The discontinuous resistivity distribution above the groundwater table was interpreted primarily to be a result of discontinuous water content distributions. The delineation of the groundwater table location revealed different states of river-aquifer connectivity across the study region. These findings provide hydrologic details that will facilitate the implementation of physically realistic groundwater-surface water models (fully saturated flow, or variably saturated flow). These surveys illustrate the importance surface water and infiltration transiency have on groundwater recharge processes in riverbeds, and show the difficultly in determining the connection status of a system without localized hydrogeolgoic information in regions that have a direct causative effect on stream-aquifer interactions. A riverbed may behave as both a connected and disconnected system at one specific location, which is something that cannot be distinguished with aquifer response data alone. The hydrogeologic background for the study region is first discussed before presenting the hypothesized conceptualization of the localized flow systems at each site. Lastly, the ERI surveys and their hydrogeologic interpretations as they relate to stream-aquifer interactions are presented followed by the key findings and conclusions.

Hydrogeologic Background

An overview map of the study region is shown in Figure3.1, which delineates the extent of the Arkansas River Alluvial aquifer and underlying Ogallala formation across Western Kansas. The Bear Creek fault, which is located just downstream (east) of Hartland, KS, defines the westernmost boundary of the Ogallala formation. The bedrock surface decreases in elevation by as much as 60 m just downstream of the Bear Creek fault (Whittemore, 2002; Young et al., 2000). Lithology records from wells along the Arkansas River (A', B', C', and D') were used to construct the generalized hydrogeologic cross section shown in Figure3.1. The hydrogeoloic units were consolidated into the four categories shown in the legend. An aquitard of varying thickness separates the Arkansas Alluvial aquifer and Ogallala aquifer.

Previous hydrologic studies have primarily focused on characterizing the interactions between the Arkansas River Alluvial aquifer and underlying Ogallala aquifer. Butler and Healey (1999) conducted a localized hydrologic study which analyzed the performance of slug tests in a nest of five monitoring wells screened at various depths within the Arkansas River Alluvial aquifer and Ogallala aquifer near Deerfield, KS (i.e., well C' in Figure3.1). All wells were screened within different hydrologic units, ranging from the Arkansas River Alluvial aquifer (elevation of 900 m) to the deepest Ogallala sediments (elevation of 790 m), to determine hydraulic conductivity at different depths. Butler and Healey (1999) estimated the average hydraulic conductivity of the Arkansas River Alluvial aquifer to be between 40 m/day and 45 m/day. The hydraulic conductivity of permeable units within the Ogallala aquifer ranged between 2.5 m/day to 22 m/day. Whittemore et al. (2000) also conducted a hydrologic study to determine the interaction between the Arkansas River Alluvial aquifer and the underlying Ogallala aquifer using the same five monitoring wells as Butler

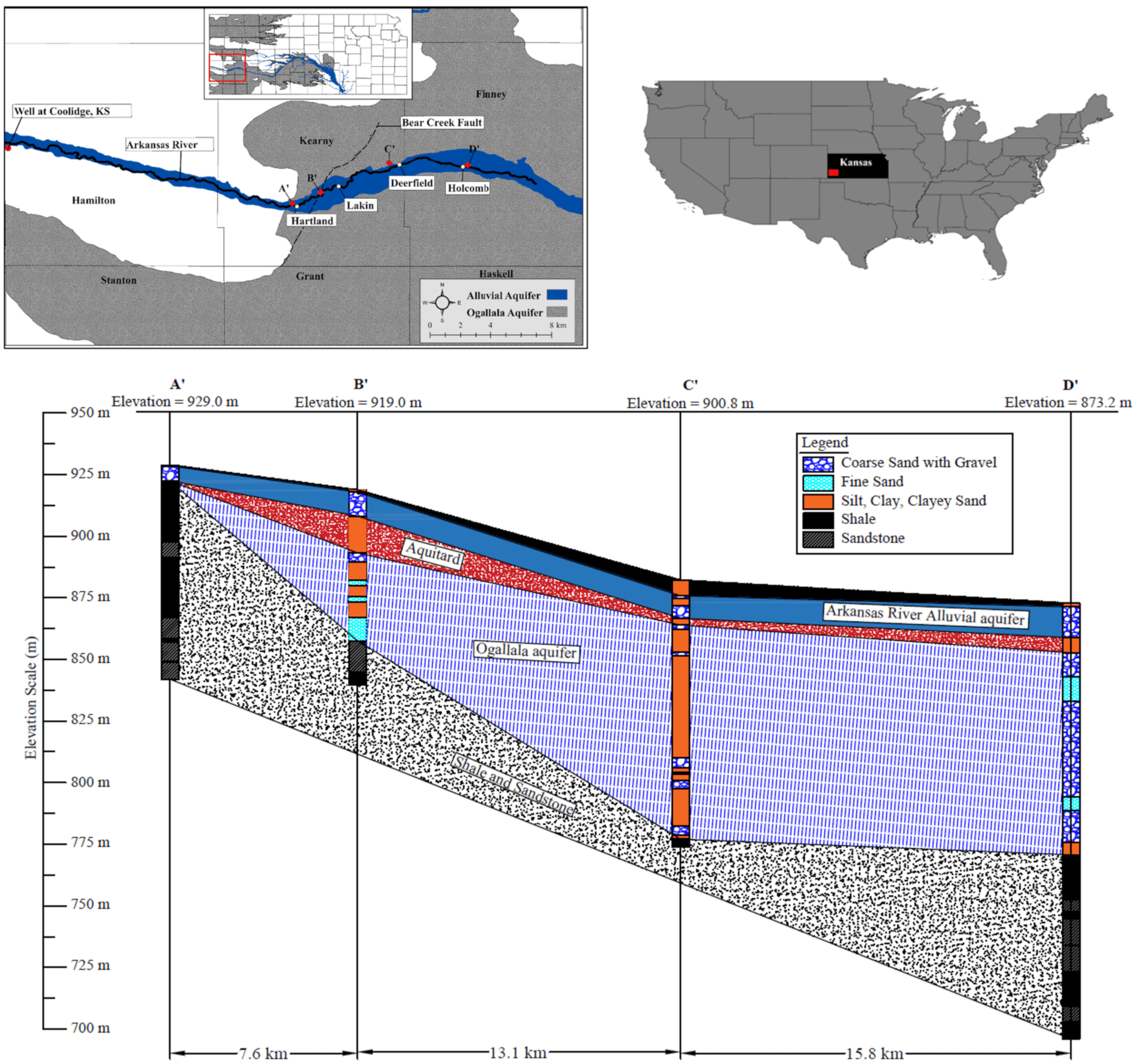

Figure 3.1: Overview map of the study region showing the extent of the Ogallala Aquifer and Arkansas Alluvial Aquifer. A generalized hydrogeologic cross section constructed form boreholes (A', B', C', and D') across the study area is shown.

and Healey (1999). Borehole lithologic records showed layers of coarse-grained aquifer material separated by several confining units (e.g., silt and clay). Groundwater samples were collected from each of the five wells to determine the vertical variation in the total dissolved solids (TDS) concentration. The TDS concentration ranged between 2,700 mg/L within the Arkansas River Alluvial aquifer to less than 500 mg/L within the deepest Ogallala aquifer sediments. The large gradient in TDS showed that the vertical movement of water between the Arkansas River Alluvial aquifer and underlying Ogallala aquifer was limited at Deerfield. Whittemore et al. (2000) also collected water quality data from a series of five monitoring wells further downstream near Garden City, KS, which is located approximately 11 km east of Holcomb, KS. There was a markedly different trend in the TDS concentration versus depth at this site. The TDS concentrations of groundwater within deeper wells screened within Ogallala sediments were at or above the TDS concentrations observed within Arkansas River Alluvial aquifer wells. This indicates that the interaction between the two aquifers increases further downstream of the Bear Creek fault. In similar studies conducted by Young et al. (2000) and Whittemore (2007), the connection between the two aquifers was reported to be somewhat limited near Lakin and Deerfield by numerous silt/clay layers observed within borehole lithologic records. These previous hydrogeologic conceptualizations of the region show the complexity of interactions between the Arkansas River Alluvial aquifer and Ogallala aquifer, however, they do not provide the details necessary to understand how the Arkansas River and Arkansas River Alluvial aquifer are hydrologically connected.

The Arkansas River is highly saline, and TDS concentrations within the river can exceed 4,500 mg/L during low flow periods (Whittemore, 2002). The alluvial groundwater within the study region is also highly saline, as indicated by the high electrical conductivity values in the time series plot shown in Figure 3.2a. These data were collected from a USGS monitoring well located 1 km south of Coolidge, KS, which is located approximately 60 km to the west of Hartland (see Figure3.1). No other monitoring wells within the study region reported groundwater temperature or groundwater electrical conductivity. The groundwater electrical conductivity increased by approximately 2,000 μS/cm between June 2014 and June 2018, which corresponded to a 5.0 Ω m increase in electrical resistivity. However, the groundwater electrical conductivity increased by less than 200 μS/cm (0.1 Ω m) during the study period (September 2015 and September 2016).

In terms of the spatial variation of groundwater quality, the study conducted by Whittemore et al. (2000) reported a large vertical gradient in the TDS concentration between the Arkansas River Alluvial aquifer and Ogallala aquifer depending upon connectivity. However, in this study the spatial distribution of TDS within the Arkansas River Alluvial aquifer likely did not affect the spatial distribution of electrical resistivity at the riverbed scale based upon the negligible differences in groundwater electrical conductivity shown in Figure 3.2a.

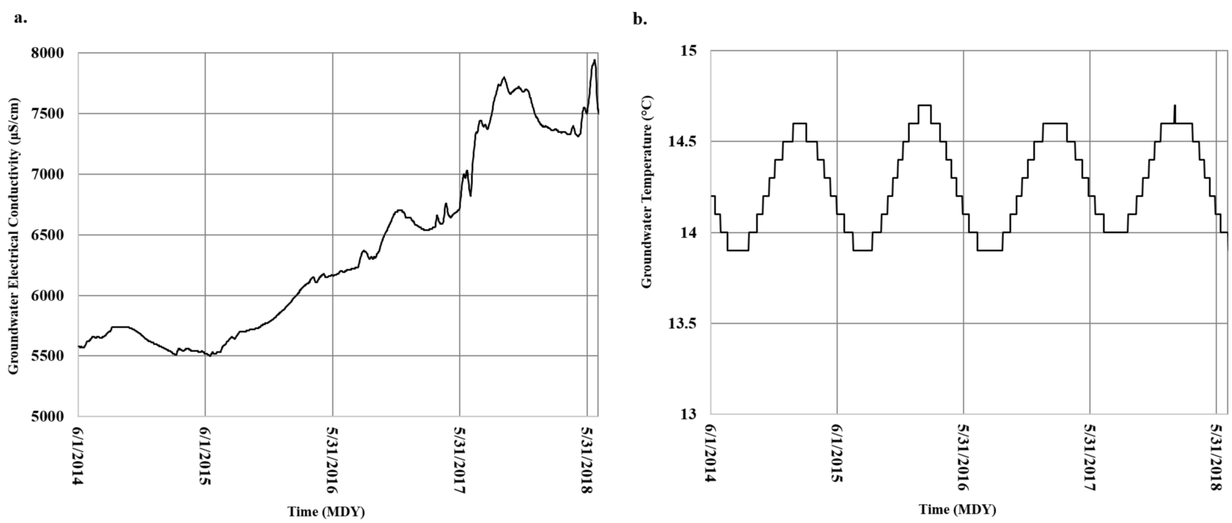

Figure 3.2: Groundwater temperature and electrical conductivity data obtained from a USGS monitoring well near the Kansas-Colorado border. a) Groundwater electrical conductivity between June 2014 and June 2018 within the Arkansas Alluvial Aquifer near Coolidge, KS. b) Groundwater temperature between June 2014 and June 2018 within the Arkansas Alluvial Aquifer near Coolidge, Kansas.

Negligible temporal variation in the groundwater temperature (i.e., less than 0.5 °C) occurred within the Arkansas River Alluvial aquifer as shown by the time series plot in Figure 3.2b. Therefore, temporal changes in resistivity below the groundwater table were also not considered to be related to changes in groundwater temperature. The groundwater temperature varied between 14.0 °C to 14.5 °C between June 2014 and June 2018.

Hydrographs from monitoring wells screened within the Arkansas River Alluvial aquifer at Hartland, Deerfield, and Holcomb were analyzed to gain insight into the spatial and temporal hydraulic head response of the Arkansas River Alluvial aquifer to changes in river discharge. Table 1 gives the land surface elevation at each well, the completed well depth (below the ground surface), and the riverbed elevation nearest each well. The screened depths of the Hartland and Holcomb wells were not available.

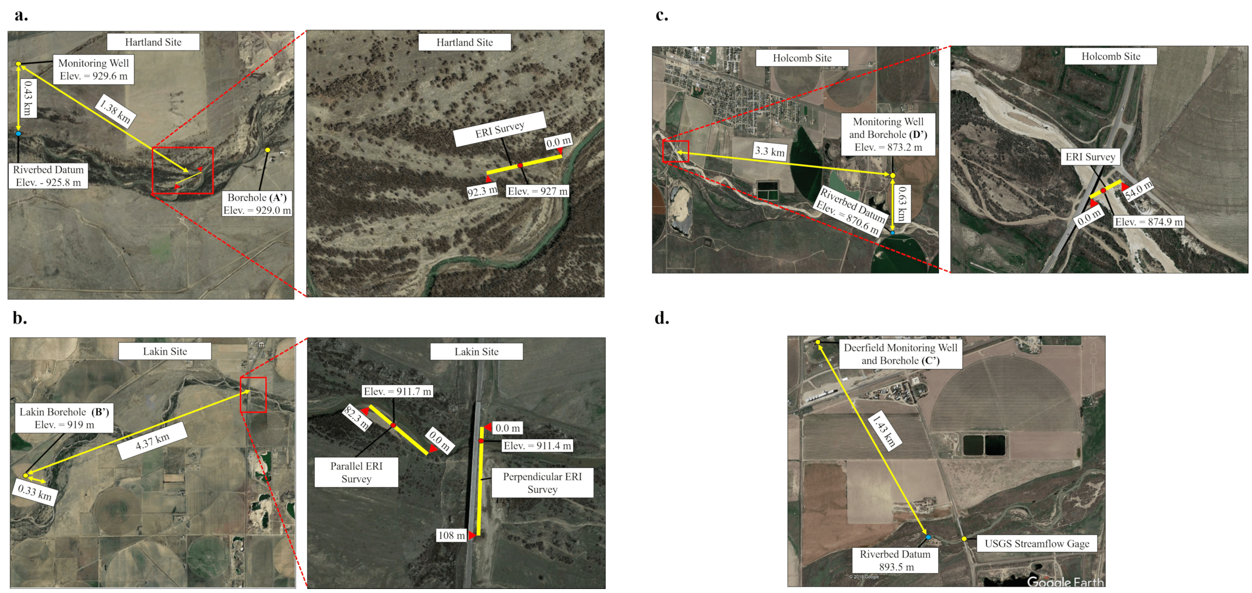

Figure 3.3: Layout and alignment of ERI surveys at each site along the Arkansas River. The location of the monitoring wells and boreholes relative to the Arkansas River are shown for each ERI survey site along with the riverbed datum, and well elevations. The starting and ending locations of each survey are labeled along the yellow lines in the close up view, which show the survey transects. a) Hartland b) Lakin c) Holcomb d) Deerfield (Google Earth, 2018)

The majority of the wells within the alluvial sediments are screened just above the completed well depths. The location of the monitoring wells relative to the Arkansas River and ERI survey locations are shown in Figure 3.3, along with the starting and ending location of the ERI surveys. The hydraulic head observed at each monitoring well is plotted as a function of time in Figure 3.4a. The depth to the water table (i.e., Arkansas River Alluvial aquifer) observed at each well relative to the nearest riverbed elevation is given in Figure 3.4b. Negative y-axis values in Figure 3.4b correspond to periods when the water table elevation observed at the well was above the referenced riverbed elevation. The change in groundwater head relative to the beginning of the observation period (January 2008) is shown in Figure 3.4c. The discharge hydrograph of the Arkansas River at Deerfield, KS, is shown in Figure 3.4d.

The hydraulic head observed at the Hartland well remained stable between 2008 and 2015, before increasing by approximately 2 m between 2015 and 2018. The increase in hydraulic head

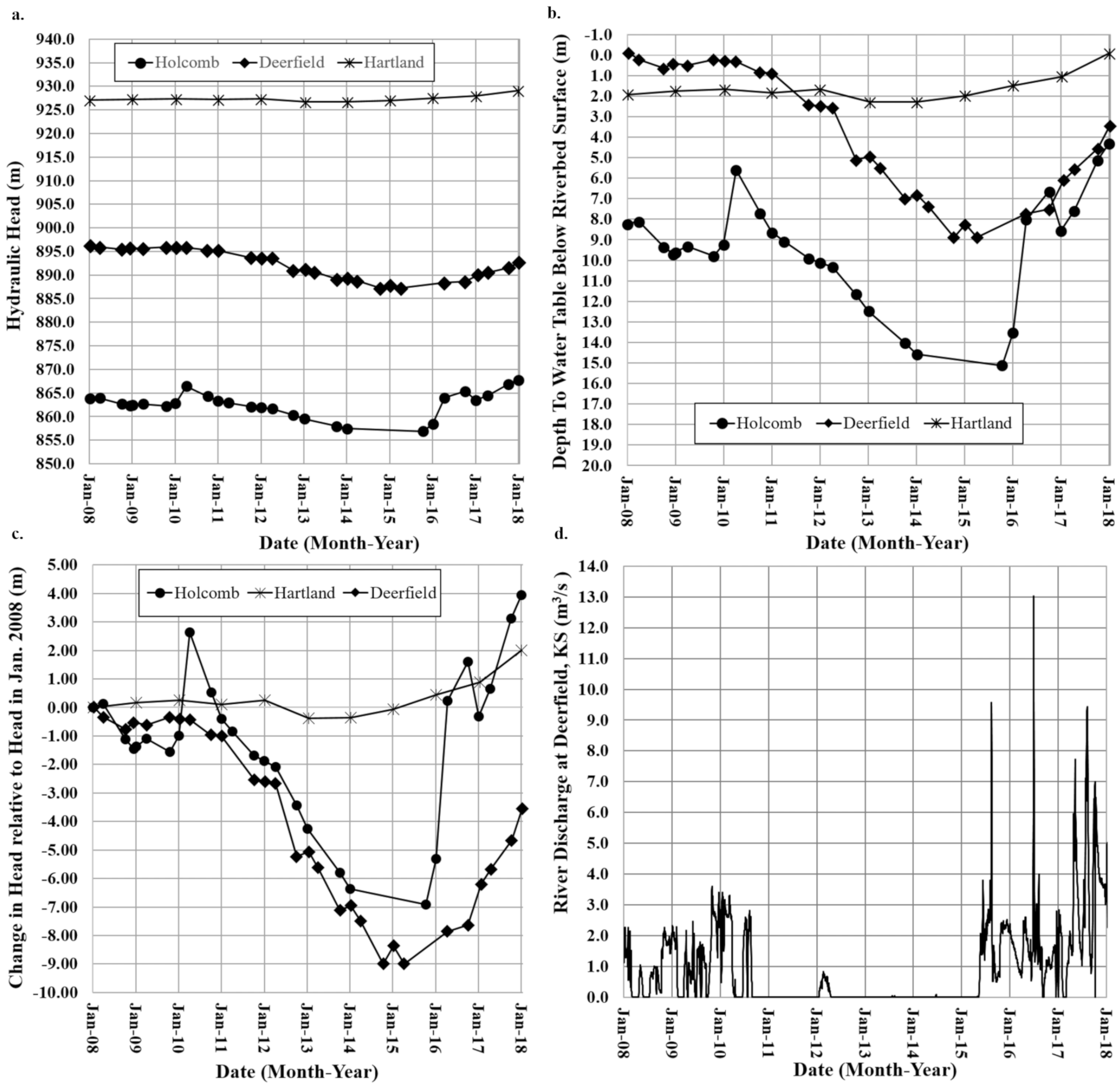

Figure 3.4: River discharge, hydraulic head, and depth to groundwater measurements across the study region. a) Hydraulic head at each monitoring well between 2008 and 2018. b) Depth to the water table relative to the riverbed surface. c) Change in groundwater head relative to Jan. 2008 at each well. d) Discharge hydrograph of the Arkansas River between 2008 and 2018

corresponds to an increase in bank storage within the Arkansas River Alluvial aquifer, and is a result of increased river discharge post 2016. The streamflow conditions at Deerfield are not representative of the relatively steady streamflow that occurs at Hartland. The Arkansas River Alluvial aquifer exhibited a more pronounced response to changes in streamflow downstream of the Bear Creek fault at Deerfield and Holcomb. This was expected, as more episodic river flows

Table 3.1: Monitoring Well Information

Location of Well	Land Surface Elevation (m)	[1]Completed Well Depth (m)	[1]Depth of Screened Interval (m)	[2]Riverbed Elevation (m)
Hartland	929.6	8.84	Not Available	925.8
Deerfield	900.8	14.02	10.97 to 14.02	893.5
Holcomb	873.3	16.76	Not Available	870.6

[1]Depths are relative to the land surface elevation
[2]Elevation of the riverbed surface nearest each well

exist downstream of the Bear Creek fault where the Arkansas River Alluvial aquifer overlies the Ogallala aquifer. Additionally, pumping from the underlying Ogallala formation enhances the seepage rate between the Arkansas River Alluvial aquifer and Ogallala aquifer (Whittemore, 2002). The groundwater table at Deerfield and Holcomb showed a strong hydraulic response to changes in river discharge between 2008 and 2018. The hydraulic head increased by approximately 4 m within a 3 month span in response to the high flow event at the end of 2009 and beginning of 2010 shown in Figure 3.4d. This event produced little to no aquifer response at Deerfield as the riverbed elevation and groundwater table elevation were approximately equal during this period as shown in Figure 3.4b. Substantial decreases in groundwater head occurred during the low flow period between 2011 and 2015 at both Deerfield and Holcomb. By the end of 2015, the depth to the water table below the riverbed at Holcomb had increased to as much a 15 m, which nearly exceeded the completed well depth (given in Table 1). This extended period of no flow created a disconnected state between the river and aquifer at both sites. Both wells showed a strong response to the increased river discharge near the end of 2015, however, the magnitude of the initial water table response at Holcomb was larger than the initial response at Deerfield (i.e., steeper slope in Figure 3.4c).

A downward shift in the rate of the water table response occurred at Holcomb near the end of 2016, and the water table at Deerfield and Holcomb exhibited fairly similar behavior between 2017 and 2018. Although it is difficult to distinguish the exact hydrologic factors controlling the differences in the magnitude and rate of the aquifer responses at Holcomb and Deerfield, two general conclusions about the stream-aquifer system can be made:

1.) The stream-aquifer system was disconnected at Deerfield and Holcomb prior to the flood event that occurred in mid-2015.

2.) Between Jan. 2017 and Jan. 2018, the system exhibited more stable behavior (i.e., rate of water table fluctuations were approximately linear), however, it is unclear whether this behavior is consistent with that of a fully connected or disconnected system.

Based upon the response of the water table to seasonal changes in river discharge, hypothesized conceptualizations of the localized flow systems were constructed, which are shown in Figure 3.5.

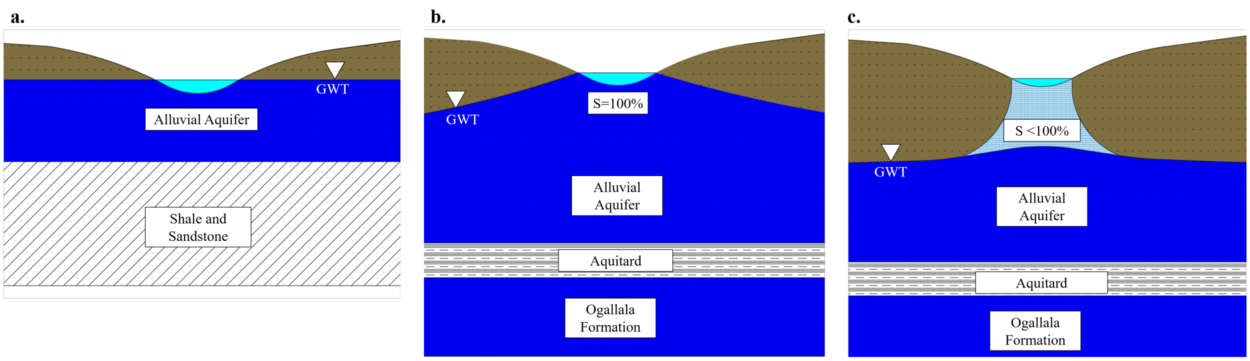

Figure 3.5: Schematic illustrating the general hydrogeologic setting beneath the Arkansas River and the type of hydrologic connection that persists between the Arkansas River and Arkansas Alluvial aquifer at three locations. a) Hartland - fully connected river that maintains a near equilibrium of fluxes with the alluvial aquifer. b) Lakin - fully connected losing river. c) Holcomb - disconnected losing river.

A fully connected (fully saturated) perennial river is illustrated west of the Bear Creek fault in Figure 3.5a (i.e., Hartland). The transition from a fully connected (fully saturated) losing river at Lakin to a disconnected losing river at Holcomb are illustrated in Figure 3.5b and Figure 3.5c, respectively. The validity of these conceptualizations are further examined with the hydrologic interpretation of the ERI surveys.

3.3 Methods

ERI surveys are conducted by injecting electrical current into the subsurface through an electrode pair (current pair) while simultaneously measuring the induced voltage potential between a separate electrode pair (potential pair). Repeated sets of measurements using various electrode pair configurations are conducted in an ERI survey, and the sequence of measurements is defined by the array type. A dipole-dipole array was used to acquire all datasets. The dipole-dipole array was chosen for its high sensitivity to horizontal changes in resistivity (Loke et al., 2003). An array with high sensitivity to horizontal changes in resistivity provided the best opportunity to detect a change in saturation across the streambed, which would ultimately provide evidence of stream-aquifer disconnection. The SuperSting Earth Resistivity Induced Polarization and Self Potential System from Advanced Geosciences, Inc. was used to conduct all ERI surveys.

Surveys that spanned the river used both submersible and dry electrode cables in series. Land based (dry) survey segments utilized 30 cm long stainless steel electrodes. Submersed (underwater) portions of surveys used graphite coated electrodes placed at the water-sediment interface. Electrode spacing ranged between 1.52 m to 2.0 m, and was dependent upon the available space at the site. The riverbanks along the Arkansas River were heavily vegetated, and required survey transects to be shortened at the Holcomb site. The timing of surveys depended upon the discharge in the Arkansas River. Periods with flows exceeding 15 cubic meters per second (cms) were excluded from potential survey times as the submersible cable was not able to remain stationary during testing.

All resistivity data were processed with EarthImager 2D (AGI, 2007). An Occam style smooth model inversion was used to process all datasets in this study (Constable et al., 1987). The advantage of using a smooth model inversion is that resistivity values undulate smoothly across the model domain, yielding more stable solutions than other inversion techniques (Loke et al., 2003). Segments of surveys that were submerged were set to a constant resistivity value (measured Arkansas River water resistivity) for inversion. Table 3.2 shows the the measured Arkansas River water resistivity where appropriate. The depth of water over each electrode was measured to determine the water layer thickness and included in the model.

3.4 Results

The three sites selected for ERI instrumentation (Hartland, Lakin, and Holcomb) are shown in Figure 3.1. The Hartland site was chosen as it overlies the shallower Arkansas River Alluvial aquifer

Table 3.2: ERI survey details for each site

Site	Survey Date	Alignment Relative to River	River Water Resistivity (Ω m)
Hartland (Figure 3.6A)	Sept. 2015	perpendicular	2.35
Hartland (Figure 3.6B)	Mar. 2016	perpendicular	2.56
Lakin (Figure 3.7A)	Jul. 2016	perpendicular/spanning	5.30
Lakin (Figure 3.7B)	Sept. 2016	perpendicular/spanning	2.90
Lakin (Figure 3.8)	May 2016	parallel	dry riverbank
Holcomb (Figure 3.9A)	Jul. 2016	perpendicular/spanning	2.90
Holcomb (Figure 3.9B)	Sept. 2016	perpendicular/spanning	dry riverbed

where the Ogallala formation is not present. The Hartland site represents the fully connected hydrologic flow system that maintains a near equilibrium of fluxes conceptualized in Figure 3.5a. The Lakin site provided a prime spot to analyze a portion of the Arkansas River Alluvial aquifer that was hypothesized to be a fully connected system (i.e., Figure 3.5b). The Holcomb site was chosen because of the measured highly periodic Arkansas River flows (i.e., Figure 3.4d). Additionally, the Holcomb site allowed for surveys to be conducted under flow and no flow conditions. This was advantageous as it allowed for two distinctly different hydrologic states to be imaged. A summary of ERI survey details is given in Table 2.

Soil samples were collected from the top 0.5 m to 1 m of the riverbed surface at each site, and classified in accordance to the Unified Soil Classification System (USCS) as per American Society of Testing and Materials (ASTM) standard D2487-11 to support ERI survey interpretation (Standard, 2011). Site access was highly limited within the study area and borehole sampling via drill rig within the riverbed was not possible. The USCS classification, saturated hydraulic conductivity K_{sat}, and median grain size (D_{50}) of each sample are given in Table 3. Constant head permeability tests were conducted in accordance to ASTM D2434-68 to determine the saturated hydraulic conductivity of two of the granular riverbed samples (ASTM, 2006). The median grain size represents the particle diameter of which 50% of the sample mass is finer than (Mitchell et al., 2005). The higher median grain size at the Lakin and Holcomb sites relative to that at Hartland shows the riverbed surface to be slightly coarser in texture. The sample collected from the Lakin riverbank had a median grain size that was roughly one order of magnitude lower than that of the riverbed, showing the increase in finer grained sediments deposited along the edges of the riverbed. Although fluxes between surface water and groundwater depend upon much more than just the hydraulic conductivity obtained from a point sample as discussed earlier, these soil data support the near surface ERI interpretations. Additionally, the distinction between a clayey sand (SC) and fully saturated poorly graded sand (SP) was not possible without this ground truth as their bulk resistivity values were nearly identical due to the highly saline pore water. A laboratory based electrical resistivity test was conducted on a sample of fully saturated poorly graded sand (SP) that was collected from the riverbed at the Lakin site to validate the resistivity values shown in the inverted ERI surveys. A resistivity value of approximately 15 Ω m was obtained using a Collins Model 54A - Soil Resistivity Bridge, which was consistent with the in situ resistivity values of the saturated alluvium shown in the ERI profiles.

Table 3.3: Soil properties and USCS classification for soil samples collected from each ERI survey site

Soil Properties	Hartland Riverbed	Lakin Riverbed	Holcomb Riverbed	Lakin Riverbank
USCS Classification	SP	SP	SP	SC
K_{sat} (m/day)	13.60	23.79	No Measurement	No Measurement
D_{50} (mm)	0.65	1.00	0.99	0.076

The top 7 m of the Hartland site consists of poorly graded sand with gravel (SP) according to a borehole log less than 1 km to the east of the site, which is shown in Figure 3.3a. This is consistent with the grab sample in Table 3.3, providing ground truth for the closest borehole. Groundwater was encountered at a depth of approximately 1 m in the test hole in March of 2016, which is consistent with the depth to water observed in the nearest monitoring well. ERI surveys were conducted at the Hartland site in September of 2015 (Figure 3.6a), and March of 2016 (Figure 3.6b).

The two ERI surveys shown in Figure 3.6 imaged three horizontal resistivity layers. A high resistivity layer (greater than 60 Ω m) makes up the top 1 m of the surface. A low resistivity zone (less than 20 Ω m) stretches from -1 to -7 m in both surveys. The depth to the low resistivity zone (1 m) is consistent with the depth to water observed in the test hole. A layer of moderate resistivity (between 30 to 60 Ω m) is imaged below a depth of -7 m. The hydrogeologic cross section illustrated by Figure3.1 shows a shale formation is present approximately 7 m below the

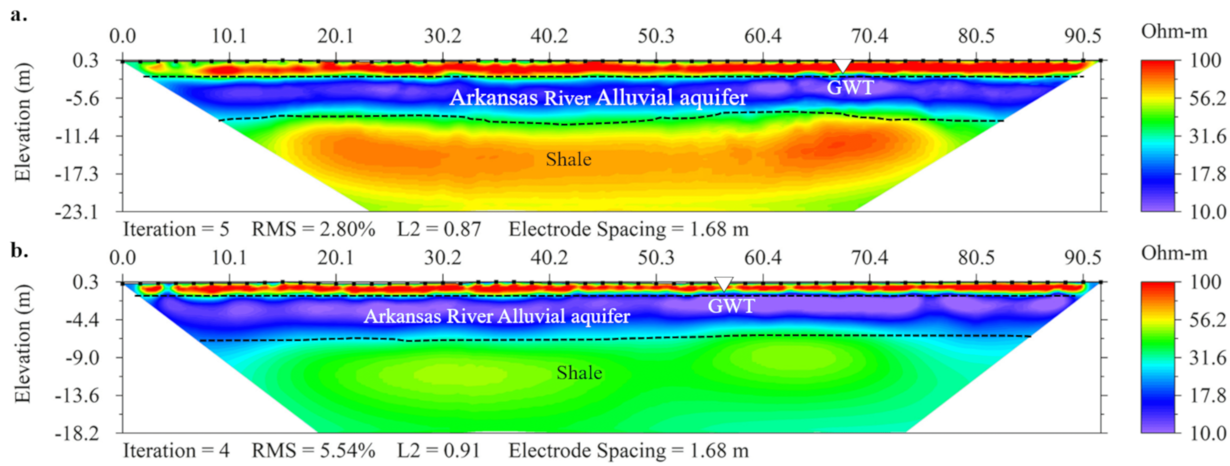

Figure 3.6: Inverted ERI profiles from Hartland, Kansas. a) Land based 56 electrode ERI survey conducted in September 2015. b) Land based 56 electrode ERI survey conducted in March 2016.

surface, which is consistent with depth to the bottom resistivity layer in both ERI surveys.

ERI surveys conducted at Lakin are shown in Figure 3.7. The river stage decreased by 0.3 m between the July survey (Figure 3.7a) and September survey (Figure 3.7b), and the width of the inundated riverbed decreased from 24 m to 10 m. Soil samples were collected from both the riverbank and riverbed, and were classified as a clayey sand (SC) and a poorly graded sand (SP), respectively. These two samples provided a way to distinguish the difference in soil type between the riverbed and riverbank as their bulk resistivity values were nearly identical (15 Ω m). This was in large part due to the effect of the low pore fluid resistivity on the resistivity measurements conducted within the riverbed. In Figure 3.7a, a low resistivity layer (less than 20 Ω m) makes up the top 1 m of the surface to the left and right of the inundated riverbed. A moderate resistivity layer (between 20 Ω m and 40 Ω m) ranges from an elevation of -1 m to -7 m, and stretches laterally across the profile from 48 m to 96 m. At a depth of approximately -7 m, a low resistivity layer (between 15 to 20 Ω m) extends to the bottom of the survey and stretches laterally across the profile. At 42 m along the profile, a region of low resistivity (20 Ω m) stretches from the riverbed surface through the moderately resistive layer. Figure 3.7b shows the ERI survey conducted in September 2016 along the same transect shown in Figure 3.7a. While the same basic resistivity structure exists in Figure 3.7b, the area of moderate resistivity (unsaturated zone) stretching laterally from 48 m to 96 m increased in thickness and experienced a 10 Ω m to 20 Ω m increase in resistivity. The bottom resistivity layer (saturated zone) experienced small changes (less than 5 Ω m) in resistivity.

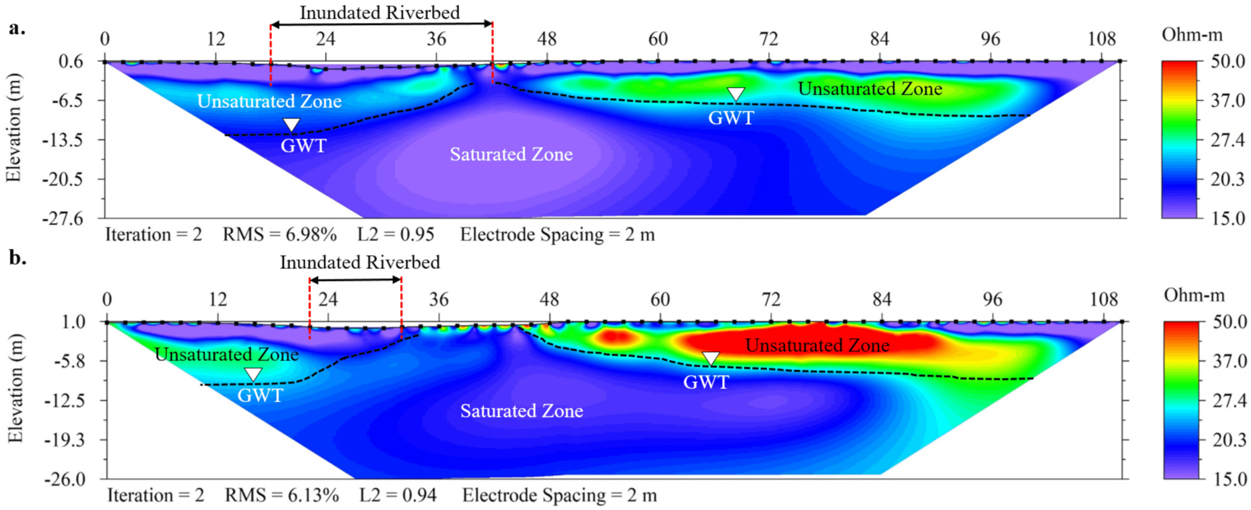

Figure 3.7: Inverted ERI profiles from Lakin, Kansas. a) Land based-underwater 56 electrode ERI survey conducted in July 2016. b) Land based-underwater 56 electrode ERI survey conducted in September 2016.

A dry, land-based ERI survey was conducted parallel to the Arkansas River at the Lakin site (Figure 3.8). This survey was located 0.25 km to the west of the surveys shown in Figure 3.7, as shown in b. Only one survey was conducted at this site as the Arkansas River inundated the entire survey area shortly after the survey was conducted. Soil samples collected from the surface were classified as clayey sand (SC) (between 0 m to 50 m) and poorly graded sand (SP) from 50 m to 82 m. The vegetative cover changed across the site as grass was present at the surface from 0 m to 50 m, while a grove of salt cedars was present from 50 m to 82 m. The relevance of the soil type within the top 1 m across the site as it relates the the vegetation present is included in the discussion.

A low resistivity zone (less than 20 Ω m) makes up the top 2 m of the profile from 0 m 50 m. A moderate resistivity layer (25 Ω m) stretches from 50 m to 82 m along the profile and extends to an elevation of -5 m. Resistivity values decrease from 25 Ω m to less than 20 Ω m below a depth of 5 m from left to right across the profile.

Large differences in the subsurface resistivity distribution are seen between the two ERI surveys conducted at the Holcomb site, which are shown in Figure 3.9. This was expected as the July 2016 survey, shown in Figure 3.9a, was conducted when the river was flowing and the September 2016

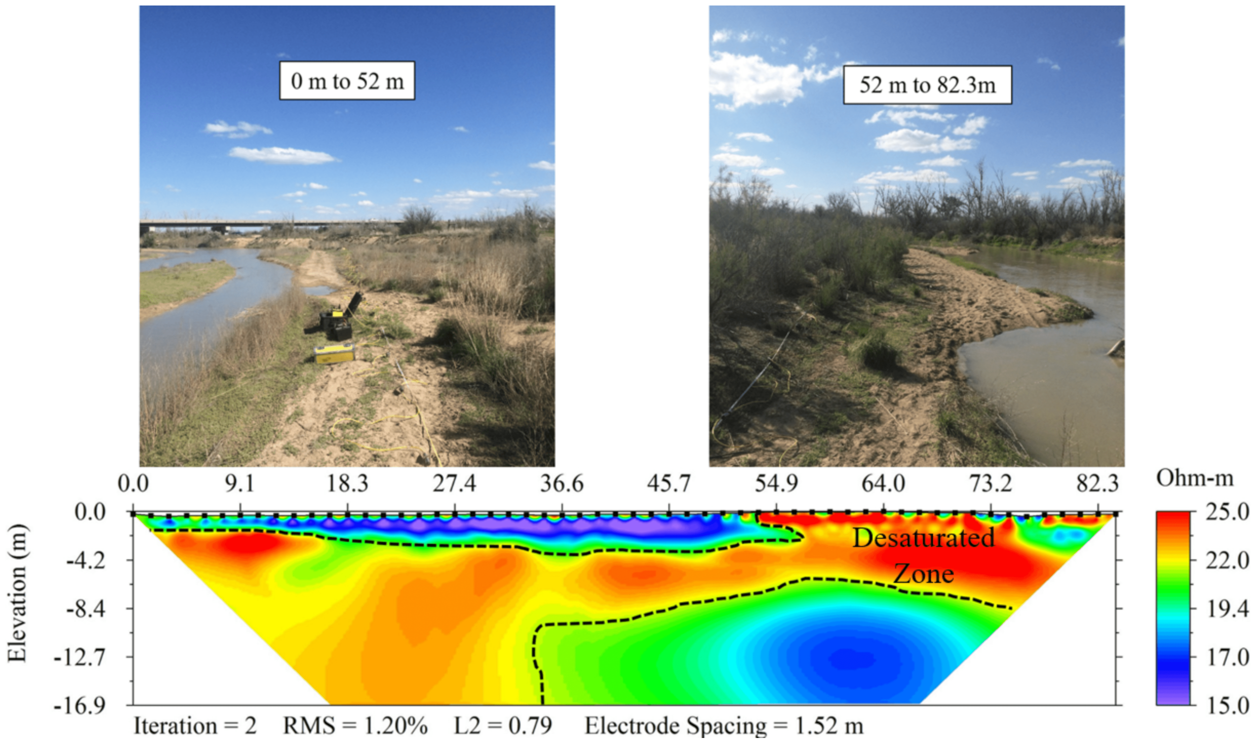

Figure 3.8: Lakin, Kansas – Land based 56 electrode ERI survey conducted along the south riverbank at the Lakin site in March 2016.

survey, shown in Figure 3.9b, was conducted when the riverbed was dry. Only 28 electrodes were used to collect these datasets as available survey space was limited by the densely vegetated riparian zones bordering the river channel. In Figure 3.9a, a zone of low resistivity (less than 20 Ω m) stretches from just below the riverbed surface downward to -8 m between 17.9 m and 23.9 m along the transect. The resistivity structure of this image is more discontinuous and less uniform than the images collected at the Hartland and Lakin sites. The resistivity within the top 3 m of the surface ranges from 15 Ω m to 50 Ω m across the transect. Figure 3.9b shows an ERI survey that was offset 6 m northeast (right) of Figure 3.9a. This transect was offset because the electrodes were unable to penetrate the compacted riverbank at the time of the survey due to dry surface conditions. The resistivity is generally greater than 150 Ω m between the surface and -4 m (unsaturated zone). A low resistivity region (saturated zone) was observed below -4 m.

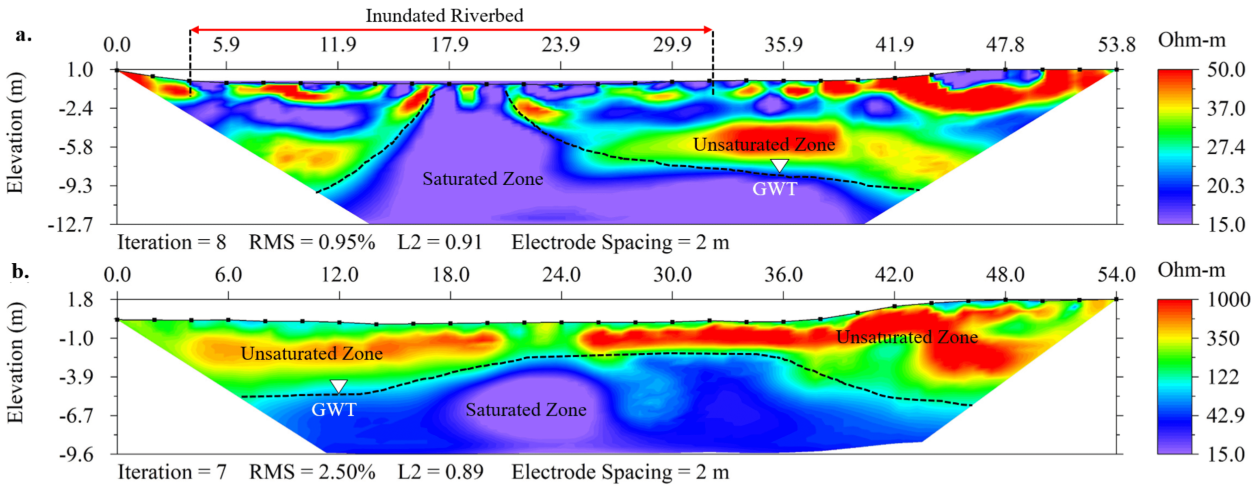

Figure 3.9: Inverted ERI profiles from Holcomb, Kansas. a) Land based-underwater 28 electrode ERI survey conducted in July 2016. b) Land based 28 electrode ERI survey conducted in September 2016.

3.5 Discussion

The ERI profiles in this study presented a detailed depiction of the subsurface alluvial environment through which river-aquifer interactions occur. The spatial distribution of electrical resistivity effectively delineated the location of the groundwater table adjacent to and beneath the riverbed. Additionally, fully saturated and unsaturated areas below the riverbed were identifiable by sharply contrasting resistivity bodies. The discontinuous resistivity distribution observed beneath inundated portions of the riverbed at Holcomb show the transient nature of riverbed infiltration, and the role it plays in groundwater-surface water exchange. These results provide hydrologic information that is necessary to characterize the hydrologic connectivity at specific points in time, which can be correlated to observational head data to more reliably assess the connective state of the river-system.

The ERI surveys conducted adjacent to the Arkansas River upstream of the Bear Creek fault at the Hartland site (Figure 3.6) were consistent with the conceptualized flow system shown in Figure 3.5a. The depth to water table below the land surface within the Arkansas River Alluvial aquifer was interpreted to be between 1 m to 2 m in both surveys, which is supported by the hydrograph shown in Figure 3.4b. The resistivity values observed in the bottom resistivity layer of both profiles are within the range of resistivity for shale (1 Ω m to 500 Ω m) as reported by Everett (2013).

The ERI surveys conducted at the Lakin site (Figure 3.7) imaged a three layered resistivity system below the Arkansas River. The spatial distribution of resistivity below the inundated riverbed is interpreted to be consistent with a fully connected river-aquifer system as conceptualized in Figure 3.5b. The low resistivity zone below -7 m likely represented fully saturated alluvial material (coarse-grained). The bottom low resistivity zone (below -7 m) stretched laterally across the profile in both surveys, but also extended to the riverbed surface at 42 m along the profile. The zone of low resistivity extending to the riverbed surface appears to represent a fully saturated region that is connected to the riverbed. Therefore, the two ERI surveys in Figure 3.7 show that the Arkansas River and Arkansas River Alluvial aquifer remained fully connected across a 0.3 m decrease in stream stage.

The survey parallel to the Arkansas River at Lakin (Figure 3.8) identified how differences in vegetation within the riparian zone can be used to identify the underlying hydrogeologic environment within the alluvium. Ahring and Steward (2012) demonstrated that salt cedars have the ability to tap groundwater from depths as great as 10 m, and often inhabit areas with higher saturated hydraulic conductivity. The high resistivity zone below the salt cedars extends to an elevation of -5 m (from 50 m to 82 m) in Figure 3.8, which likely represents the rooting depth of the salt cedar grove. The higher resistivity of this region indicates that the sediments are likely unsaturated and at a lower water content than the surrounding background as a result of phreatophyte root water uptake. Figure 3.8 supports the contributions of Ahring and Steward (2012), and highlights the need to further investigate riparian areas with high and low densities of phreatophytes to be able to identify productive recharge zones.

A discontinuous resistivity distribution is seen in the two ERI surveys conducted at Holcomb. Figure 3.9a displays a low resistivity zone (less than 20 Ω m) between 17.9 m and 23.9 m extending downward through the profile. The survey shown in Figure 3.9a was conducted shortly after a high flow event inundated the riverbed (between 4 m and 38 m). Prior to the flow event, the width of the inundated riverbed at Holcomb was less than 10 m. The alluvial material to the left and right of 17.9 m in Figure 3.9a exhibited resistivity values between 20 to 50 Ω m. These regions appeared to be variably saturated and located above the groundwater table, which was interpreted to be located at just above -8.5 m in July 2016. This interpretation was supported by the Holcomb well hydrograph in Figure 3.4b, as the depth to water below the riverbed in April 2016 was approximately 8 m. The ERI survey shown in Figure 3.9b was conducted under extremely dry surface conditions (no river flow) after the river flow receded upstream of the site. The high resistivity values (350 Ω m to 1,000 Ω m) within the top 5 m were interpreted to be desaturated coarse grained alluvial material. The region of low resistivity below -5 m was interpreted to be fully saturated alluvial material. The transition from partially saturated to fully saturated alluvial material between 4 m and 38 m between the surface and -8.5 m (i.e., groundwater table) illustrates a disconnection between the Arkansas River and Arkansas Alluvial aquifer. The hydrologic interpretation of these ERI surveys disproved the hypothesized conceptualization of a disconnected losing river in Figure 3.5c. The low and high resistivity regions near the surface in Figure 3.9a show that the riverbed was likely connected and disconnected to the water table during July 2016.

The ERI surveys support the conceptualized model of the connection regime between the Arkansas River and Arkansas River Alluvial aquifer at Lakin, however, the hypothesized conceptualization at Holcomb is disproved by the discontinuous resistivity distribution below the inundated riverbed. The change from a fully connected system to a partially disconnected system occurred within the stretch of the river between Lakin and Holcomb, which indicated that seepage losses from the river were greater near Holcomb. The response of the groundwater table across the region, shown in Figure 3.4, corroborated this claim as the magnitude of the groundwater table response was larger at Holcomb than it was upstream near Deerfield between 2016 and 2018. A study conducted by Shanafield et al. (2012) showed that the disconnected water table response to increases in stream stage are generally greater than the water table responses in a connected system. This study provides a way to gather critical hydrologic information below losing rivers that is not always attainable with existing hydrologic data. The transient nature of river discharge and riverbed infiltration make the distinction of the hydrologic connection with hydrologic data difficult. The results of this study show the effectiveness of ERI as method for improving the characterization of river-aquifer connectivity.

3.6 Conclusions

Groundwater depletion in excess of natural recharge has resulted in the decline of groundwater levels within the Arkansas River valley across Western Kansas over the past century. Consequently, the Arkansas River has transitioned from a groundwater fed stream to a losing stream over the past 50 years. Recharge processes between the Arkansas River and the underlying Arkansas River Alluvial aquifer and Ogallala aquifer are difficult to conceptualize with the existing river gauge, borehole, and well data. Modeling localized groundwater-surface water interactions requires a detailed understanding about river-aquifer connectivity. This study examined the hydrologic connectivity between the Arkansas River and Arkansas River Alluvial aquifer through the analysis of existing hydrogeologic data and application of ERI surveys.

Conceptualizations of the hydrologic connection at three locations along the river valley were initially constructed from borehole lithology and water table response data. Cross-river ERI surveys of the the localized flow systems were performed to further examine the validity of the hypothesized conceptualizations. The spatial distribution of electrical resistivity below the riverbed identified regions of unsaturated and fully saturated sediments beneath portions of the inundated riverbed, and identified the location of the groundwater table beneath and adjacent to the riverbed. Soil sample analysis aided in the interpretation of the near surface sediments and was used to distinguish the difference between contrasting soil types exhibiting similar bulk resistivity values. The results of this study provide hydrologic details that are critical to accurately model of stream-aquifer interactions (i.e., depth to the water table beneath the riverbed, hydrologic connection between the river and water table). Merging hydrologic data with near-surface geophysical methods provides a way to reliably assess the hydrogeologic factors that have a direct causative effect on groundwater recharge through riverbeds.

While ERI is used to study groundwater-surface water interactions across many regions of the world, this is the first known application of ERI to study groundwater-surface water interactions over an important Ogallala aquifer region of Western Kansas. Future analysis of stream-aquifer interactions should focus on coupling measurements of soil physical properties and hydrologic state variables below riverbeds with geophysical instrumentation to better constrain the mechanisms controlling alluvial recharge processes.

3.7 Acknowledgments

Support for this project was provided by the USDA Ogallala Aquifer Project. We would also like to thank Southwest Kansas Groundwater Management District (GMD3) and the land owners for their assistance and cooperation.

Chapter 4

Transient Analysis of Electrical Resistivity

Aquifer depletion contributes to an evolution in the hydrological exchanges between groundwater and surface water. This problem is studied in a region overlying the Ogallala Aquifer where regional rivers, such as the Arkansas River in Western Kansas, were fed by groundwater prior to the development of widespread irrigated agriculture and the occurrence of depleting groundwater stores (Gutentag et al., 1984). This region has surpassed the threshold of peak groundwater declines, and previous consumption rates of groundwater can no longer be sustained by the Ogallala aquifer to support irrigated agriculture (Steward and Allen, 2016). Furthermore, replenishing groundwater levels to predevlopment conditions through natural recharge processes would require decades to centuries in some regions (Steward et al., 2013). The losing rivers in this region play an important role in the regional water balance as they serve as primary sources of groundwater recharge (Whittemore, 2002), and provide a source of recharge to the underlying Ogallala formation (Whittemore, 2002; Steward and Allen, 2016). The recharge occurring beneath the ephemeral Arkansas River follows the flow regimes between surface water and groundwater typical of stream-aquifer interactions (Sophocleous, 2005; Brunner et al., 2009). This chapter assesses the temporal response of the flow regimes conceptualized in Figure 3.5 in Chapter 3 by interpreting the temporal changes in electrical resistivity measurements. Although there have been many uses of ERT to study different components of hydrologic systems, a novel interpretation of temporal resistivity dynamics is proposed by incorporating insight gained from vadose zone modelling. The rate of recharge leaves a signature that is decipherable through measurements of pressure head in the vadose zone (Pullan, 1990). Specifically, Steward (2016) showed that changes in recharge rate result in different patterns of pressure head distribution for layered soils with inclusions. A coarse soil embedded within a fine grained soil behaves differently than a fine grained soil embedded within a coarse grained soil, and these differences provide the perspective necessary to elucidate the spatial and temporal response of the vadose zone to changes in recharge rate (Steward, 2016).

4.1 Site Selection and Methodology

Selection of three ERT survey sites (i.e., Figure 3.3 in Chapter 3) along the Arkansas River were chosen to study the hydrologic response of sediments under baseflow conditions and losing conditions. Each site contained unique hydrologic and hydrogeologic aspects, such as the depth to bedrock, depth to water table, and hydrologic connection between the river and saturated zone.

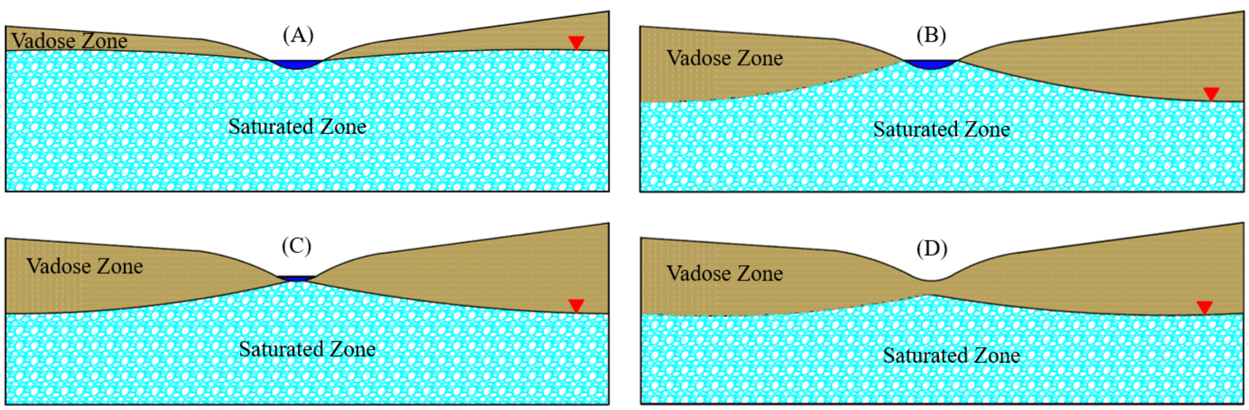

Figure 4.1: Schematic showing different types of hydrologic connection between groundwater and surface water as the system evolves from gaining to losing conditions; (A) stream is groundwater fed, (B) streambed and saturated zone are fully connected, (C) streambed and saturated zone may be partially connected, (D) streambed and saturated zone and are disconnected by a vadose zone.)

The Hartland site overlies the Arkansas Alluvial Aquifer upstream of the Bear Creek fault where the Ogallala formation is not present. Bank storage provides baseflow to the river at Hartland during low flow periods, and the river sustains groundwater levels within the alluvial aquifer during higher flows (Whittemore, 2002). The Lakin site is located 6 km downstream of the Bear Creek fault, where seepage losses from the river to underlying Arkansas Alluvial and Ogallala

Aquifers are known to occur (Whittemore, 2007). The river and alluvial aquifer are fully to partially connected near Lakin as the depth to water below the land surface is generally less than 10 m within the alluvium. The Holcomb site was chosen because of the highly periodic Arkansas River flows that occur there, which allowed for surveys to be conducted across a dry and inundated riverbed.

Electrical resistivity measurements are conducted by injecting electrical current into the subsurface through an electrode pair (current pair) while simultaneously measuring the induced voltage potential between a separate electrode pair (potential pair). Repeated sets of measurements using various electrode configurations are conducted in an ERT survey to collect an apparent resistivity psuedosection. The SuperSting Earth Resistivity Induced Polarization and Self Potential System from Advanced Geosciences Inc. was used to conduct all ERT surveys in this study, and all data were processed with EarthImager 2D (AGI, 2007). ERT surveys were conducted with submersible and dry electrode cables in series when aligned perpendicular to the Arkansas River. A dipole-dipole array was used to conduct all the surveys used for the temporal comparison. The water depth was measured at each submersed electrode, and the resistivity of the river water was also measured at the time of each survey. The water body was set to the measured resistivity value and held constant during the inversion. The terrain used to invert the background resistivity images is included within the time-lapse profiles. Table 4.1 gives a summary of survey details and the misfit of each background survey used for the temporal comparision. Additional details about the experimental setup of the baseline resistivity profiles and their hydrogeologic interpretations can be found in Chapter 3.

Table 4.1: Survey Details

Site	**Date**	RMSPE	**L2-norm**	**Spacing**	**Water Resistivity (Ω m)**
Hartland	Sept. 2015	9.77%	0.95	1.68 m	2.35
Hartland	March 2016	8.50%	0.72	1.68 m	2.56
Lakin	July 2016	6.98%	0.95	2.00 m	5.30
Lakin	Sept. 2016	6.13%	0.94	2.00 m	2.90
Holcomb	July 2016	2.92%	0.87	2.00 m	2.90
Holcomb	Sept. 2016	4.88%	0.96	2.00 m	Dry

The time difference profiles were generated by plotting the percent change in resistivity between the inverted resistivity profiles using generic mathematical software. All surveys were invereted independently from one another. The percent change in resistivity was calculated through Eq. (4.1),

$$\% Change = \frac{\rho_f - \rho_o}{\rho_o} * 100 \tag{4.1}$$

ρ_o is the inverted resistivity from the initial survey, and ρ_f is the inverted resistivity from the final survey. A negative percent change indicates a decrease in resistivity over time and a positive percent change indicates an increase in resistivity over time.

4.2 Temporal Changes in Electrical Resistivity

Temporal changes in resistivity were calculated for survey transects located at Hartland, Lakin, and Holcomb (shown in Figure 3.3 in Chapter 3).. The background resistivity images for this temporal comparison are shown in Figure 3.6 in Chapter 3 as well. The ERT surveys at the Hartland site were conducted in September of 2015 and March of 2016, and the temporal changes in resistivity are shown in Figure 4.2D. These surveys were conducted using 56 electrodes with a spacing of 1.68 m. The river water resistivity was 2.35 Ω m in September 2015 and 2.56 Ω m in March 2016. The hydrologic conditions at Hartland follow those of Figure 4.1A, with a perennial stream and shallow groundwater table. The resistivity increased by an average of 50% between -1 m and -5 m from September 2015 to March 2016, which is attributable to changes in pore fluid resistivity within the saturated zone as a result of fluctuating river discharge. Little to no change in resistivity occurred between -5 m and - 7 m. Resistivity values decreased between 0 and -50% between -7 m and -10 m, which corresponds to the shale/sandstone formation that acts as the base of the Arkansas River Alluvial Aquifer. Below -10 m, changes in resistivity ranged between 0% to 20 %. Bulk resistivity values within this region ranged between 40 to 50 Ω m, and the changes observed within this region are not significant in terms of understanding the temporal response of the overlying alluvial sediments to changes in streamflow.

The Lakin site is down-gradient of the Bear Creek fault, and ERT surveys were conducted in July and September of 2016 with changes in resistivity shown in Figure 4.3D. The background

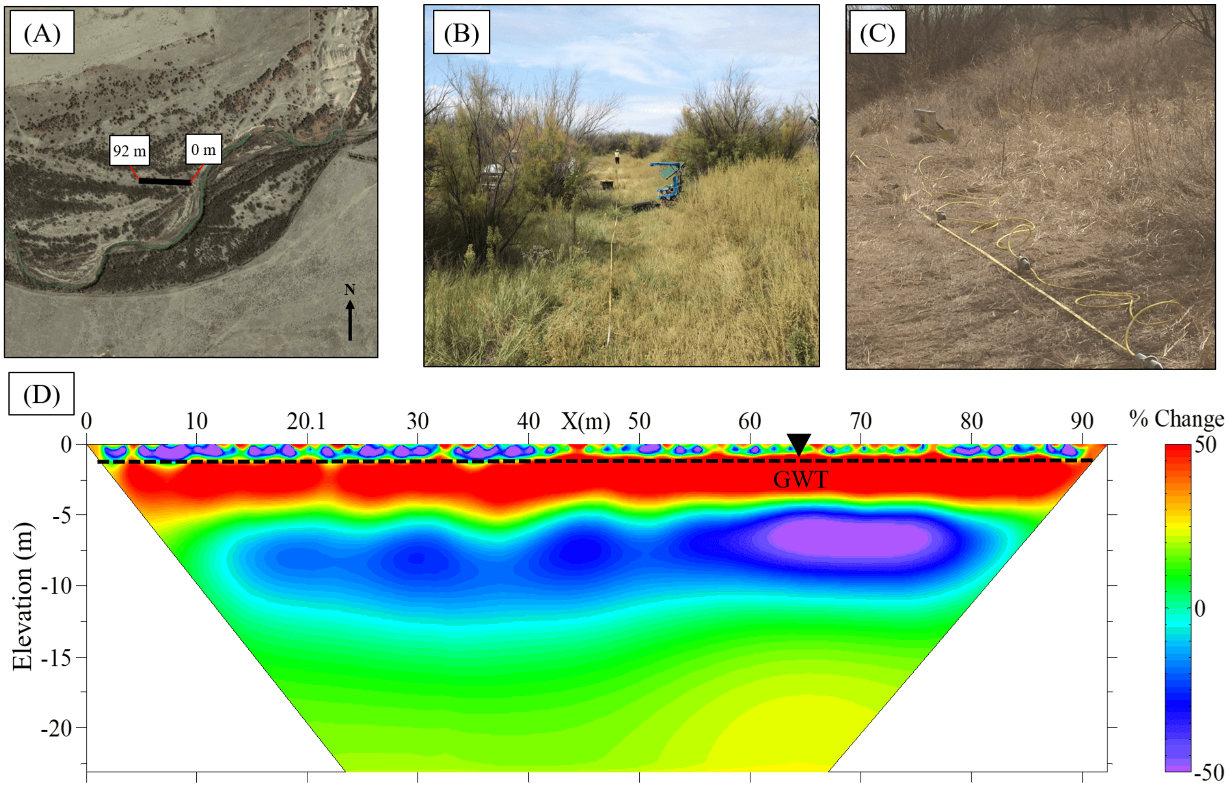

Figure 4.2: Hartland Site (Seasonal Baseflow Conditions); (A) Aerial view of survey location; (B) ERT survey setup in September 2015 ; (C) ERT survey setup in March 2016; (D) Change in resistivity between September 2015 and March 2016. The river is to the right (south) of the survey lines shown in Figure 4.2A and Figure 4.2B

resistivity images for this comparison are shown in Figure 3.7 in Chapter 3. These surveys were conducted with 56 electrodes with a spacing of 2.0 m. The river water resistivity was 5.30 Ω m in July 2016 and 2.90 Ω m in September 2016. These surveys crossed the river, and the difference in resistivity between high and low flow periods (Figure 4.1B to Figure 4.1C) illustrate two recharge zones below the riverbed. The recharge zones experienced a -10 % to -20% decrease in resistivity, and these changes within the saturated zone are in response to increases in pore fluid salinity as a result of decreased river discharge. The Arkansas River generally exhibits higher salinity during low flow periods (Whittemore, 2000). The oblong shape and lateral spreading of the recharge zones (between 24 m and 84 m) indicate that the hydraulic properties within the alluvium may exhibit a degree of anisotropy. Additionally, a confining unit may exist between the alluvial aquifer and underlying Ogallala aquifer, which would promote more lateral flow within the alluvial deposits. A dewatered zone is illustrated between 60 m and 84 m within near surface sediments above the groundwater table.

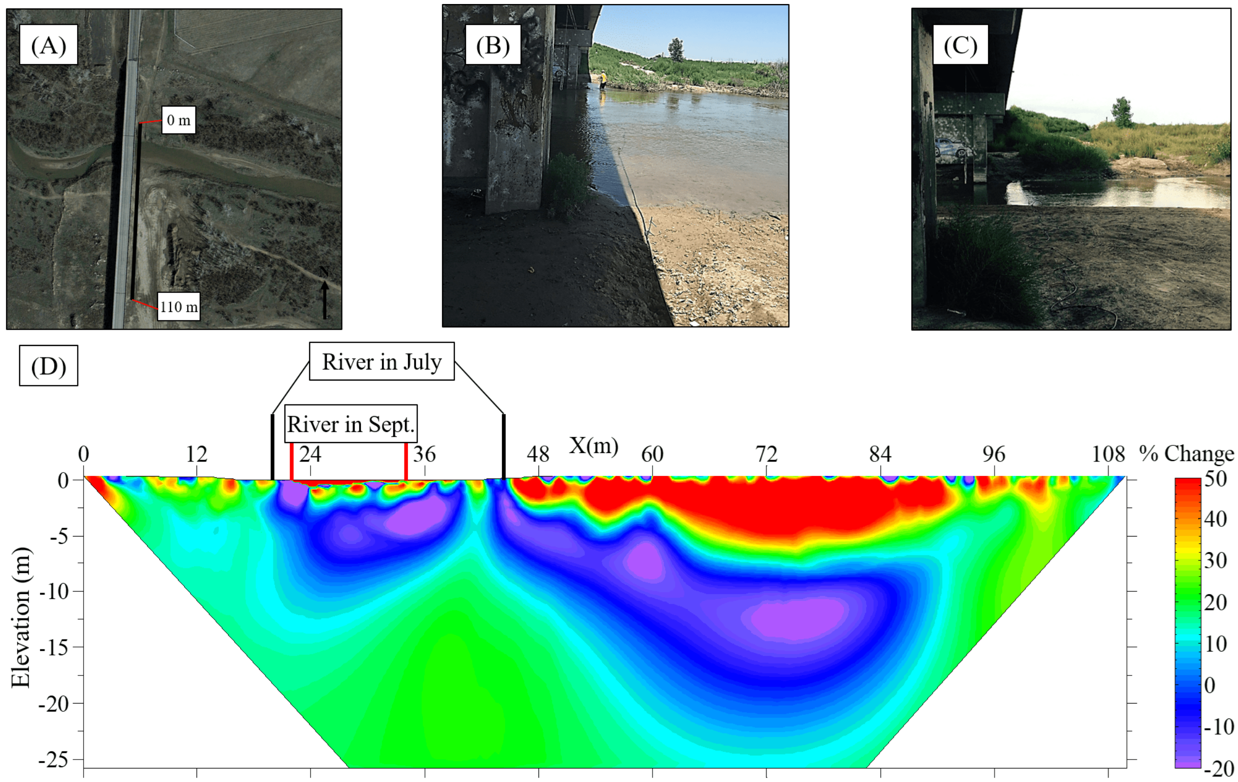

Figure 4.3: Lakin Site (Transitional to Fully Connected Losing River); (A) Aerial view of survey location; (B) ERT survey setup in July 2016; (C) ERT survey setup in September 2016; (D) Percent change in resistivity between July 2016 and September 2016

The site at Holcomb (Figure 4.4) is furthest down-gradient of the Bear Creek fault, and surveys were conducted during the midst of a high flow event (July 2016) and during no flow conditions (September 2016). These surveys were conducted with 28 electrodes with a spacing of 2.0 m. The river water resistivity was 2.90 Ω m during the July 2016 survey. The changes in resistivity at this site are much larger than those observed at Hartland and Lakin, which was expected given that the river transitioned from flow conditions (July 2016) to a completely dry state (September 2016). The changes in resistivity shown in Figure 4.4D illustrate dewatered sediments (blue to red zones) above the remainder of an ephemeral groundwater mound (purple zones). The large changes in resistivity at Holcomb show the implications surface water transience has on the interactions between groundwater and surface water, and the need to analyze the connective state across transitional periods.

No temperature corrections were made prior to interpreting the temporal changes in resistivity. The surveys at the Lakin and Holcomb sites were all conducted during the summer months (during July and September) where surface water and groundwater temperatures are quite stable. Regions below the groundwater table were assumed to exhibit little to no temperature variation. The groundwater temperature within the Arkansas River Alluvial Aquifer varies by less than 0.5 degrees Celsius annually according to a monitoring well near the Kansas-Colorado state line (i.e., Figure 3.2 in Chapter 3) .

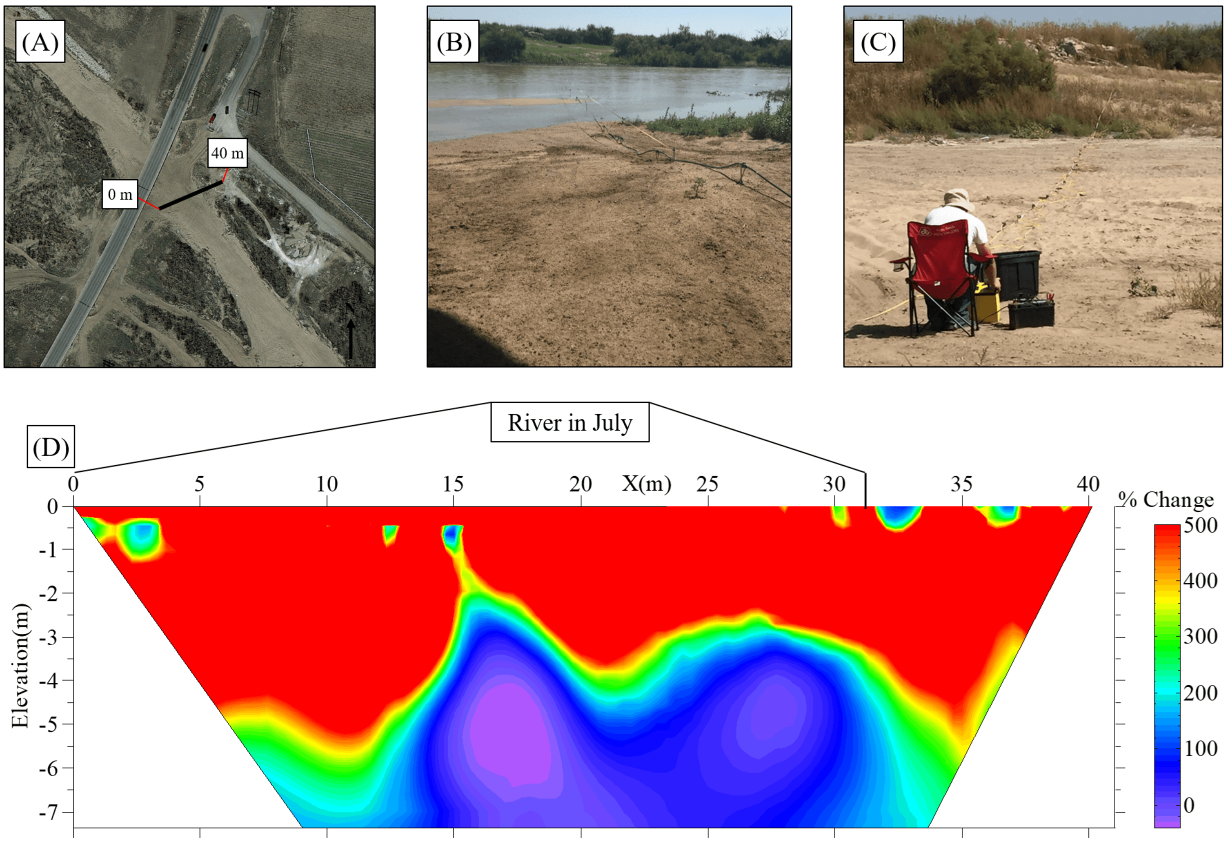

Figure 4.4: Holcomb Site (Disconnected losing river); (A) Aerial view of survey location; (B) ERT survey setup in July 2016 ;(C) ERT survey setup in September 2016; (D) Change in electrical resistivity between July 2016 and September 2016

The time difference profiles in this chapter delineate the pathways of recharge from surface water to groundwater across perennial and ephemeral reaches of the Arkansas River. The state of connectivity between the river and alluvial aquifer becomes revealed by analyzing the changes in electrical resistivity of riverbed sediments in response to seasonal changes river discharge. While temporal changes in resistivity are commonly used to map changes in water content (Descloitres et al., 2008; Daily et al., 1992), the use of temporal changes in electrical resistivity to detect the difference in the rate of groundwater fluxes within alluvial environments is less common due to complex site conditions (i.e., heterogeneity, differences in pore water temperature and salinity) and the assumptions required to use well established petrophysical relationships, such as Archie's Law (Archie, 1942) to relate resistivity to water content. Insights gleaned from Steward and Allen (2016) showed that large variations in pressure head distributions occur within fine grained inhomogeneities well above the groundwater table across shifts in recharge. Therefore, localized temporal changes in electrical resistivity between survey periods may provide an indication of not only a fine grained inhomogeneity, but a shift in the rate of groundwater recharge, as changes in pressure head directly correspond to detectable changes in water content. Therefore, ERT surveys could be conducted across periodic shifts in river discharge to better understand how river discharge is related to the rate of recharge in hetergeneous groundwater systems.

Chapter 5

Methods

5.1 Electrical Resistivity Tomography

Electrical resistivity tomography (ERT) is a near surface geophysical method that measures voltage differences at the earth's surface to determine the spatial distribution of electrical resistivity of the underlying geologic material. A voltage measurement is obtained by inducing an electric field/equilibrium voltage between a source/sink electrode pair, and by measuring the resulting voltage difference between a potential electrode pair at a specified distance away from the source/sink pair. Repeated sets of voltage measurements are conducted for different electrode configurations and spacings to obtain an apparent resistivity psuedosectoin that provides information about the spatial distribution of electrical properties. The apparent resistivity is defined as the resistivity of a homogeneous halfspace. Hence, an inversion process is carried out to determine the true resistivity distribution responsible for the measured surface voltage potentials.

All ERT surveys in this research were conducted using both 28 and 56 electrode arrays with an electrode spacing ranging between 1.5 m to 2.0 m. Survey transects were shortened where dense vegetation bordered the river channel. Data were collected using either a dipole-dipole or dipole-dipole/Schlumberger array. Although surface based measurements are more popular, submersible electrodes allow surveys to be conducted below water to image submerged sediments. Mixed surface and underwater surveys require the electrical resistivity of the water body to be measured as it is a needed parameter in the inversion scheme. Additional details regarding the ERT surveys conducted in this research can be found in the methods section of Chapter 3 and Chapter 4.

5.2 Classical Theory of Electrostatics

A governing set of partial differential equations are developed from the fundamental equations of electrostatics. Gauss's law (Maxwell's first equation) relates the volume charge density within a dielectric region to the divergence of the E-field

$$\nabla \cdot E = \frac{\rho}{\epsilon_0 \epsilon_r} \tag{5.1}$$

where E is the electric field, ϵ is the electric permittivity, and ρ is the charge density. The electric field is related to the gradient of the electric potential

$$E = -\nabla \Phi \tag{5.2}$$

Substituting Eq. (5.2) into Eq. (5.1) gives the Poisson equation

$$\nabla \cdot \nabla \Phi = -\frac{\rho}{\epsilon} \tag{5.3}$$

which can be rewritten.

$$\nabla^2 \Phi = -\frac{\rho}{\epsilon} \tag{5.4}$$

If the source charge is located outside of the problem domain, the problem reduces to the Laplace equation,

$$\nabla^2 \Phi = 0 \tag{5.5}$$

where the Laplacian of the electric potential is equal to zero. The electric displacement field D and the current density field J can be related to the electric field through two constitutive relationships.

The electric displacement is linearly related to the electric field through the electric permittivity. The current density J is also linearly related to the electric field through the electrical conductivity σ.

$$D = \varepsilon E \tag{5.6}$$

$$E = \sigma J \tag{5.7}$$

These relationships can also be written in terms of the electrical resistivity ρ, which is simply the reciprocal of the electrical conductivity $\rho = 1/\sigma$. In the case when an electric field is produced within an inhomogeneous medium, interface conditions must be satisfied across the discontinuity in soil properties occurring between two adjacent geologic mediums.

5.3 Analytic Element Method

The AEM formulation of electrical conduction through rectangular elements is taken from Steward (2020a). The geometry of a typical rectangular element with evenly spaced control points is illustrated by Figure 5.1.

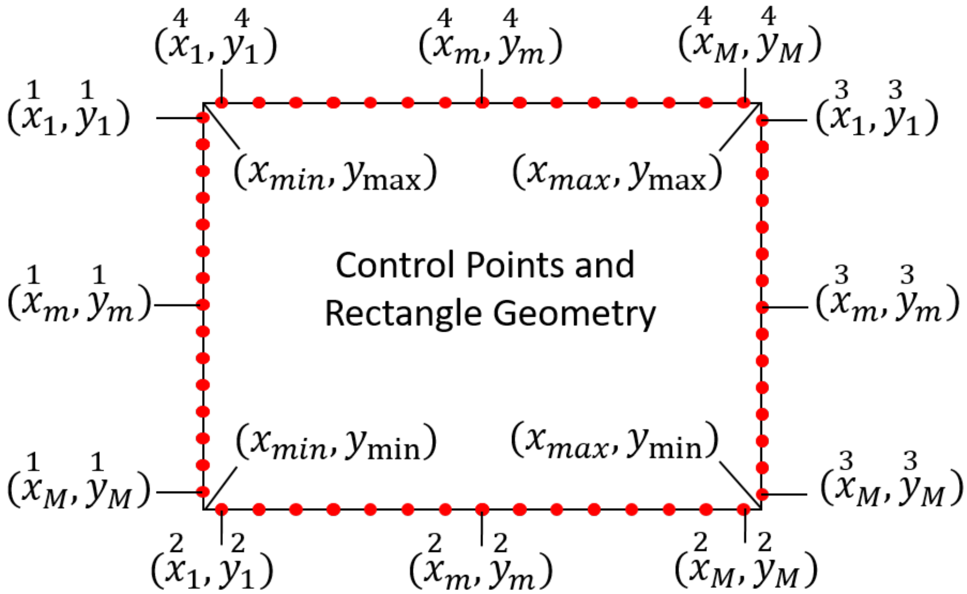

Figure 5.1: Rectangle geometry and control points evenly spaced around each side of the rectangle. The number of control points M may vary depending upon the number of times the Fourier Serires terms are repeated across each rectangle side δ

The location of the control points for each side can be written in terms of the minimum and maximum x and y dimensions for each side of a rectangle.

$$
\begin{aligned}
&\overset{1}{x}_m = x_{min}, \quad \overset{1}{y}_m = y_{min} + (y_{max} - y_{min})\frac{m - \frac{1}{2}}{M} \\
&\overset{2}{x}_m = x_{min} + (x_{max} - x_{min})\frac{m - \frac{1}{2}}{M}, \quad \overset{2}{y}_m = y_{min} \\
&\overset{3}{x}_m = x_{min}, \quad \overset{3}{y}_m = y_{min} + (y_{max} - y_{min})\frac{m - \frac{1}{2}}{M} \\
&\overset{4}{x}_m = x_{min} + (x_{max} - x_{min})\frac{m - \frac{1}{2}}{M}, \quad \overset{4}{y}_m = y_{min}
\end{aligned}
\tag{5.8}
$$

5.3.1 Electrostatic Boundary Conditions

Boundary and interface conditions for 2D solution of Laplace's equation in a charge free region of space are developed in the following section. Continuity conditions for the normal component of the current density field, normal component of the displacement field, and potential (voltage) across vertical and horizontal interfaces separating two mediums with different electrical properties are illustrated in Figure 5.2.

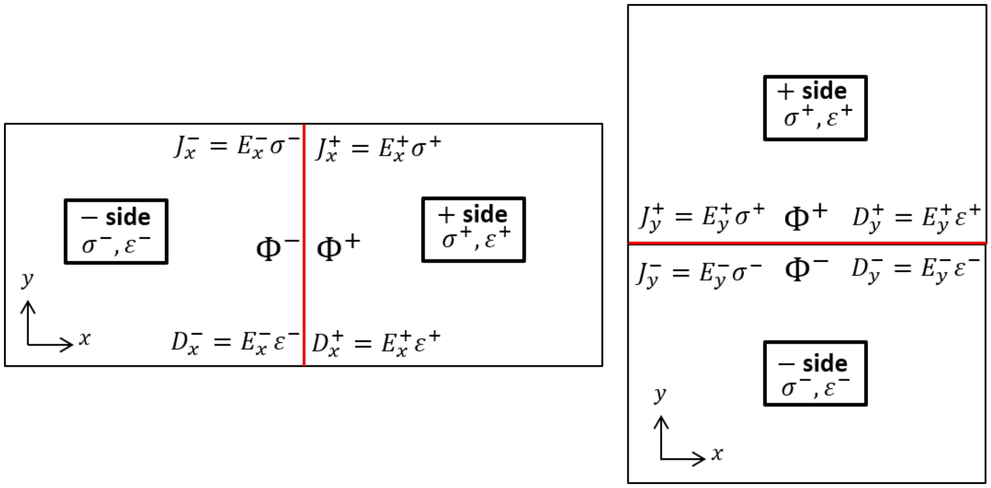

Figure 5.2: Rectangular elements with different electrical properties (σ, ε) separated by a vertical interface (left) and horizontal (right) interface. The normal components of the electric current density field and electric displacement field are derived in terms of the electric field, electrical conductivity, and electrical permittivity. Continuity of potential must also be satisfied across the interface.

The continuity of potential across an interface is written,

$$\Phi^- = \Phi^+ \tag{5.9}$$

where Φ^- and Φ^+ is the voltage on each side of the interface. The continuity of the normal component of the current density field is given by multiplying the normal component of the electric field on each side of the interface by the respective electrical conductivity on each side of the interface,

$$E_N^- \sigma^- = E_N^+ \sigma^+ \tag{5.10}$$

where E_N^- and E_N^+ are the normal components of the electric field of the two different mediums, and σ^- and σ^+ are the electrical conductivity values of each homogeneous and isotropic medium. The jump in the normal component of the E field also requires that the tangential component of the E field be continuous across an interface separating two adjacent mediums.

$$E_T^- = E_T^+ \tag{5.11}$$

The normal component of the electric displacement field D is continuous across an interface, which is given by multiplying the normal component of the electric field on each side of an interface by the respective electrical permittivity

$$E_N^- \epsilon^- = E_N^+ \epsilon^+. \tag{5.12}$$

It is convenient to represent the tangential and normal components of the electric field in terms of the gradient of the electric potential. The x and y components of the electric field can be written

$$\frac{\partial \Phi}{\partial x} = E_x = E_N; \frac{\partial \Phi}{\partial y} = E_y = E_T \tag{5.13}$$

for the case when two rectangles are separated by a vertical interface, and

$$\frac{\partial \Phi}{\partial x} = E_x = E_T; \frac{\partial \Phi}{\partial y} = E_y = E_N \tag{5.14}$$

when two rectangles are separated by a vertical interface.

Nuemann boundary conditions were applied to the exterior of the model domain in this study. The normal component of the electric field along the exterior boundaries can be written in terms of the electric potential

$$\frac{\partial \Phi}{\partial N} = E_N = 0 \tag{5.15}$$

where the normal component of the E-field is given to be zero. Enforcing a large model geometry relative to the overall problem geometry mitigates boundary effects on the solution when utilizing Nuemann boundary conditions as it essentially insulates the model.

5.3.2 Formulation of Point Sources

Inducing a steady state electric field is achieved through the application of a point sink and point source. The analytical solution for the electric potential in three dimensions within a homogeneous halfspace is written

$$\Phi = \frac{I\rho}{2\pi(r)} \tag{5.16}$$

where I is the magnitude of the applied current, ρ is the electrical resistivity of the homogeneous halfspace, and r is the distance between the point source any point within the half-space. Integrating Eq (5.16) with respect to r gives the analytical solution for the potential distribution arising from a 2D point source applied within a homogeneous halfspace

$$\Phi = \frac{I\rho}{2\pi} ln(r). \tag{5.17}$$

Taking minus the gradient of Eq. (5.17) gives electric field for a 2D point source.

$$E_r = -\frac{\rho I}{2\pi r} \tag{5.18}$$

The radial distance r written in terms of Cartesian coordinates is

$$r = \sqrt{(x_p - x_s)^2 + (y_p - y_s)^2} \tag{5.19}$$

where x_p and y_p are where the potential is to be computed at, and x_s and y_s are coordinate locations of the point sources. Formulating the point sources in terms of Cartesian coordinates is written

$$\overset{add}{\Phi} = \frac{I\rho}{2\pi} ln\left(\sqrt{(x_p - x_s)^2 + (y_p - y_s)^2}\right) \tag{5.20}$$

where Φ_{add} is the additional potential function (Steward, 2015). The x component of the electric field arsing from a point source is written

$$\frac{\partial \overset{\text{add}}{\Phi}}{\partial x} = \overset{\text{add}}{E_x} = -\frac{I\rho}{2\pi}\left(\frac{x_p - x_s}{(x_p - x_s)^2 + (y_p - y_s)^2}\right) \tag{5.21}$$

and y component is written

$$\frac{\partial \overset{\text{add}}{\Phi}}{\partial y} = \overset{\text{add}}{E_y} = -\frac{I\rho}{2\pi}\left(\frac{y_p - y_s}{(x_p - x_s)^2 + (y_p - y_s)^2}\right) \tag{5.22}$$

where $\overset{\text{add}}{E_y}$ and $\overset{\text{add}}{E_y}$ are the additional E-field functions.

5.3.3 Separation of Variables Solution of Laplace's Equation

A solution to the 2D Laplace Equation can be represented by a seperation of variables solution in rectangular coordinates (Steward and Allen, 2013). The general form the 2D Laplace's equation is given

$$\frac{\partial^2 \Phi}{\partial x^2} + \frac{\partial^2 \Phi}{\partial y^2} = 0. \tag{5.23}$$

The potential function Φ is represented in a separated form as

$$\Phi = X(x)Y(y) \tag{5.24}$$

where X is a function that only varies with x and Y is a function that only varies with y, where in this case $x_{min} < x < x_{max}$ and $y_{min} < y < y_{max}$ as shown in Figure 5.1. Combining this equation with the latter gives the following expression (Moon and Spencer, 1961).

$$Y\frac{d^2X}{dx^2} + X\frac{d^2Y}{dy^2} = 0 \tag{5.25}$$

Note that the ∂ symbol is not used as X and Y are univariate functions. Rearranging this equation gives,

$$\frac{X''}{X} = -\frac{Y''}{Y} = p \tag{5.26}$$

where p is the separation constant. Finally, this gives two ordinary differential equations.

$$
\begin{aligned}
X'' &= pX \\
Y'' &= -pY
\end{aligned}
\tag{5.27}
$$

The solutions to these equations are built from sin, cos, sinh, cosh functions, along with the separation constant p. The influence functions derived from these solutions over a rectangle is described in the next section.

5.3.4 Influence Functions

A solution to the Laplace equation over each rectangle can be obtained through the linear summation of influence functions. Influence functions allow for periodic, quadratic, linear, and constant variation along each side of a rectangle. The separation of variables solutions yields eight Fourier series terms that allow for the solution to vary periodically along each side of the rectangle. There are eight Fourier series terms that contribute the solution (Steward and Allen, 2013), each of which is given below,

$$
\begin{aligned}
\overset{1cos}{\Phi}_n &= \frac{\sinh 2\pi n \frac{x_{max}-x}{y_{max}-y_{min}}}{\sinh 2\pi n \frac{x_{max}-x_{min}}{y_{max}-y_{min}}} \cos 2\pi n \frac{y-y_{min}}{y_{max}-y_{min}} \\
\overset{1sin}{\Phi}_n &= \frac{\sinh 2\pi n \frac{x_{max}-x}{y_{max}-y_{min}}}{\sinh 2\pi n \frac{x_{max}-x_{min}}{y_{max}-y_{min}}} \sin 2\pi n \frac{y-y_{min}}{y_{max}-y_{min}} \\
\overset{2cos}{\Phi}_n &= \cos 2\pi n \frac{x-x_{min}}{x_{max}-x_{min}} \frac{\sinh 2\pi n \frac{y_{max}-y}{x_{max}-x_{min}}}{\sinh 2\pi n \frac{y_{max}-y_{min}}{x_{max}-x_{min}}} \\
\overset{2sin}{\Phi}_n &= \sin 2\pi n \frac{x-x_{min}}{x_{max}-x_{min}} \frac{\sinh 2\pi n \frac{y_{max}-y}{x_{max}-x_{min}}}{\sinh 2\pi n \frac{y_{max}-y_{min}}{x_{max}-x_{min}}} \\
\overset{3cos}{\Phi}_n &= \frac{\sinh 2\pi n \frac{x-x_{min}}{y_{max}-y_{min}}}{\sinh 2\pi n \frac{x_{max}-x_{min}}{y_{max}-y_{min}}} \cos 2\pi n \frac{y-y_{min}}{y_{max}-y_{min}} \qquad (5.28) \\
\overset{3sin}{\Phi}_n &= \frac{\sinh 2\pi n \frac{x-x_{min}}{y_{max}-y_{min}}}{\sinh 2\pi n \frac{x_{max}-x_{min}}{y_{max}-y_{min}}} \sin 2\pi n \frac{y-y_{min}}{y_{max}-y_{min}} \\
\overset{4cos}{\Phi}_n &= \cos 2\pi n \frac{x-x_{min}}{x_{max}-x_{min}} \frac{\sinh 2\pi n \frac{y-y_{min}}{x_{max}-x_{min}}}{\sinh 2\pi n \frac{y_{max}-y_{min}}{x_{max}-x_{min}}} \\
\overset{4sin}{\Phi}_n &= \sin 2\pi n \frac{x-x_{min}}{x_{max}-x_{min}} \frac{\sinh 2\pi n \frac{y-y_{min}}{x_{max}-x_{min}}}{\sinh 2\pi n \frac{y_{max}-y_{min}}{x_{max}-x_{min}}}
\end{aligned}
$$

where the numerical over-scripts (1,2,3,4) represent the side δ of the rectangle that each function is corresponds to, and each of the functions repeat n times over each side. Each of these terms is formulated to vary between +1 and -1 along each side. While the Fourier series is highly effective for matching different forms of functional variation, other types of influence functions may be added to the solution control the Gibb's phenomenon (Peterson, 1998; Steward, 2020a). Influence functions that allow for constant, linear, and quadratic variation of the potential and electric field along each side of a rectangle are written as (Steward and Allen, 2013) ,

$$\begin{aligned}
\overset{0}{\Phi} &= 1, \\
\overset{x}{\Phi} &= \tfrac{2x-(x_{max}+x_{min})}{x_{max}-x_{min}}, \\
\overset{y}{\Phi} &= \tfrac{2y-(y_{max}+y_{min})}{y_{max}-y_{min}}, \\
\overset{xy}{\Phi} &= \tfrac{2x-(x_{max}+x_{min})}{x_{max}-x_{min}} \tfrac{2y-(y_{max}+y_{min})}{y_{max}-y_{min}}, \\
\overset{x2y2}{\Phi} &= \left(\tfrac{2x-(x_{max}+x_{min})}{x_{max}-x_{min}}\right)^2 - \left(\tfrac{2y-(y_{max}+y_{min})}{x_{max}-x_{min}}\right)^2
\end{aligned} \tag{5.29}$$

Taking minus the gradient all terms in Eq. (5.28) and Eq. (5.29) gives influence functions for the x and y components of the electric field. The x components of the electric field given by the Fourier series terms are written:

$$
\begin{aligned}
\overset{\text{1cos}}{E}_{xn} &= +\frac{2\pi n}{y_{max}-y_{min}} \frac{\cosh 2\pi n \frac{x_{max}-x}{y_{max}-y_{min}}}{\sinh 2\pi n \frac{x_{max}-x_{min}}{y_{max}-y_{min}}} \cos 2\pi n \frac{y-y_{min}}{y_{max}-y_{min}} \\
\overset{\text{1sin}}{E}_{xn} &= +\frac{2\pi n}{y_{max}-y_{min}} \frac{\cosh 2\pi n \frac{x_{max}-x}{y_{max}-y_{min}}}{\sinh 2\pi n \frac{x_{max}-x_{min}}{y_{max}-y_{min}}} \sin 2\pi n \frac{y-y_{min}}{y_{max}-y_{min}} \\
\overset{\text{2cos}}{E}_{xn} &= +\frac{2\pi n}{x_{max}-x_{min}} \sin 2\pi n \frac{x-x_{min}}{x_{max}-x_{min}} \frac{\sinh 2\pi n \frac{y_{max}-y}{x_{max}-x_{min}}}{\sinh 2\pi n \frac{y_{max}-y_{min}}{x_{max}-x_{min}}} \\
\overset{\text{2sin}}{E}_{xn} &= -\frac{2\pi n}{x_{max}-x_{min}} \cos 2\pi n \frac{x-x_{min}}{x_{max}-x_{min}} \frac{\sinh 2\pi n \frac{y_{max}-y}{x_{max}-x_{min}}}{\sinh 2\pi n \frac{y_{max}-y_{min}}{x_{max}-x_{min}}} \\
\overset{\text{3cos}}{E}_{xn} &= -\frac{2\pi n}{y_{max}-y_{min}} \frac{\cosh 2\pi n \frac{x-x_{min}}{y_{max}-y_{min}}}{\sinh 2\pi n \frac{x_{max}-x_{min}}{y_{max}-y_{min}}} \cos 2\pi n \frac{y-y_{min}}{y_{max}-y_{min}} \\
\overset{\text{3sin}}{E}_{xn} &= -\frac{2\pi n}{y_{max}-y_{min}} \frac{\cosh 2\pi n \frac{x-x_{min}}{y_{max}-y_{min}}}{\sinh 2\pi n \frac{x_{max}-x_{min}}{y_{max}-y_{min}}} \sin 2\pi n \frac{y-y_{min}}{y_{max}-y_{min}} \\
\overset{\text{4cos}}{E}_{xn} &= +\frac{2\pi n}{x-x_{min}} \sin 2\pi n \frac{x_{max}-x_{min}}{x_{max}-x_{min}} \frac{\sinh 2\pi n \frac{y-y_{min}}{x_{max}-x_{min}}}{\sinh 2\pi n \frac{y_{max}-y_{min}}{x_{max}-x_{min}}} \\
\overset{\text{4sin}}{E}_{xn} &= -\frac{2\pi n}{x-x_{min}} \cos 2\pi n \frac{x_{max}-x_{min}}{x_{max}-x_{min}} \frac{\sinh 2\pi n \frac{y-y_{min}}{x_{min}-x_{min}}}{\sinh 2\pi n \frac{y_{max}-y_{min}}{x_{max}-x_{min}}}
\end{aligned}
\tag{5.30}
$$

and the y components of the electric field:

$$
\begin{aligned}
\overset{1\cos}{E}_{yn} &= +\frac{2\pi n}{y_{max}-y_{min}} \frac{\sinh 2\pi n \frac{x_{max}-x}{y_{max}-y_{min}}}{\sinh 2\pi n \frac{x_{max}-x_{min}}{y_{max}-y_{min}}} \sin 2\pi n \frac{y-y_{min}}{y_{max}-y_{min}} \\
\overset{1\sin}{E}_{yn} &= -\frac{2\pi n}{y_{max}-y_{min}} \frac{\sinh 2\pi n \frac{x_{max}-x}{y_{max}-y_{min}}}{\sinh 2\pi n \frac{x_{max}-x_{min}}{y_{max}-y_{min}}} \cos 2\pi n \frac{y-y_{min}}{y_{max}-y_{min}} \\
\overset{2\cos}{E}_{xy} &= +\frac{2\pi n}{x_{max}-x_{min}} \cos 2\pi n \frac{x-x_{min}}{x_{max}-x_{min}} \frac{\cosh 2\pi n \frac{y_{max}-y}{x_{max}-x_{min}}}{\sinh 2\pi n \frac{y_{max}-y_{min}}{x_{max}-x_{min}}} \\
\overset{2\sin}{E}_{yn} &= +\frac{2\pi n}{x_{max}-x_{min}} \sin 2\pi n \frac{x-x_{min}}{x_{max}-x_{min}} \frac{\cosh 2\pi n \frac{y_{max}-y}{x_{max}-x_{min}}}{\sinh 2\pi n \frac{y_{max}-y_{min}}{x_{max}-x_{min}}} \\
\overset{3\cos}{E}_{yn} &= +\frac{2\pi n}{y_{max}-y_{min}} \frac{\sinh 2\pi n \frac{x-x_{min}}{y_{max}-y_{min}}}{\sinh 2\pi n \frac{x_{max}-x_{min}}{y_{max}-y_{min}}} \sin 2\pi n \frac{y-y_{min}}{y_{max}-y_{min}} \\
\overset{3\sin}{E}_{yn} &= -\frac{2\pi n}{y_{max}-y_{min}} \frac{\sinh 2\pi n \frac{x-x_{min}}{y_{max}-y_{min}}}{\sinh 2\pi n \frac{x_{max}-x_{min}}{y_{max}-y_{min}}} \cos 2\pi n \frac{y-y_{min}}{y_{max}-y_{min}} \\
\overset{4\cos}{E}_{yn} &= -\frac{2\pi n}{x-x_{min}} \cos 2\pi n \frac{x_{max}-x_{min}}{x_{max}-x_{min}} \frac{\cosh 2\pi n \frac{y-y_{min}}{x_{max}-x_{min}}}{\sinh 2\pi n \frac{y_{max}-y_{min}}{x_{max}-x_{min}}} \\
\overset{4\sin}{E}_{yn} &= -\frac{2\pi n}{x-x_{min}} \sin 2\pi n \frac{x_{max}-x_{min}}{x_{max}-x_{min}} \frac{\cosh 2\pi n \frac{y-y_{min}}{x_{min}-x_{min}}}{\sinh 2\pi n \frac{y_{max}-y_{min}}{x_{max}-x_{min}}}
\end{aligned}
\tag{5.31}
$$

The constant, linear, quadratic influence functions for the x componenet of the electric field are:

$$
\begin{aligned}
\overset{0}{E}_x &= 0, \\
\overset{x}{E}_x &= \frac{2}{(x_{max}+x_{min})}, \\
\overset{y}{E}_x &= 0, \\
\overset{xy}{E}_x &= \frac{2}{(x_{max}+x_{min})} \frac{2y-(y_{max}+y_{min})}{y_{max}-y_{min}}, \\
\overset{x2y2}{E}_x &= -4\left(\frac{(2x-x_{max}+x_{min})}{x_{max}-x_{min}}\right)^2
\end{aligned}
\tag{5.32}
$$

and for the y component:

$$\begin{aligned} \overset{0}{E}_y &= 0, \\ \overset{x}{E}_y &= 0, \\ \overset{y}{E}_y &= \tfrac{2}{y_{max}-y_{min}}, \\ \overset{xy}{E}_y &= \tfrac{(2x-(x_{max}+x_{min})}{x_{max}-x_{min}} \tfrac{2}{y_{max}-y_{min}}, \\ \overset{x2y2}{E}_y &= 4\left(\tfrac{(2y-y_{max}+y_{min})}{x_{max}-x_{min}}\right)^2 \end{aligned} \tag{5.33}$$

Similar to the Fourier series terms, the linear and quadratic influence functions are also normalized by the length of the each rectangle side they are evaluated on to achieve variation between -1 and +1.

Now that the influence functions that form the solution have been introduced, the matrix formulation of the method will be shown. The electric potential and electric field is obtained for each rectangle by evaluating influence functions at control points and multiplying them by the rectangle coefficients. There are $8N + 5$ element coefficients for each rectangle, where N is the number of cycles for each Fourier series term along each side, δ. It is convenient to gather all coefficients in a column vector, as shown below.

$$c = \begin{bmatrix} \overset{0}{C} \\ \overset{x}{C} \\ \overset{y}{C} \\ \overset{xy}{C} \\ \overset{x2y2}{C} \\ \overset{\delta\cos}{C_n} \\ \overset{\delta\sin}{C_n} \end{bmatrix} \tag{5.34}$$

The potential over one rectangle is obtained through the summation of the rectangle coefficient times the influence functions in Eq. (5.28) and Eq. (5.29).

$$\Phi_0 = \overset{o}{c}\overset{o}{\Phi} + \overset{x}{c}\overset{x}{\Phi}(x) + \overset{y}{c}\overset{y}{\Phi}(y) + \overset{xy}{c}\overset{xy}{\Phi}(x,y) + \overset{x2y2}{c}\overset{x2y2}{\Phi}(x,y)$$
$$+[\Sigma_{n=1}^{N}\Sigma_{\delta=1}^{4}\overset{\delta cos}{c_n}\overset{\delta cos}{\Phi_n}(x,y) + \overset{\delta sin}{c_n}\overset{\delta sin}{\Phi_n}(x,y)] \tag{5.35}$$

Similarly, the electric field over a rectangle is obtained by summing the element coefficients times the influence functions in Eq. (5.29) - (5.33). The x component of the electric field for a rectangle is written

$$E_{x0} = \overset{o}{c}\overset{o}{E}_x + \overset{x}{c}\overset{x}{E}_x(x) + \overset{y}{c}\overset{y}{E}_x(y) + \overset{xy}{c}\overset{xy}{E}_x(x,y) + \overset{x2y2}{c}\overset{x2y2}{E}_x(x,y)$$
$$+[\Sigma_{n=1}^{N}\Sigma_{\delta=1}^{4}\overset{\delta cos}{c_n}\overset{\delta cos}{E}_{xn}(x,y) + \overset{\delta sin}{c_n}\overset{\delta sin}{E}_{xn}(x,y)] \tag{5.36}$$

and the y component of the electric field for rectangle is given by

$$E_{y0} = \overset{o}{c}\overset{o}{E}_y + \overset{x}{c}\overset{x}{E}_y(x) + \overset{y}{c}\overset{y}{E}_y(y) + \overset{xy}{c}\overset{xy}{E}_y(x,y) + \overset{x2y2}{c}\overset{x2y2}{E}_y(x,y)$$
$$+[\Sigma_{n=1}^{N}\Sigma_{\delta=1}^{4}\overset{\delta cos}{c_n}\overset{\delta cos}{E}_{yn}(x,y) + \overset{\delta sin}{c_n}\overset{\delta sin}{E}_{yn}(x,y)] \tag{5.37}$$

Additional forms of potential variation can be added to the solution over each rectangle (Steward, 2015). The potential variation arising from a point source must be added to the rectangle potential

$$\Phi = \Phi_0 + \overset{\text{add}}{\Phi}. \tag{5.38}$$

Similarly, the x componenet of the electric field arising from the point sources are added to the electric field over a rectangle

$$E_x = E_{x0} + \overset{\text{add}}{E}_x, \tag{5.39}$$

and the y component is added to the rectangle solution using

$$E_y = E_{y0} + \overset{\text{add}}{E}_y. \tag{5.40}$$

5.3.5 Computing Element Coefficients

Adjustment of the element coefficients allows the solution to meet the interface and boundary conditions. The previous section stepped through the solution assuming element coefficients were known. The matrix formulation to solve for unknown coefficients between two adjacent rectangles is described next. First, the influence functions for the electric potential are gathered into row vectors for all four sides of a rectangle

$$
\begin{aligned}
\mathrm{A1}&=\begin{bmatrix} \overset{0}{\Phi} & \overset{x}{\Phi} & \overset{y}{\Phi} & \overset{xy}{\Phi} & \overset{x2y2}{\Phi} & \overset{1\cos}{\Phi_n} & \overset{1\sin}{\Phi_n} \end{bmatrix},\\
\mathrm{A2}&=\begin{bmatrix} \overset{0}{\Phi} & \overset{x}{\Phi} & \overset{y}{\Phi} & \overset{xy}{\Phi} & \overset{x2y2}{\Phi} & \overset{2\cos}{\Phi_n} & \overset{2\sin}{\Phi_n} \end{bmatrix},\\
\mathrm{A3}&=\begin{bmatrix} \overset{0}{\Phi} & \overset{x}{\Phi} & \overset{y}{\Phi} & \overset{xy}{\Phi} & \overset{x2y2}{\Phi} & \overset{3\cos}{\Phi_n} & \overset{3\sin}{\Phi_n} \end{bmatrix},\\
\mathrm{A4}&=\begin{bmatrix} \overset{0}{\Phi} & \overset{x}{\Phi} & \overset{y}{\Phi} & \overset{xy}{\Phi} & \overset{x2y2}{\Phi} & \overset{4\cos}{\Phi_n} & \overset{4\sin}{\Phi_n} \end{bmatrix}.
\end{aligned}
\tag{5.41}
$$

Similarly, influence functions for the normal component of the electric field for all four sides of a rectangle can be gathered into row vectors

$$
\begin{aligned}
\text{Av1}=&\begin{bmatrix} \overset{0}{E_x} & \overset{x}{E_x} & \overset{y}{E_x} & \overset{xy}{E_x} & \overset{x2y2}{E_x} & \overset{\text{1cos}}{E_{xn}} & \overset{\text{1sin}}{E_{xn}} \end{bmatrix}, \\
\text{Av2}=&\begin{bmatrix} \overset{0}{E_y} & \overset{x}{E_y} & \overset{y}{E_y} & \overset{xy}{E_y} & \overset{x2y2}{E_y} & \overset{\text{2cos}}{E_{yn}} & \overset{\text{2sin}}{E_{yn}} \end{bmatrix}, \\
\text{Av3}=&\begin{bmatrix} \overset{0}{E_x} & \overset{x}{E_x} & \overset{y}{E_x} & \overset{xy}{E_x} & \overset{x2y2}{E_x} & \overset{\text{3cos}}{E_{xn}} & \overset{\text{3sin}}{E_{xn}} \end{bmatrix}, \\
\text{Av4}=&\begin{bmatrix} \overset{0}{E_y} & \overset{x}{E_y} & \overset{y}{E_y} & \overset{xy}{E_y} & \overset{x2y2}{E_y} & \overset{\text{4cos}}{E_{yn}} & \overset{\text{4sin}}{E_{yn}} \end{bmatrix}.
\end{aligned} \tag{5.42}
$$

The formulation to satisfy boundary and interface conditions in a least squares sense can be written generally as

$$Ac = b \tag{5.43}$$

where A is the matrix of influence functions for each side of a rectangle (either Dirichlet or Nuemann), b is the matrix of boundary conditions (Dirichlet or Nuemann), and c is the coefficient matrix for the rectangle or rectangles. An iterative approach is used to adjust the coefficients in Eq.(5.34) to satisfy boundary and interface conditions between to adjacent interconnected rectangles in a least squares sense. The values of the normal component of the electric field at control points used for the Nuemann boundary conditions for rectangle side 1 are

$$\overset{E_N}{\text{b1}} = E_x(x_m^1, y_m^1) \tag{5.44}$$

and for side 2,

$$\overset{E_N}{\text{b2}} = E_y(x_m^2, y_m^2) \tag{5.45}$$

and for side 3,

$$\overset{E_N}{\text{b3}} = E_x(x_m^3, y_m^3) \tag{5.46}$$

and for side 4,

$$\overset{E_N}{\text{b4}} = E_y(x_m^4, y_m^4) \tag{5.47}$$

where $E_x(x_m, y_m)$ and $E_y(x_m, y_m)$ are the specified values of the normal componenet of the electric field at the control points. Dirichlet conditions in which the value of the potential is specified at control points are written

$$\overset{\Phi}{\text{b1}} = \Phi(x_m^1, y_m^1) \tag{5.48}$$

and for side 2,

$$\overset{\Phi}{\text{b2}} = \Phi(x_m^2, y_m^2) \tag{5.49}$$

and for side 3,

$$\overset{\Phi}{\text{b3}} = \Phi(x_m^3, y_m^3) \tag{5.50}$$

and for side 4,

$$\overset{\Phi}{\text{b4}} = \Phi(x_m^4, y_m^4). \tag{5.51}$$

The matrix setup for computation of the element coefficients for the rectangle pairs shown in Figure 5.2A with Nuemann boundary conditions and continuity of potential across the rectangle interface is written (Steward, 2020a)

$$\begin{bmatrix} \text{Av1} & 0 \\ \text{Av2} & 0 \\ \text{Av4} & 0 \\ \text{A3} & A1 \\ \sigma^-\text{Av3} & \sigma^+\text{Av1} \\ 0 & \text{Av2} \\ 0 & \text{Av3} \\ 0 & \text{Av4} \end{bmatrix} \begin{bmatrix} c^- \\ c^+ \end{bmatrix} = \begin{bmatrix} \overset{E_N}{\text{b1}} - \overset{\text{add}}{E_x}(x_m^1, y_m^1) \\ \overset{E_N}{\text{b2}} - \overset{\text{add}}{E_y}(2_m^2, y_m^2) \\ \overset{E_N}{\text{b4}} + \overset{\text{add}}{E_x}(x_m^4, y_m^4) \\ \overset{\text{add}}{\Phi}(x_m^3, y_m^3) - \overset{\text{add}}{\Phi}(x_m^1, y_m^1) \\ \sigma^-\overset{\text{add}}{E_x}(x_m^3, y_m^3) - \sigma^+\overset{\text{add}}{E_x}(x_m^1, y_m^1) \\ \overset{E_N}{\text{b2}} - \overset{\text{add}}{E_y}(x_m^2, y_m^2) \\ \overset{E_N}{\text{b3}} + \overset{\text{add}}{E_x}(x_m^3, y_m^3) \\ \overset{E_N}{\text{b4}} + \overset{\text{add}}{E_y}(x_m^4, y_m^4) \end{bmatrix} \tag{5.52}$$

where c^- and c^+ are the coefficients rectangles on the left and right side of the interface, and σ^- and

σ^+ is the electrical conductivity of the rectangle to the left and right of the vertical interface. The fourth row of the A and b matrices correspond to the continuity of potential across the adjoining interface, and the fifth row of the A and b matrices correspond to the jump in the normal component of the electric field. The interface conditions for the electric field across the interface is satisfied when the following expression is equal to 0

$$\sigma^- E_x(x_m^3, y_m^3, c^-) - \sigma^- E_x(x_m^1, y_m^1, c^+) = 0. \tag{5.53}$$

The continuity of potential across the interface is also satisfied when the following expression is equal to 0

$$\sigma^- \Phi(x_m^3, y_m^3, c^-) - \sigma^- \Phi(x_m^1, y_m^1, c^+) = 0. \tag{5.54}$$

The formulation for solving boundary and interface conditions between a pair of rectangles separated by a horizontal interface is written (Steward, 2020a)

$$\begin{bmatrix} \text{Av1} & 0 \\ \text{Av2} & 0 \\ \text{Av3} & 0 \\ \text{A4} & A2 \\ \sigma^-\text{Av4} & \sigma^+\text{Av2} \\ 0 & \text{Av1} \\ 0 & \text{Av3} \\ 0 & \text{Av4} \end{bmatrix} \begin{bmatrix} c^- \\ c^+ \end{bmatrix} = \begin{bmatrix} \overset{E_N}{\text{b1}} - \overset{\text{add}}{E_x}(x_m^1, y_m^1) \\ \overset{E_N}{\text{b2}} - \overset{\text{add}}{E_y}(2_m^2, y_m^2) \\ \overset{E_N}{\text{b3}} + \overset{\text{add}}{E_x}(x_m^3, y_m^3) \\ \overset{\text{add}}{\Phi}(x_m^4, y_m^4) - \overset{\text{add}}{\Phi}(x_m^2, y_m^2) \\ \sigma^- \overset{\text{add}}{E_x}(x_m^4, y_m^4) - \sigma^+ \overset{\text{add}}{E_x}(x_m^2, y_m^2) \\ \overset{E_N}{\text{b1}} - \overset{\text{add}}{E_y}(x_m^1, y_m^1) \\ \overset{E_N}{\text{b3}} + \overset{\text{add}}{E_x}(x_m^3, y_m^3) \\ \overset{E_N}{\text{b4}} + \overset{\text{add}}{E_y}(x_m^4, y_m^4) \end{bmatrix}. \tag{5.55}$$

The interface conditions for the electric field across the interface is satisfied when the following expression is equal to 0

$$\sigma^- E_x(x_m^4, y_m^4, c^-) - \sigma^- E_x(x_m^2, y_m^2, c^+) = 0. \tag{5.56}$$

Likewise, the continuity of potential across the interface is also satisfied when the following expression is equal to 0

$$\sigma^{-}\Phi(x_m^4, y_m^4, c^-) - \sigma^{-}\Phi(x_m^2, y_m^2, c^+) = 0. \tag{5.57}$$

The formulation of the forward problem with the AEM using the above equations allows for high computational accuracy near point sources and discontinuities without refining the computational grid. The superposition of the analytic solutions provides a robust and flexible mathematical method to accurately solve for the electric field and electric potential distributions not only within deeper regions of the model, but near the surface of the model where model predictions are compared to field observations. The results of forward simulations using the presented formulations is given in Chapter 7.

5.4 Particle Swarm Optimization

Particle Swarm Optimization (PSO) was developed by Eberhart and Kennedy (1995), and is closely related to evolutionary strategies and genetic algorithms. PSO mimics the behavior flocking birds in search for food as particles fly through a parameter space in search for an optimal solution. Each particle within a swarm can be thought of as a potential solution (set of parameters) to the optimization problem. The term "position" is used to represent the values of the parameters each particle is trying to optimize. A "velocity" term represents how far and in which direction each of the parameter values change between iterations. The inertia weight model, developed by Shi and Eberhart (1998), is one of the more widely used forms of the PSO scheme. The inertia weight, w, controls the global and local search ability of the swarm. Initially, the inertia weight is set to a value near 0.9 to allow for the particles to exploit the entire parameter space (global search behavior). The inertia weight w is linearly decreased (damped) through the iterative search to a value of 0.4 to enable more localized searching to occur for improved convergence (Shi and Eberhart, 1998). Each particle's velocity vector is computed according to Eq. (5.58)

$$v_{k+1}^i = \omega_k v_k^i + c_1 r_1 (p_k^i - x_k^i) + c_2 r_2 (p_k^g - x_k^i) \tag{5.58}$$

where ω_k is the inertia weight factor and the current iteration, p_k^i is the best position (in terms of data misfit) of the individual particle though k iterations (personal best), p_k^g is the position of the best particle in the entire swarm as of iteration k (or global best position), c_1 and c_2 are cognitive and social weighting parameters that provide each particle with some sense of trust in their personal fitness (c_1) and the swarm's historical fitness (c_2), and r_1 and r_2 are random numbers generated from a uniform distribution ranging between 0 and 1 that adds a stochastic element to the search scheme. Eq. (5.59) defines how each particle's position is updated at each iteration,

$$x_{k+1}^i = x_k^i + v_{k+1}^i \tag{5.59}$$

where k is the iteration number, i is the particle index, v is the velocity of the particle, and x is the position of the particle.

One of the main problems regarding PSO is how to deal with particles that leave a bounded parameter space during the search procedure (Kaur and Kaur, 2015). Potential solutions that originate from outside of the parameter space bounds are infeasible, and provide no information about the global solution. Possible boundary restriction mechanisms include the following:

1. Velocity Re-initialization-Particle velocity values are reinitialized to zero;
2. Velocity Clamping - Maximum velocity constraint is placed upon the particles;
3. Velocity Adaption - Velocity of particles is up-scaled or down-scaled by a predetermined factor depending upon it's proximity to the most current global solution;
4. Position Re-initialization - Position of particles outside of the parameter space are reset to the confines of the search space.

A maximum velocity of 10% of the maximum parameter space dimension was used for all simulations in this research. Additionally, a velocity adaption and re-positioning techniques were employed. These techniques ensured that particles who left the parameter space were re-positioned to the nearest parameter space boundary and that their current velocity was multiplied by -1 to redirect the particle towards the interior of the feasible region.

Ensuring uniform coverage of the parameter space is vital to exploit the global solution within a highly complex parameter space. A Halton sequence was used to initialize the position of each particle within the parameter space. Other types of quasi-random sequences commonly used in global optimization are the Sobol sequence and the Van der Corupt sequence (Bratley and Fox, 1988). The advantage of using a quasi-random or low discrepancy number sequences over pseudo-random number sequences is the enhanced coverage of the parameter space they provide (Pant et al., 2008). The difference in the coverage of a 2 dimensional parameter space is illustrated in Figure 5.3, which compares 1,000 samples generated using a quasi-random sequence and pseudo-random sequence.

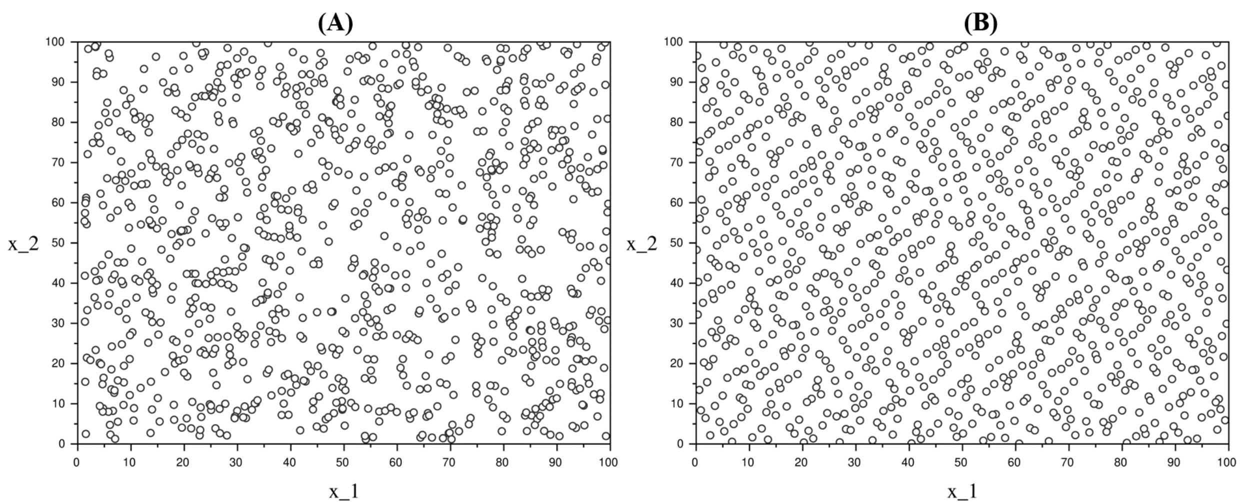

Figure 5.3: Scatter plots showing 1,000 samples in two dimensions for a pseudo-random number sequence drawn from a uniform distribution (A), and 1,000 samples drawn from a quasi-random number sequence (Halton sequence). Both dimensions range between 0 to 100.

A quasi-random sequence increases the chance that an initial particle is closer to the actual solution by more uniformly sampling the parameter space (Pant et al., 2008). Other quasi-random sequences used for initialization are the Sobol sequence (e.g., Lamsal et al. (2016)), which has been shown to improve the performance of global optimization (Bratley and Fox, 1988).

The generalized flowchart of the PSO procedures Figure 5.4 gives the sequential progression algorithm. Using PSO in the context of DC resistivity inversion removes the need for a good initial model for a global solution to be achieved. Additionally, PSO allows for optimal and suboptimal

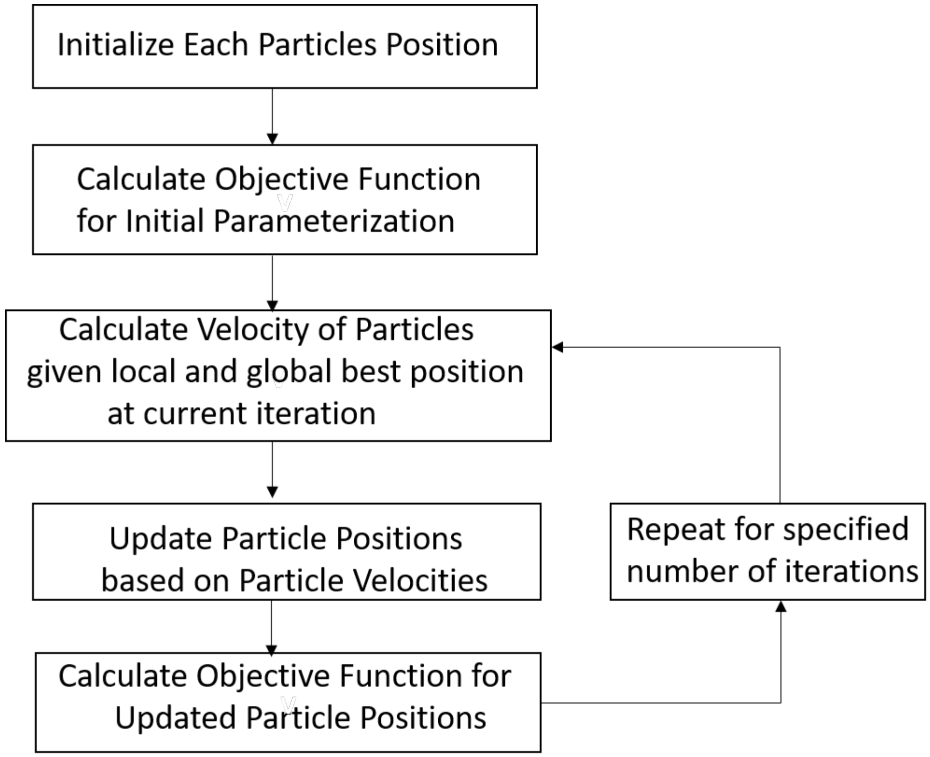

Figure 5.4: Flow chart of the Particle Swarm Optimization Procedure

solutions (in terms of misfit) to be compared, which allows the user to understand what class of model best fits the data if some a-priori information is available. Simulation results from this PSO scheme are shown in Chapter 7.

Chapter 6

Results: Analysis of Electrostatic Fields across Soil Interfaces with the AEM

The focus of this chapter is to demonstrate the ability of the Analytic Element method to solve for electric potential distribution within a variety of hydrogeologic scenarios. The methods described in Chapter 5 provided the necessary background the understand how the AEM and PSO approaches are applied in regards to electrostatic fields and optimization. The results in the next two chapters will serve as the initial findings of these methods to bridge the gap between ERT methods and the AEM. In light of the understanding provided by the ERT surveys shown Chapter 3, the results from the AEM scheme are presented by this new computational method to form hydrogeologic interpretations of ERT data.

Subsurface domains are represented using a series of interconnected rectangular elements with different electrical properties. An electric field is produced by applying an electrical charge (equal to the magnitude of electric current multiplied by the resistivity surrounding the source) through two surface based point sources. All models in this section have an established potential difference of 100 Volts between the point sources (0.25 m below surface) to allow for an equal comparison of each scenario. This was done by running through an iterative root finding scheme to find the appropriate current magnitude for each source pair given the resistivity distribution of the model. Nuemann boundary conditions were satisfied to within three significant digits for all model runs.

Spacing of equipotential lines differs for some scenarios to better illustrate the important features of the solution across different levels of electrical contrast. The ability for the AEM to accurately match boundary and interface/continuity conditions across sharp geologic interfaces will be discussed in detail.

The electric potential and electric field distribution within a layered geologic system is shown in Figure 6.1A. There are horizontal divisions within the domain, however, the electrical properties do not change in the horizontal direction. The continuity of electric potential and jump in the normal component of the electric field across a horizontal interface is shown by Figure 6.1B. The electrical resistivity is 100 Ω m above the interface and 15 Ω m below the interface. This resistivity distribution is representative of an unsaturated vadose zone (dry sand) overlying an unconfined-unconsolidated aquifer system, similar to the surveys conducted in Chapter 3 and shown in Figure 3.6.

Another layered system is illustrated in Figure 6.2A, where two lowly resistive layers (15 Ω m) surround a moderately resistive layer (100 Ω m) and overly 12 m of material with a resistivity of 50 Ω m. This scenario could be represented by a geologic scenario in which the surface is predominately fined grained material that overlies alternating layers of shale and limestone. Shales and limestone can exhibit electrical anisotropy (Keller and Frischknecht, 1966). This occurs when the electrical response is dependent upon the orientation of the electric field, meaning that the resistivity values of the materials are directionally dependent. However, this scenario assumes that thy are both isotropic materials.

The model domain in Figure 6.3 contains a highly resistive inclusion (ρ = 15,000 Ω m), which is located between 26 m and 29 m between the depths of -12 m to -24 m. This inclusion is surrounded by a homogeneous background with a resistivity of 15 Ω m. The inclusion is essentially completely insulated from the electric field as the equipotential lines meet its vertical boundaries at right angles. Producing an accurate solution across this level of electrical contrast (three orders of magnitude) shows the ability of the method to be used for forward modelling of surveys aimed at detecting slender resistive bodies. Arjwech et al. (2013) analyzed the ability of standard ERT methods to identify the depth of concrete bridge foundations, and found that only the upper portions of narrow resistive bodies were distinguishable due to the resolution of the specific array type

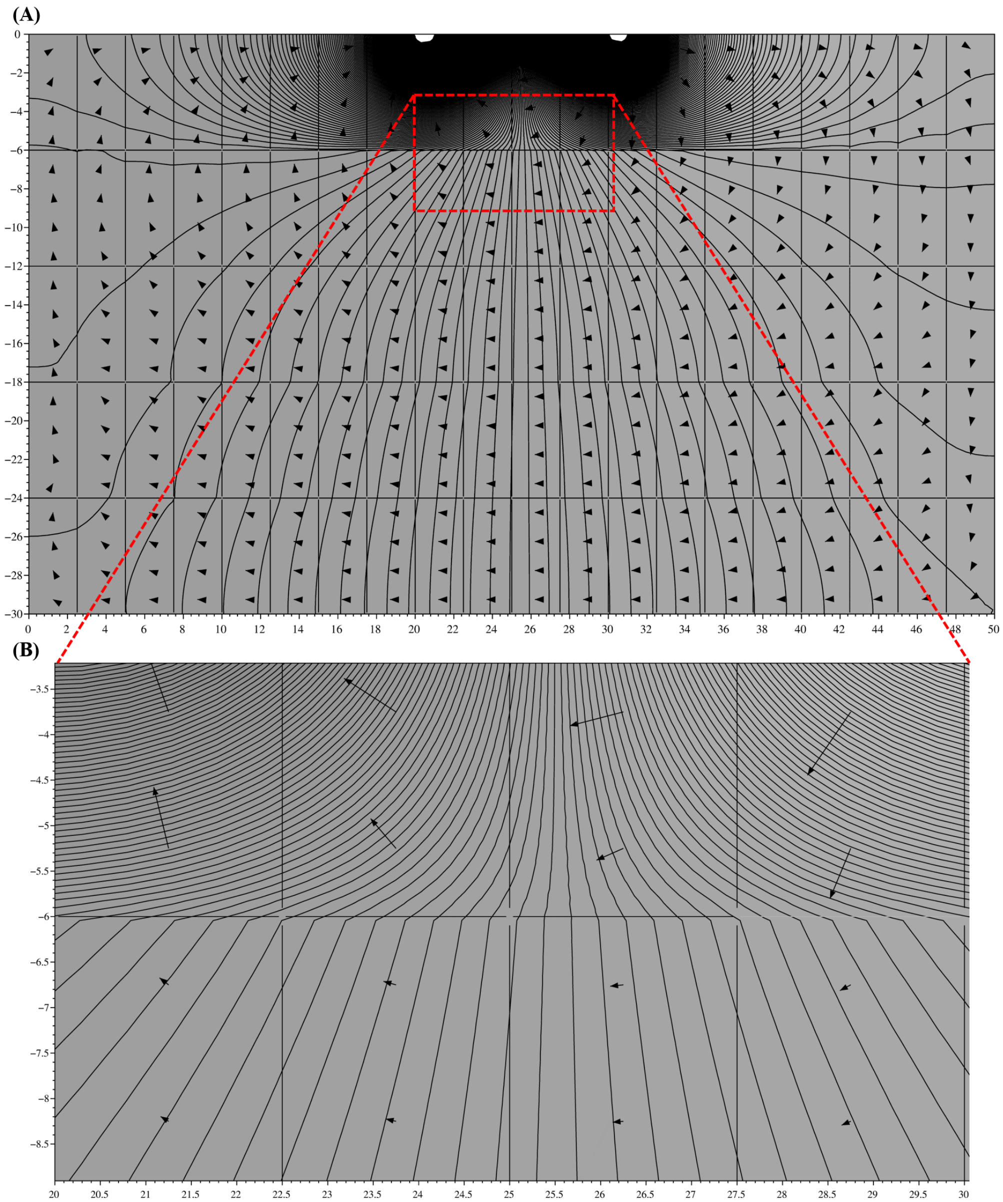

Figure 6.1: A set of 100 interconnected rectangles representing five uniformly thick geologic layers (0 m to 6 m - 100 Ω m; 6 m to 12 m - 15 Ω m; 12 m to 18 m - 15 Ω m; 18 m to 24 m - 50 Ω m; 24 m to 30 m - 50 Ω m). The interval between equipotential lines 0.25 volts.

used in the survey. Although 15,000 Ω m is above the range of resistivity values that concrete normally exhibits (i.e., (500 Ω m to 5,000 Ω depending on the current frequency (Layssi et al., 2015)), this scenario demonstrates the numerical ability of the AEM to match continuity conditions across interfaces separating highly conductive and highly resistive bodies. While the lack of resolution is related to survey design, the ability to accurately deduce the impact of specific subsurface targets

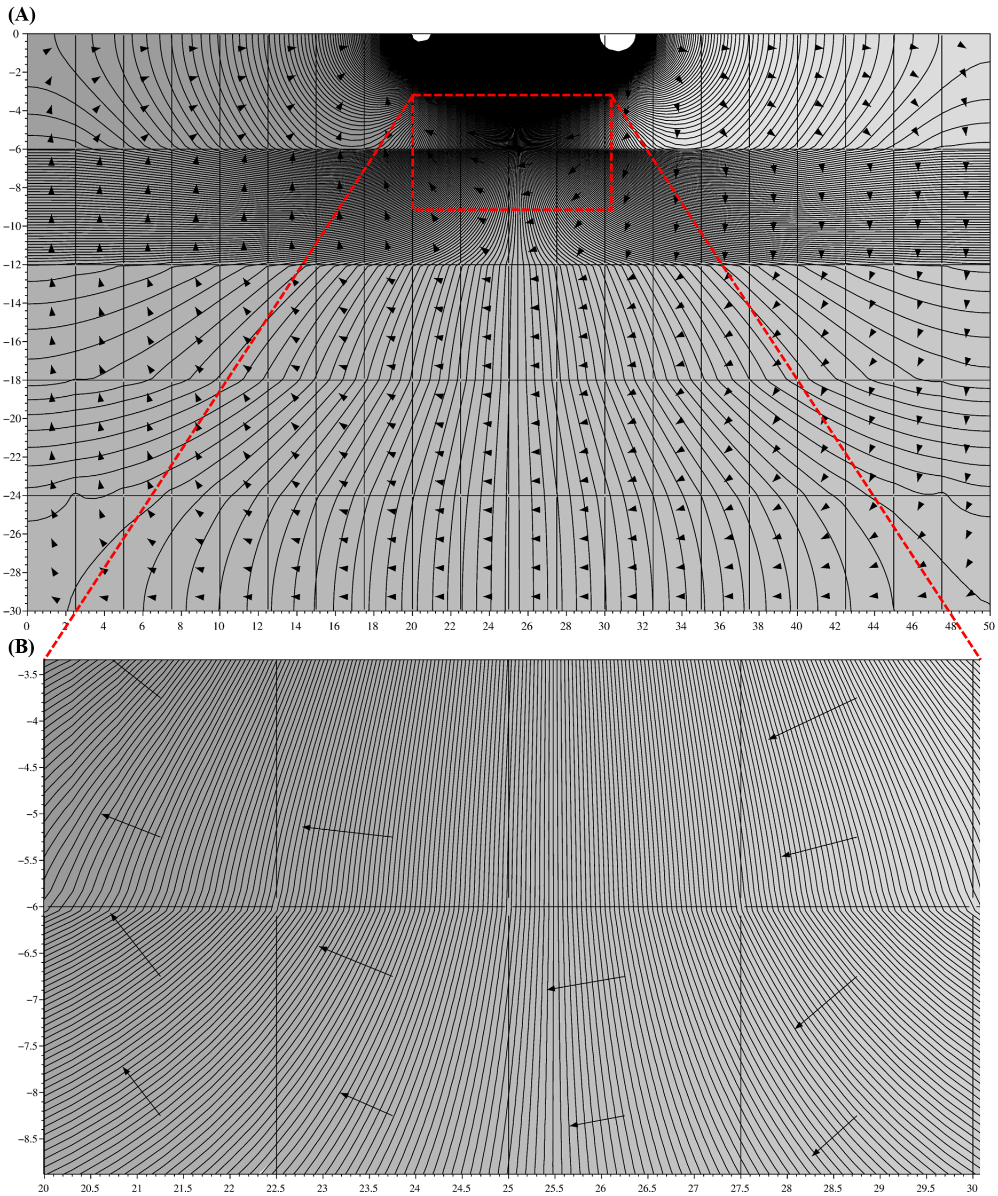

Figure 6.2: A set of 100 interconnected rectangles representing five uniformly thick geologic layers (0 m to 6 m - 15 Ω m; 6 m to 12 m - 100 Ω m; 12 m to 18 m - 15 Ω m; 18 m to 24 m - 50 Ω m; 24 m to 30 m - 50 Ω m). The interval between equipotential lines is 0.25 volts.

on the surface response is extremely useful in survey design. A sensitivity analysis of resistive perturbations could be carried out using similar geometries shown in Figure 6.3 to find the optimal electrode array for such studies.

The model domain shown in Figure 6.4A contains lowly resistive vertical strip (ρ=1 Ω m) stretching from the top to the bottom of the model domain between 21 m and 29 m. The surrounding background is homogeneous and represents a more resistive material (ρ=15 Ω m). The

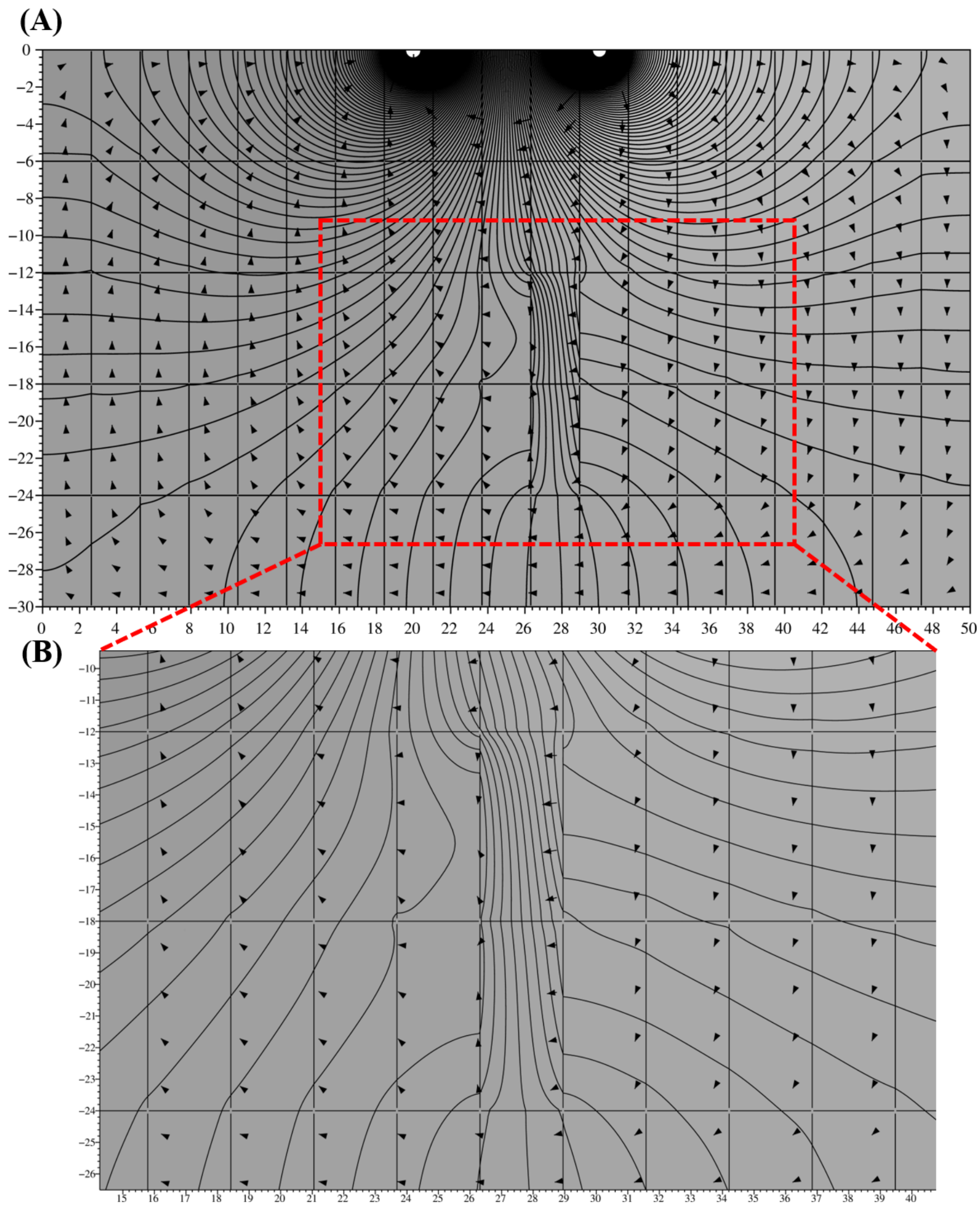

Figure 6.3: Highly resistive inclusion (15,000 Ω m) within a homogeneous background (15 Ω m). The interval between equipotential lines is 0.5 volts.

resistivity distribution of this model scenario is representative of a field setting in which an ERT survey is conducted across a recharge zone, where saturated and unsaturated regions of soil exhibit sharp contrasts in electrical properties across small spatial scales (See Chapter 3 for ERT surveys conducted within similar environments). A close up view of the model between point sources (Figure 6.4B shows the large potential gradients that occur near the sources, and the sharp discontinuity in the normal component of the electric field.

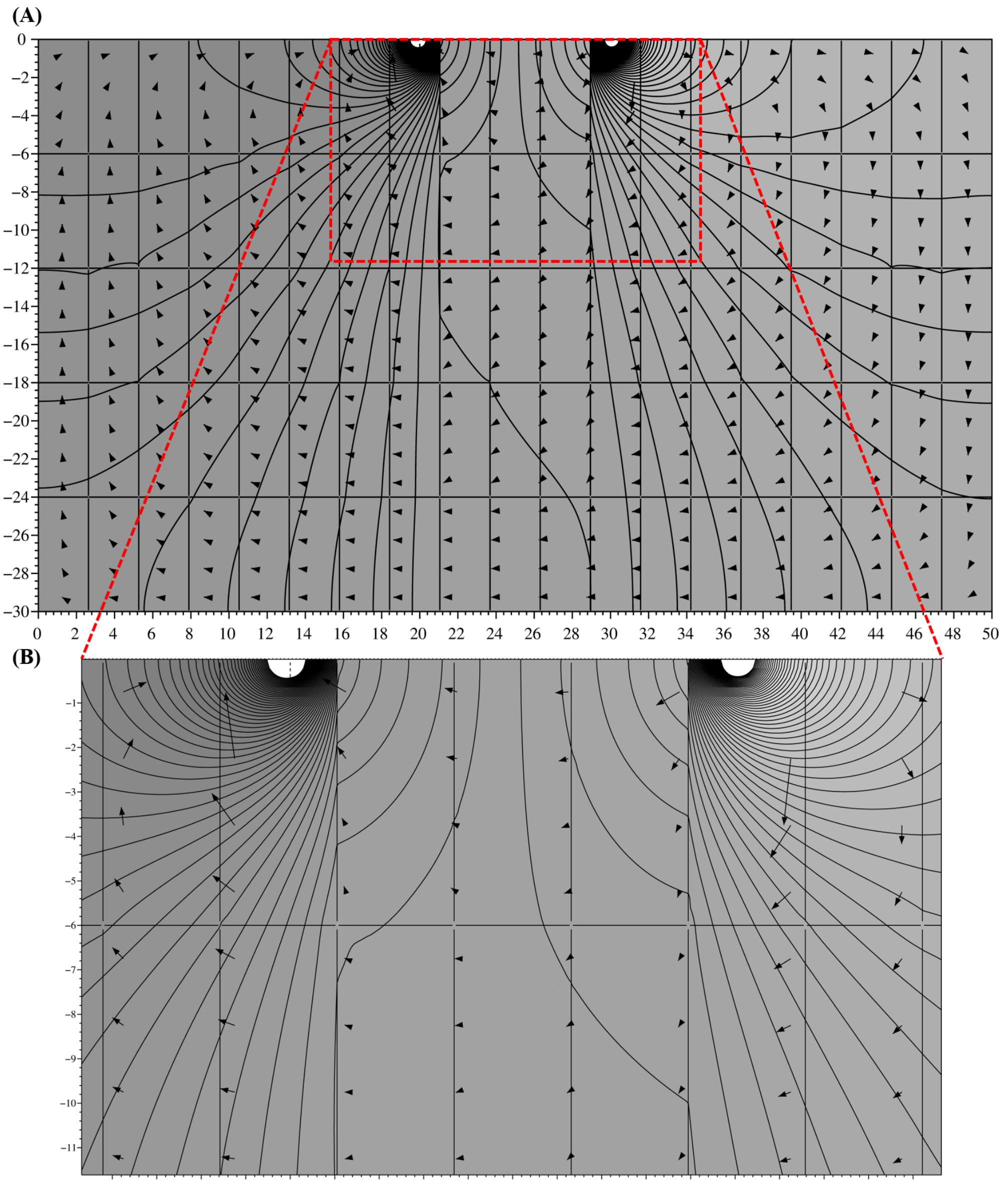

Figure 6.4: Lowly resistive vertical inclusion (1 Ω m) bounded by a homogeneous background (15 Ω m). The interval between equipotential lines is 1.0 volts.

The model accurately matches the interface and boundary conditions across the discontinuity. The ability of the model to converge when a discontinuity is placed directly adjacent to a source is one of the advantages the AEM has over of a discretized computational method. The steep gradients around the source require a discretized method to locally refine their mesh to achieve an accurate solution (Günther and Rücker, 2015). The ability to reduce the complexity of the domain near point sources lessens the number of model parameters that need to be determined by the inverse model. A finely discretized model near the surface may allow for large variations in electrical properties near voltage potential electrodes. This is one of the reasons that structural constraints (smooth variations in resistivity values) must be placed on highly discretized models. Smaller rectangular elements could be added to provide a more appropriate geologic representation if small features exist near points sources, however, it is not a requirement for the model to achieve an accurate solution.

An accuracy analysis of interface conditions was conducted along the horizontal interface shown in Figure 6.5A (solid red line). The interface separates two layers with a resistivity of 5 Ω m (top) and 75 Ω m (bottom). The error in the continuity of electric potential along the interface is shown by Figure 6.5B. The potential was calculated by evaluating Eq.(5.38) at the control points along the interface by using the top and bottom rectangle coefficients. Comparison of the normal and tangential components of the electric field across the interface are given in Figure 6.5C and D. The jump in the normal component across the interface varies periodically around a value of 15. This jump across the interface should be equal of the ratio between the electrical resistivity values of each rectangle (75/5=15) to perfectly match the interface conditions in (5.10). The continuity of tangential component of the electric field across the interface is verified in Figure 6.5D, as the difference on each side of the interface is less than 0.01 V/m for all control points. The periodic variation of these quantities originates from the seperation of variables solution (Fourier series solution). Adding more cycles N to the Fourier series terms would reduce the amplitude of the oscillations.

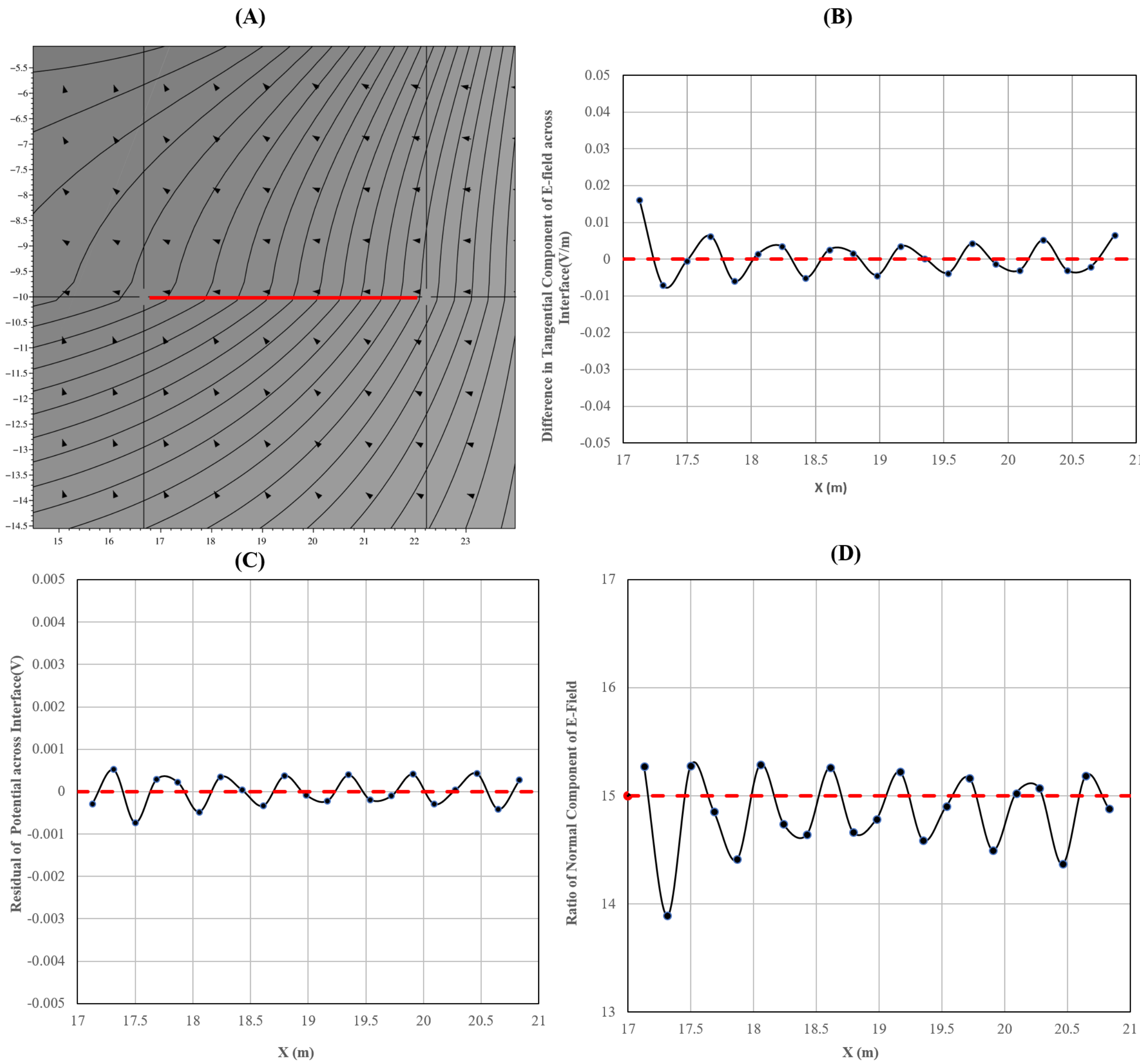

Figure 6.5: (A). Close up view of model where horizontal interface (red line) separates a moderately resistivie soil (75 Ω m above interface) and a lowly resistivie soil (5 Ω m below interface); (B). Difference in the tangential component of the electric field on each side of interface; (C). Difference in the normal component of the electric field on each side of the interface; (D). Ratio of the normal components of the electric field on each side of the interface

Chapter 7

Geophysical Inversion with a Particle Swarm Optimizer

A particle swarm optimization scheme was used to construct resistivity models for synthetic and field ERT datasets. The functionality of the PSO scheme was first validated using a dataset generated from a known resistivity model (1D layered model), and then tested with field data collected using 28 electrode ERT survey. The AEM model presented in Chapter 6 was used to create the synthetic dataset. The inertia weight model of PSO (Shi and Eberhart, 1998) was utilized for all model simulations. Table 5.1 gives the range of the parameter values used for all PSO simulations.

Table 7.1: PSO Parameter Values and Parameter Space Bounds

c1	c2	w	Swarm Population	Maximum Iterations	Min ρ (Ω m)	Max ρ (Ω m)
1.6	1.6	0.9-0.4	10-30	10-30	1	100

Note that the inertia weight w is linearly decreased from 0.9 to 0.4 between the beginning and end of the simulation to control the global and local search ability of the particles. The number of particles and number of maximum iterations significantly impact the convergence of the inertia weight model (Poli et al., 2007). Thus, different combinations of swarm populations and iteration numbers were included. The social, ($c1$), and cognitive, ($c2$), learning parameters and were both set to 1.6. They were set to equal values so that no preference was given to the social or cognitive influence. An in depth study on the optimal values for $c1$ and $c2$, as well as the swarm population and max number of iterations, should be conducted for this problem. The only widely accepted standard for the value of these parameters is that the sum of the two should be less than or equal to 4 to maintain stability (Poli et al., 2007). Ozcan and Mohan (1998) showed that the search pattern becomes unstable when the sum of $c1$ and $c2$ exceed 4, and that the particles exhibit more stable behavior when the sum of $c1$ and $c2$ is less than or equal to 4. Results are shown for simulations using swarm populations between 10 and 30 through 10 to 30 iterations. More iterations may improve the results of the simulations, however, they were limited to a maximum of 30 as simulations times became excessive for this problem given the computational framework that was employed. The use of multithreading for this scheme is very natural, and should be used in future studies to decrease simulation times.

7.0.1 Synthetic Data

A synthetic dataset was generated from a layered resistivity model to test the efficiency and ability of the PSO algorithm to reconstruct a 1D resistivity model. The scatter plot in Figure 7.1 provides an indication of the depth imaged by the survey based upon the median depth of investigation metric after Edwards (1977).

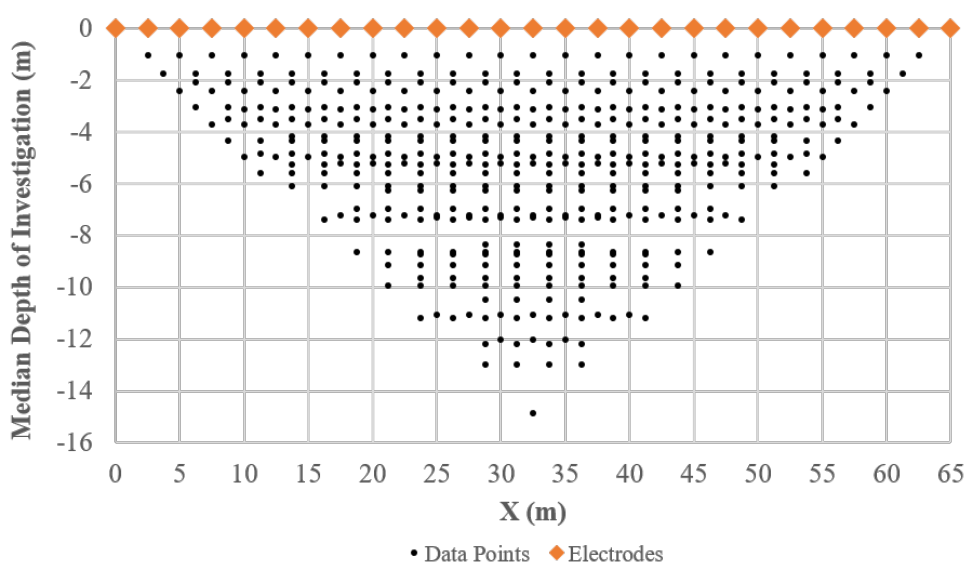

Figure 7.1: Pseudosection of the voltage/apparent resistivity measurements plotted at their median depth of investigation.

The dataset was generated over a five-layer 35 m deep resistivity model (Figure 7.3 using a 28 electrode dipole-dipole array). The dataset contains 450 data points (observed voltages) that were obtained from 116 different electrode configurations. Note that the maximum depth shown in Figure 7.1 is approximately 15 m. Under the assumption that the median depth represents the point in the earth that represents the median value of current density for each source electrode pair (Edwards, 1977), a model depth of 35 m was used (approximately twice of the maximum median depth for the entire array). The width of the model domain was set to 150 m. Oversizing the model domain relative to the survey length (65 m) helps to avoid effects from the exterior boundary conditions from influencing current propagation and perturbing the surface response. Two different PSO simulations were run to analyze how changes in the swarm population and number of iterations impacted the recovered model and convergence. A comparison of the measured and observed (synthetic) voltages for both simulations (A and B) is shown in Figure 7.2 along with the convergence plot of each simulation.

The error metrics for the simulations are shown in Table 7.2. Simulation A was run for 10 iterations using a swarm population of 30, and simulation B was executed for 30 iterations using a swarm population of 10. The RMSE (volts) was used as the objective function for both simulations. A comparison of the final model produced by each PSO simulation to the true model is shown in Figure 7.3. A sample of the simulations times for evaluating the objective function and conducting PSO simulations are shown in Table 7.3.

Table 7.2: Statistical comparison of model predictions to synthetic dataset

Simulation	RMSE (Volts)	MAE (Volts)	RMSPE (%)	RMSLE (Volts)
A	0.0224	0.010	6.046	0.0588
B	0.0218	0.011	6.522	0.0625

Both PSO simulations struggled to match the resistivity in the two deepest layers, as shown in Figure 7.3. This indicates that the two bottom layers should not be interpreted in the final model. This notion is also supported by the error metrics in Table 7.2. While the error metrics for both simulations are nearly identical, the recovered resistivity values within the bottom two layers are drastically different. Therefore, it is reasonable to say that the bottom two resistivity layers have little to no effect on the surface response produced by this particular ERT array. However, both

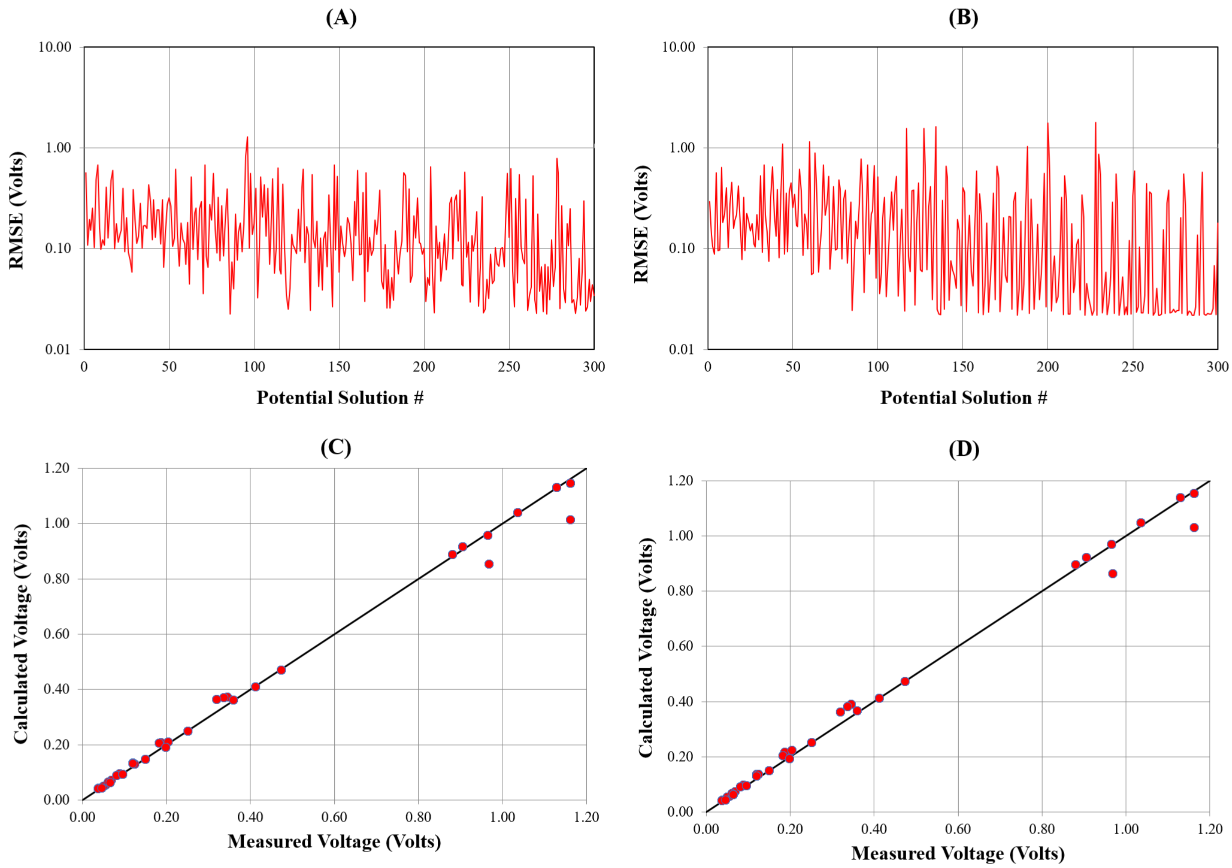

Figure 7.2: Comparison of convergence for two PSO simulations with different populations and maximum iterations (A and B), and scatter plots of voltage comparisons generated from final model solution (C and D).

Table 7.3: Computation times for the AEM forward solver and PSO simulations

Scenario	Time (seconds)	Time (hours)	Convergence (Volts)	N	M
A[1]	8,246	0.23	1e-3	3	15
B[1]	2,215	0.62	1e-3	5	15
C[1]	5,798	1.61	1e-3	10	30
D [2]	346,086	96.13	1e-3	3	15
E [3]	296,154	82.27	1e-3	3	15

[1]Objective function evaluated one time for one particle
[2]PSO simulation with a population of 10 for 30 iterations
[3]PSO simulation with a population of 30 for 20 iterations

models resemble the structure of the true models within the top three layers (0 m to 21 m), as the resistivity values are within 5 Ω m of the true values. This synthetic example shows the utility

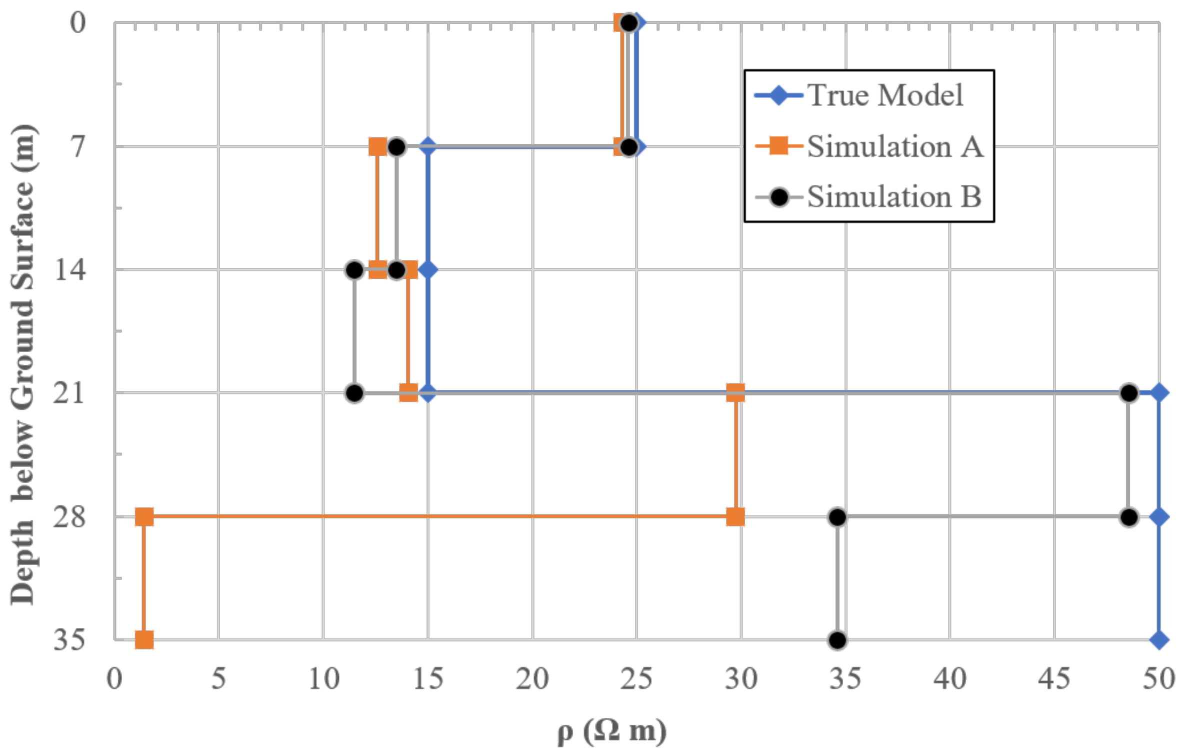

Figure 7.3: Comparison of resistivity models obtained from two PSO simulations with different swarm populations and maximum iterations.

of inverse modelling when designing surveys to target specific subsurface features. Attempting to image a structure below 21 m with this specific array would provide little to no information about the target.

7.0.2 Inversion of 28 Electrode ERT Survey

The PSO scheme was applied to a field dataset collected with a 28 electrode ERT survey conducted in the Konza Prairie near Manhattan, KS. The ERT dataset was collected using a 28 electrode dipole-dipole array with an electrode spacing of 2.5 m. This array is the identical to the array used to generate the synthetic data shown in the previous section. The field survey was conducted adjacent to a monitoring well which was used to determine the groundwater table elevation at the time of the survey (8 m below the land surface). The borehole lithologic log was also provided by the Kansas Geological Survey, which is shown in Table 7.4. The borehole log is overlaid onto the inverted (using the finite element software - EarthImager 2D) ERT survey in Figure 7.4. The survey was conducted in the lowland portion of King's creek watershed, which consists of approximately 10 m of fine grained alluvial deposits that overly alternating layers of shale and limestone (Steward et al., 2011).

Table 7.4: Borehole lithologic log adjacent to the ERT survey used for layered inversion.

Depth (m)	**Geologic Material**
0.0-0.3	Top Soil
0.3-9.1	Brown Clay
9.1-12.5	Large Gravel
12.5-13.7	Gray Shale
13.7-14.6	Limestone
14.6-15.2	Gray Oily Shale

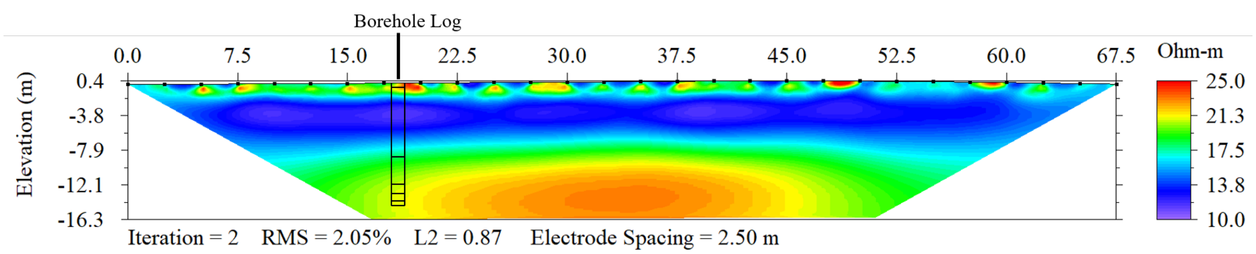

Figure 7.4: Inverted 28 electrode ERT survey with borehole log overlaid onto survey.

Four different PSO simulations were conducted with each minimizing a different objective function. This was done to gain insight on the performance of the scheme when different error metrics were used. The four different objective functions employed in the PSO scheme are given by Eq. (7.1) - Eq. (7.4).

$$RMSE = \sqrt{\frac{\Sigma_{i=1}^{N}(d_i^{calc} - d_i^{obs})^2}{N}} \tag{7.1}$$

and

$$MAE = \frac{\Sigma_{i=1}^{N}|(d_i^{calc} - d_i^{obs})|}{N} \tag{7.2}$$

$$RMSPE = \sqrt{\frac{\Sigma_{i=1}^{N}\left(\frac{d_i^{calc} - d_i^{obs}}{d_i^{obs}}\right)^2}{N}} * 100\% \tag{7.3}$$

$$RMSLE = \sqrt{\frac{\Sigma_{i=1}^{N}\left(log(\overset{calc}{d_i}) - log(\overset{obs}{d_i})\right)^2}{N}} \tag{7.4}$$

Each of the four PSO simulations was identical in form except for the objective function used. The four simulations each minimized one of the norms above for the same dataset. The 1D inversion case assumes the electrical resistivity only varies with depth (z direction), and is constant in the x direction. Thus, the resistivity of each layer can be thought of as the bulk average of all soil contained within a layer. The model consists of five 7 m thick rectangular domains. The cross plots in Figure 7.5 compare the observed and calculated voltage for the best model generated by each simulation. The statistical comparison of the model predictions are shown in Table 7.5. Each row in Table 7.5 reports four error metrics for one PSO simulation that used one of the four norms as the objective function. The convergence plots for simulation C and D are shown in Figure 7.6.

Table 7.5: Statistical comparison of model predictions to observed dataset from inversions minimizing four different misfit criteria

Minimized Norm	RMSE (Volts)	MAE (Volts)	RMSPE (%)	RMSLE (Volts)
RMSE	0.031	0.018	79.195	0.247
MAE	0.037	0.012	28.901	0.125
RMSPE	0.048	0.016	25.824	0.163
RMSLE	0.039	0.013	24.578	0.122

At first glance, there are some noticeable differences and similarities in each of the four scatter plots in Figure 7.5. There is an upper limit of calculated voltage for each of the four model scenarios, which makes sense given that a layered geometry was assumed. All calculated voltages that lie along a horizontal line were generated from the same electrode configurations. If a true layered system existed in nature, measurements conducted at the same electrode configuration would show no deviation in voltage difference in the absence of noise (similar to the synthetic data in the previous section). Regardless of the type of objective function used, the layered model geometry does not account for some lateral variation in electrical resistivity that was obviously present at the time of the survey. However, the RMSE produced a resistivity model whose response better approximated higher measured voltages. The other three objective functions produced models that

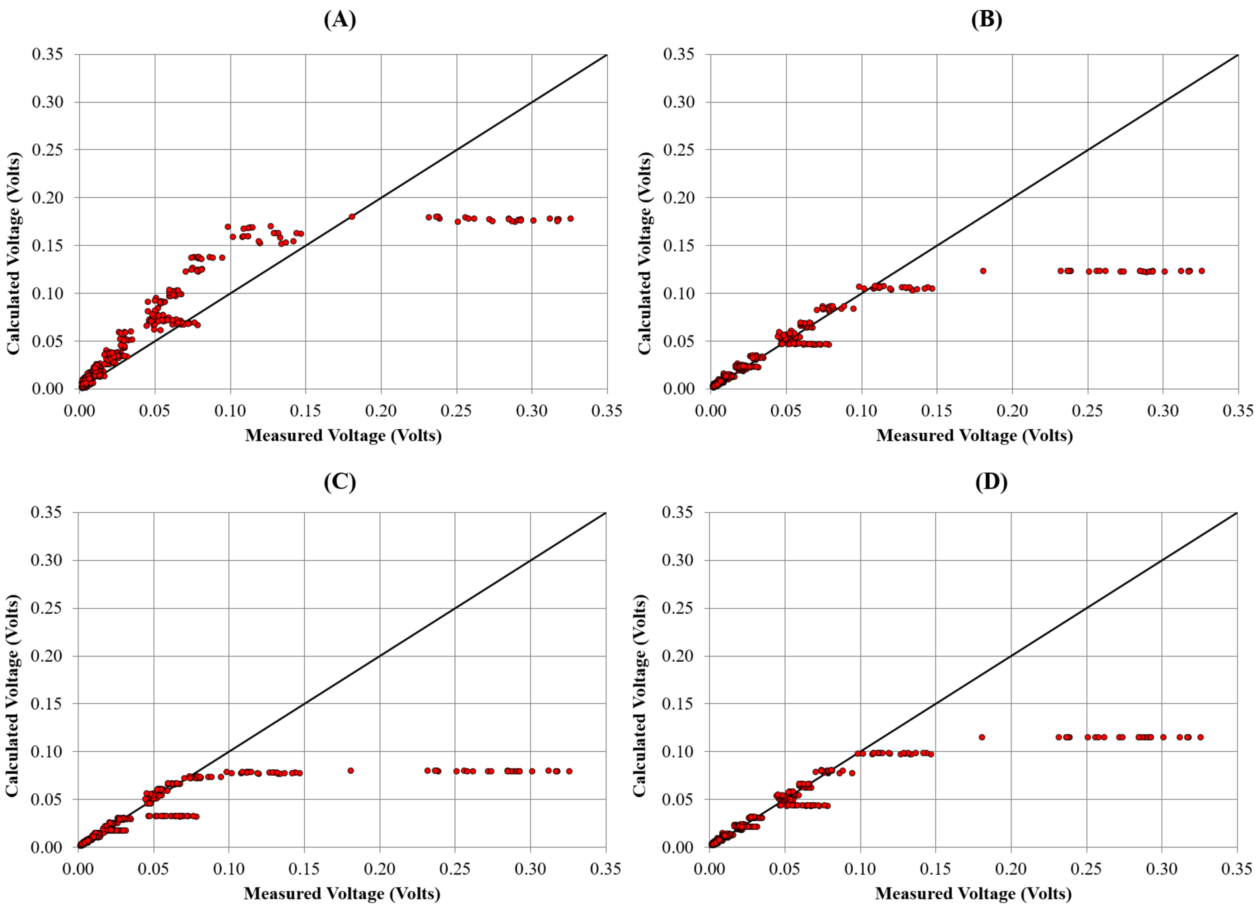

Figure 7.5: Cross-plots comparing the measured and calculated voltage difference for the Konza dataset. Results are from a layered inversion scenario in which four different objective functions were minimized; (A). RMSE; (B). MAE; (C). RMSPE; (D). RMSLE

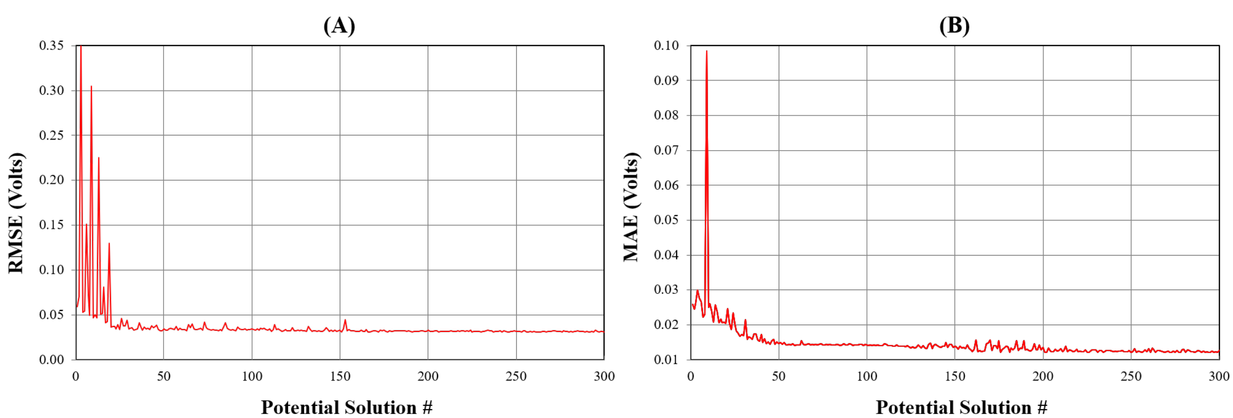

Figure 7.6: Convergence plot of simulation C (left) and simulation D (right). Simulation C used the RMSE as the objective function and simulation D used the MAE as the objective.

under predict observations above 0.1 V. Another reason for the deviation of these predictions from reality is the constraint placed upon the depth of the rectangles and number of rectangles. The scheme used to produce these predictions could easily be adapted to optimize for the depth and number of layers in conjunction to the resistivity of each rectangle to provide a more realistic representation of the resistivity distribution.

The major differences in how the objective functions impact the reconstruction of a resistivity model with this PSO scheme is apparent in Figure 7.7, which shows the final resistivity models as a function of depth. The simulation minimizing the RMSPE produced a relatively smoothly varying model with depth, while simulations the other three simulations produced models that exhibited larger jumps in the electrical resistivity. Based upon the results of the synthetic PSO test (Figure 7.3, only the top three layers of the model (0 m to -21 m) can be interpreted as this array type is insensitive at greater depths.

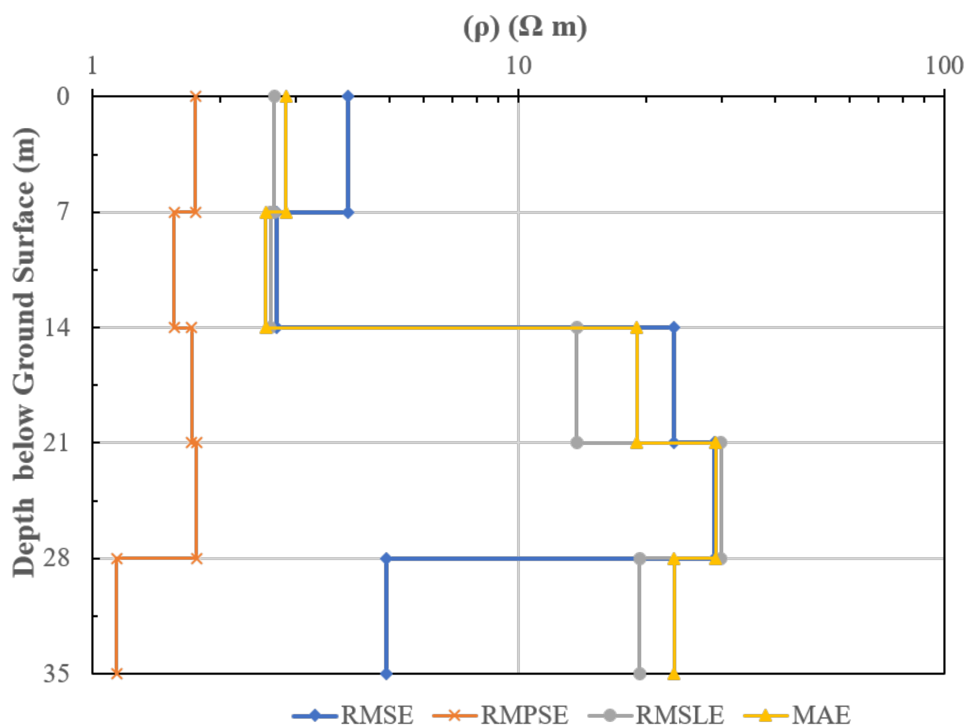

Figure 7.7: Depth log of resistivity for models generated using different objective functions

The known lithology log shown in Table 7.4 supports the geologic interpretation of the final models except for the RMPSE model. The resistivity obtained for the top two layers (0 m to

14 m) of the model indicate the presence of a lowly resistivie material, which corresponds to the established resistivity values of the materials in this region (clay-saturated gravel). Higher resistivity values were obtained for the bottom three layers, which is also supported by the known geology as a shale-limestone sequence is present (shale and limestone beds can exhibit resistivity values between (10 Ω m to 5,000 Ω m). The presence of a groundwater table at 8 m below the surface is corroborated by the lack of the resistivity contrast in the top two layers. Saturated coarse grained and fine grained materials can exhibit very similar electrical resistivity values (ERT surveys in Chapter 3).

The results of the 1D layered inversion scheme are highly dependent on the type of norm that is minimized. Although the layered assumption was obviously not true for this dataset, the AEM-PSO scheme still managed to distinguish the bulk changes in electrical resistivity in each of the top three layers expect for the RMPSE simulation. The use of the RMPSE metric for this dataset produced models that not only underestimated the resistivity of layers relative to the other norm simulations, but also produced little to no variation in the resistivity change with depth.

Chapter 8

Discussion

Determining an appropriate model depth is a vital componenet for reconstructing a physically realistic model. Gradient based inversion routines numerically solve for a sensitivity matrix at each iteration that is used to determine the depth at which a change in the model parameters most heavily influence the voltage distribution at the earth's surface for a specific electrode configuration. Local optimization schemes use this information to update the model parameters. This is a step not used in the PSO scheme as its search and updating procedure are not dependent of such information. Furman et al. (2002) calculated the optimal electrode configurations for specific arrays aimed at detecting circular heterogeneities using the AEM, however, they provided no information on how the depth of investigation is related to the optimal configurations. Edwards (1977) provided a concise explanation of the median depth of investigation as the depth at which half of the total signal (current) is above and below. When a change in the physical property at some depth is not detected by the surface response, this area is said to be not imaged by the array and features at this depth should not be interpreted or included in a final resistivity model.

The results in Chapter 6 show why determining the correct depth of investigation is important for interpreting a reconstructed resistivity model. An equally good fit was obtained for the two models derived from the synthetic data; however, the resistivity distributions at large depths were largely different and would provide a completely different interpretation of the earth. The use of the AEM-PSO scheme could be implemented to investigate how the depth of investigation for each array is manifested through reconstructed resistivity model across varying level of electrical contrast.

One of the simplifications of this model is the use of a 2D point source. While previous studies (Furman et al., 2002, 2004) used the AEM considering the 2D point source formulation given in Eq. (5.17) for determining the spatial sensitivity of different array types, there are implications of directly interpreting resistivity values derived from a two dimensional solution of a three dimensional phenomenon (current flow in earth).

A comparison of the analytical and numerical solution of the 2D voltage potential measured between potential electrodes at 1 to 8 electrode separations away from a point sink and point source spaced at 2.5 m is given in Table 8.1.

Solution	n	1	2	3	4	5	6	7	8
2D Analytical	Δ V (Volts)	4.579	1.875	1.027	0.650	0.448	0.328	0.251	0.198
2D Model	Δ V (Volts)	4.553	1.856	1.014	0.640	0.441	0.324	0.247	0.195
	% Error	0.55	0.98	1.30	1.51	1.55	1.38	1.35	1.24

Table 8.1: Comparison of analytical and model solution of voltage potentials caused by a 2D and 3D point source within a homogeneous halfspace with a resistivity of 100 Ω m.

The model is in good agreement with the 2D analytical solution for a homogeneous halfspace as the percent error is less than 2 for all measurements. Additionally, this verifies that the insulating boundary conditions (Nuemann conditions) implemented within the model do not impact the calculated voltage potentials. A scatter plot of the numerical and analytical solution of 2D voltage potentials, as well as the analytical solution of a 3D voltage potential (Eq. (5.18)) for the same homogeneous halfspace is illustrated Figure 8.1. The potential decay arising from a 3D point source varies as a function of $1/r$, while a 2D potential has a dependence of $ln(r)$. This means that an inversion scheme that simulates current flow using a 3D point source will deduce different electrical properties for the exact same voltage measurements than the same inverse scheme using a 2D point source formulation. To account for this, a quasi 2D solution (Modified Helmholtz Equation) should be explored so results from this computational method can be directly compared with standard simulation methods. The point source representation for the Modified Helmholtz equation is written

$$\Phi = \frac{I\rho}{2\pi} K_0(r) \tag{8.1}$$

where K_0 is the modified bessel function of second kind of zero order. This treatment is similar to that used by McGillivray (1992); Greenhalgh (2009). Not accounting for current flow in the third dimensions results in the inversion scheme employed in this study to underestimate resistivity values relative to established values. However, the mathematical derivation of influence functions for modified Helmholtz equation has been developed by Steward (2020a), and will be included in future work to make this inversion scheme fully applicable.

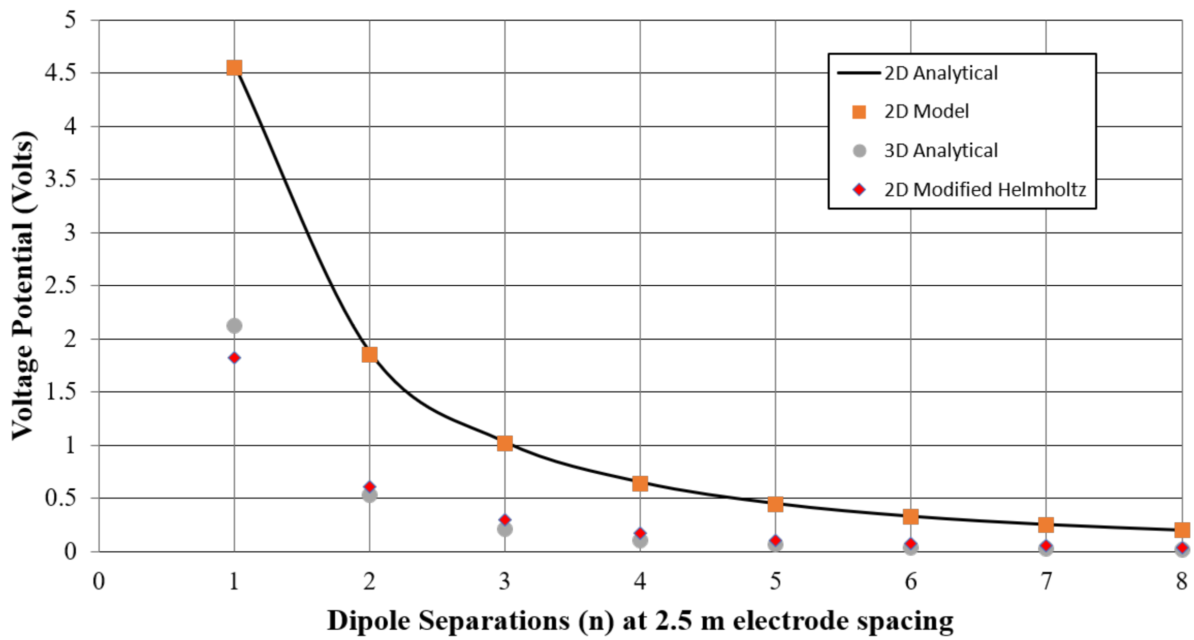

Figure 8.1: Analytical and numerical solutions of voltage potentials derived from 2D and 3D point sources.

Chapter 9

Scientific Contributions

This research presents three contributions all related to enhancing the ability to characterize groundwater systems with Electrical Resistivity Tomography. Each of the major contributions are described in detail below.

9.1 Conceptualizing Groundwater-Surface Water Interactions using ERT

A major limitation that exists in physically based models of gw-sw exchange is the lack of knowledge regarding the connectivity status between the surface water and groundwater. Monitoring wells screened adjacent to gw-sw systems are commonly used to infer connectivity regimes, however, they do no provide information about the region that has a direct-causative effect and gw-sw exchange fluxes. The results in Chapter 3 (Figures 3.6 - 3.9) and Chapter 4 (Figure 4.3 - Figure 4.5) shows that well designed ERT surveys can capture changes in electrical properties between the riverbed and groundwater table through space and time, which provides a fast and non-invasive way to decipher the connectivity status of the hydrologic system. This information is needed for accurate quantification of groundwater-surface fluxes. Consequently, the ability of hydrologic models to provide sound scientific information needed for groundwater management decisions is predicated on the accurate characterization of hydrogeoloic properties. The field and computation methods employed in this research contribute directly towards the increased understanding of gw-sw connectivity.

9.2 Analytic Element Modelling of Electrostatic Fields Across Sharp Electrical Interfaces

The Analytic Element method was adapted for the study of electrical conduction through uniform, layered, and heterogeneous soils through the computational methods developed by Steward and Allen (2013); Steward (2020a). Soil is represented by interconnected rectangular elements, each of which has specified electrical properties (i.e., electrical conductivity/resistivity, dielectric permittivity). An electric field is induced within the earth through a point sink and point source located at the top of the modelling domain. The electric potential and electric field distribtuion is solved for different geometric configurations of soils across varying levels of contrast in electrical properties. The robust mathematical capabilities of influence functions allows for the model to accurately solve for the electric potential and electric field where locally steep gradients exist. This is also true near a point source where sharp gradients in electric potential occur. The advantage of representing a soil layer with a simple geometry is the conceptualization of heterogeneous porous media as an assemblage of adjacent soil units, each with distinct soil properties. This in turn allows for a reduction in the unknown model parameters without comprising the numerical calculation of the forward response. Thus, this computational method eliminates the need for a regularization scheme that controls the spatial roughness of the model parameters. Additionally, finely discretized models refine meshes near the earth to achieve a numerically accurate solutions. As a result, they may fit data by adjusting the electrical properties near nodes that are not representative of the bulk soil within those regions. Finite element inversion schemes that are not adequately constrained may produce models whose responses achieve low RMSE values by adjustment of the electrical properties surrounding the potential measurements and point sources. The AEM differs in this sense as the domain is represented by distinct soil properties near the surface where measurements are relatively insensitive, eliminating the possible creation of surface anomalies in the recovered model.

Ultimately, the use of the AEM in the forward modelling of electrical resistivity inversion provides a more robust and physically realistic method to explicitly model the impact soil heterogeneity has on the forward response of different ERT array configurations.

9.3 Particle Swarm Optimization and the AEM in Geophysical Inversion

The AEM-PSO scheme developed in this research produces a pure mathematical response of the physical problem that is independent of model smoothness constraints. This is significant because smoothness constraints are user dependent choices that impact the recovered solutions. While regularization techniques are certainly necessary when a priori information is available (known geology), imposing such constraints on an unknown earth does not allow the solution to become data driven (assuming measurement noise is low). The search ability of the PSO scheme allows solutions to be generated from a complex parameter space without such an arbitrary starting model. The notion of Occam's Razor in geophysical inversion is well documented (Constable et al., 1987). In the context of resistivity models, it means that the most simple (smooth) resistivity model providing a response that fits the observed data within reason is the best or most likely model. Consequently, inversion schemes may shave away complex features necessitated by the data. Ultimately this global optimization scheme reconstructs an earth model that may be as simple or as complex as necessary. Ultimately, the development of this new computational method provides an analysis tool for the following questions associated with ERT:

- What is the appropriate depth of investigation metric?
- What is the optimal set of electrode configurations needed to detect subsurface heterogeneities?
- Can a global optimization schemes without regularization avoid over-fitting data?
- What level of hydrogelogic information can be directly inferred from the distribution of geophysical properties?

This is the first time the Analytic Element Method and Particle Swarm Optimization have been jointly applied to ERT. The mathematical basis that forms this joint scheme is given by the methods outlined in Chapter 5. The results of these methods are illustrated in Chapter 6 (Figure 6.1 - Figure 6.5) and Chapter 7 (Figure 7.2 - Figure 7.7). The numerical ability of the scheme to solve for the electric potential across hetergeneous domains, along with the ability of the PSO scheme to reconstruct adequate resistivity models demonstrates that this scheme can provide a sound hydrogeologic interpretation of ERT data. This will advance the ability of ERT methods to characterize hydrogeologic properties, and will improve the in-situ conceptualization of river-aquifer connectivity regimes.

Chapter 10

Conclusion

Electrical resistivity surveys conducted within the Arkansas River Valley revealed differences in groundwater-surface water connectivity patterns. The initial results of the field study in Chapters 3 and 4 show sharp changes in electrical properties beneath inundated portions of the riverbed. Supporting hydrologic was used to develop a hydrogeologic conceptualization of the system. The initial field work and discontinuous resistivity distributions observed beneath the Arkansas River motivated the extended analysis of alternative computational methods (AEM-PSO) to interpret ERT data in light of the pertinent hydrogeologic processes.

The Analytic Element Method (AEM) was used to calculate the electric potential and electric field distribution across rectangular soil elements of different size and electrical contrast. The model showed good performance in terms of its ability to match boundary and interface conditions across sharp changes in electrical properties over small spatial scales. The computational accuracy of the method is particularly beneficial for analyzing large potential gradients near points sources. One benefit of representing near surface regions with simple elements is the reduction in the number of parameters that need to be estimated by the inverse model. This in turn reduces the need for user dependent-regularization techniques that alter variation in the electrical resistivity. Rectangle size may be increased or decreased to sufficiently discretize the level of heterogeneity within the subsurface.

The continued development of PSO as a global optimization scheme has the potential to significantly advance the hydrogeologic interpretation of ERT surveys. An inertia weight particle swarm optimization scheme was utilized to reconstruct 1D-layered resistivity models from synthetic and field ERT datasets. Different objective functions were implemented within the PSO scheme, and recovered resistivity models showed a strong dependence upon the type of error metric employed. This is significant because it demonstrated that the commonly accepted norm used in the finite element method analysis of ERT, which is the established field interpretation method, uses a norm that is not the most effective in terms of reproducing field data. The inversion was able to distinguish lowly resistivie and highly resistivie layers used in the synthetic dataset, and reproduced an acceptable error levels for a perfect dataset. The model results generated from field data showed correlation to the known geology, but underestimated the resistivity values of those layers relative to the known geophysical properties. Further research needs to analyze the quasi 2D solution of electric potential so results can be compared with traditional geophysical simulation methods.

10.1 Future Work

The AEM-PSO scheme has the ability to broaden the knowledge within the field of Hydrogeophysics in the following areas:

- Optimizing ERT Arrays to Distinguish Subsurface Features
- Sensitivity Analysis of PSO performance on Objective Function Type
- Parallel Computing Environment for PSO
- Modification of AEM model as part of Optimization Scheme
- Inclusion of Surface Topography into Forward Model
- Fully Coupled Hydrological-Geophysical Model

Thus, the computational methodology and understanding of groundwater-surface water connectivity developed in this dissertation has the potential to further bridge hydrologic understanding of near surface groundwater fluxes with from near surface geophysical and hydrologic data.

Bibliography

Advanced Geosciences Inc AGI. *EarthImager 2D Resistivity and IP inversion Software Instruction Manual*. Advanced Geosciences Inc., Austin, TX, 2007.

T.R. Ahring and D.R. Steward. Groundwater Surface Water Interactions and the Role of Phreatophytes in Identifying Recharge Zones. *Hydrology and Earth System Sciences*, 16(11):4133–4142, 2012. doi: 10.5194/hess-16-4133-2012.

G. E. Archie. The electrical resistivity log as an aid in determing some reservoir characteristics. *Petroleum Transactions of AIME (Am. Inst. Metall. Eng)*, 146:54–62, 1942.

G.E. Archie. The Electrical Resistivity Log as an Aid in Determing Some Reservoir Characteristics, 1941.

R Arjwech, ME Everett, J-L Briaud, S Hurlebaus, Z Medina-Cetina, S Tucker, and N Yousefpour. Electrical resistivity imaging of unknown bridge foundations. *Near Surface Geophysics*, 11(6): 591–598, 2013.

ASTM. ASTM D2434-68 Standard Test Method for Permeability of Granular Soils (Constant Head), 2006.

Sarah Auvenshine. *Aquifer recharge and evapotranspiration from the rivers in western Kansas*. PhD thesis, 2018.

Mark Bakker and John L Nieber. Analytic element modeling of cylindrical drains and cylindrical inhomogeneities in steady two-dimensional unsaturated flow. *Vadose Zone Journal*, 3(3):1038–1049, 2004.

Andrew Binley, Lee D Slater, Melanie Fukes, and Giorgio Cassiani. Relationship between spectral induced polarization and hydraulic properties of saturated and unsaturated sandstone. *Water resources research*, 41(12), 2005.

Andrew Binley, Susan S. Hubbard, Johan A. Huisman, Andre Revil, David A. Robinson, Kamini Singha, , and Lee D. Slater. The emergence of hydrogeophysics for improved understanding of subsurface processes over multiple scales. *Water Resources Research*, 51:3837–3866, 2015.

Paul Bratley and Bennett L Fox. Algorithm 659: Implementing sobol's quasirandom sequence generator. *ACM Transactions on Mathematical Software (TOMS)*, 14(1):88–100, 1988.

RJ Brownbill, S Lamontagne, RM Williams, PG Cook, CT Simmons, and N Merrick. Interconnection of surface and groundwater systems–river losses from losing-disconnected streams. *Technical Final Report. NSW Office of Water*, 2011.

Philip Brunner, Peter G. Cook, and Craig T. Simmons. Hydrogeologic Controls on Disconnection Between Surface Water and Groundwater. *Water Resources Research*, 45, 2009. doi: 10.1029/2008WR006953.

Philip Brunner, René Therrien, Philippe Renard, Craig T Simmons, and Harrie-Jan Hendricks Franssen. Advances in understanding river-groundwater interactions. *Reviews of Geophysics*, 55(3):818–854, 2017.

Phillip Brunner, Peter G. Cook, and Craig T. Simmons. Disconnected Surface Water and Groundwater: From Theory to Practice. *Ground Water*, 49(4):460–467, 2011. doi: 10.1111/j.1745-6584.2010.00752.x.

JJ Butler and JM Healey. Performance and analysis of june 1998 slug tests at the deerfield and garden city monitoring sites. *Kansas Geological Survey Open-File Report*, (98-99), 1999.

Tianfeng Chai and Roland R Draxler. Root mean square error (rmse) or mean absolute error (mae)?–arguments against avoiding rmse in the literature. *Geoscientific model development*, 7(3):1247–1250, 2014.

Abhijit Chaudhuri, M Sekhar, Marc Descloitres, Y Godderis, Laurent Ruiz, and Jean-Jacques Braun. Constraining complex aquifer geometry with geophysics (2-d ert and mrs measurements) for stochastic modelling of groundwater flow. *Journal of Applied Geophysics*, 98:288–297, 2013.

Steven C Constable, Robert L Parker, and Catherine G Constable. Occam's inversion: A practical algorithm for generating smooth models from electromagnetic sounding data. *Geophysics*, 52 (3):289–300, 1987.

N. Crook, A. Binley., R. Knight, D.A. Robinson, J. Zarnetske, and R. Haggerty. Electrical resistivity imaging of the architecture of substream sediments. *Water Resources Research*, 44, 2008. doi: 10.1029/2008WR006968.

William Daily, Abelardo Ramirez, and Douglas LaBrecque. Electrical resistivity tomography of vadose zone water movement. *Water Resources Research*, pages 1429–1442, 1992. doi: 10.1029/91WR03087.

Catherine de Groot-Hedlin and Steven Constable. Inversion of magnetotelluric data for 2d structure with sharp resistivity contrasts. *Geophysics*, 69(1):78–86, 2004.

Constable deGroot Hedlin and Steven Constable. Occam's inversion to generate smooth, two-dimensional models from magnetotelluric data. *Geophysics*, 55(12):1613–1624, 1990.

Marc Descloitres, Laurent Ruiz, Muddu Sekhar, Anatoly Legchenko, Jean-Jacques Braun, MS Mohan Kumar, and S Subramanian. Characterization of seasonal local recharge using electrical resistivity tomography and magnetic resonance sounding. *Hydrological Processes: An International Journal*, 22(3):384–394, 2008.

Claude Doussan and Stéphane Ruy. Prediction of unsaturated soil hydraulic conductivity with electrical conductivity. *Water Resources Research*, 45(10), 2009.

John Dunbar, Joseph White, Ram Neupane, Tian Xu, June Wolfe, and Jeff Arnold. Characterizing a Shallow Groundwater System beneath Irrigated Sugarcane with Electrical Resistivity and Randon, Puunene, Hawaii. *Journal of Environmental and Engineering Geophysics*, 20(2):165–181, 2015. doi: 10.2113/JEEG20.2.165.

Russell Eberhart and James Kennedy. A new optimizer using particle swarm theory. In *MHS'95. Proceedings of the Sixth International Symposium on Micro Machine and Human Science*, pages 39–43. Ieee, 1995.

LS Edwards. A modified pseudosection for resistivity and ip. *Geophysics*, 42(5):1020–1036, 1977.

Mark E. Everett. *Near-Surface Applied Geophysics*. Cambridge University Press, 2013.

Alex Furman, A.W. Warrick, and Ty P.A. Ferre. Electrical potential distributions in a heterogeneous subsurface in response to applied current. *Vadose Zone Journal*, 1:273–280, 2002.

Alex Furman, Ty Ferré, and Art W Warrick. Optimization of ert surveys for monitoring transient hydrological events using perturbation sensitivity and genetic algorithms. *Vadose Zone Journal*, 3(4):1230–1239, 2004.

Alex Furman, Ty P Ferré, and Gail L Heath. Spatial focusing of electrical resistivity surveys considering geologic and hydrologic layering. *Geophysics*, 72(2):F65–F73, 2007.

Shishir Gaur, Bhagu Ram Chahar, and Didier Graillot. Analytic elements method and particle swarm optimization based simulation–optimization model for groundwater management. *Journal of hydrology*, 402(3-4):217–227, 2011.

Paul W.J. Glover. Archie's law - a reappraisal. *Solid Earth*, 7:1157–1169, July 2016.

A Godio and A Santilano. On the optimization of electromagnetic geophysical data: Application of the pso algorithm. *Journal of Applied Geophysics*, 148:163–174, 2018.

Mark S Greenhalgh. *DC resistivity modelling and sensitivity analysis in anisotropic media.* PhD thesis, 2009.

A.K. Greve, H. Roshan, B.F.J Kelly, and R.I. Acworth. Electrical conductivity of partially saturated porous media containing clay: An improved formulation. *Journal of Geophysial Research: Solid Earth*, 118:3297–3303, 2013.

Thomas Günther and Carsten Rücker. Boundless electrical resistivity tomography bert 2–the user tutorial, 2015.

Thomas Günther, Carsten Rücker, and Klaus Spitzer. Three-dimensional modelling and inversion of dc resistivity data incorporating topography—ii. inversion. *Geophysical Journal International*, 166(2):506–517, 2006.

E.D Gutentag, Frederick J. Heimes, Noel C. Krothe, Richard R. Luckey, and John B. Weeks. Geohydrology of the High Plains Aquifer in Parts of Colorado, Kansas, Nebraska, New Mexico, Oklahoma, South Dakota, Texas, and Wyoming. Technical report, United States Geological Survey, 1984.

Hendrik M. Haitjema, D. T. Feinstein, Randy J. Hunt, and Maksym A. Gusyev. A hybrid finite-difference and analytic element groundwater model. *Ground Water*, 48(4):538–548, July-August 2010. doi: 10.1111/j.1745-6584.2009.00672.x.

Henk Haitjema, Vic Kelson, and Wim de Lange. Selecting modflow cell sizes for accurate flow fields. *Groundwater*, 39(6):931–938, 2001.

Henk M Haitjema. *Analytic element modeling of groundwater flow*. Elsevier, 1995.

Randall J Hunt. Ground water modeling applications using the analytic element method. *Groundwater*, 44(1):5–15, 2006.

Md Zahidul Karim and Stacey E Tucker-Kulesza. Predicting soil erodibility using electrical resistivity tomography. *Journal of Geotechnical and Geoenvironmental Engineering*, 144(4): 04018012, 2018.

Avneet Kaur and Mandeep Kaur. Dealing with boundary constraint violations in particle swarm optimization with aging leader and challengers (alc-pso). *International Journal of Computer Applications*, 121(11), 2015.

George Vernon Keller and Frank C Frischknecht. Electrical methods in geophysical prospecting. 1966.

Andreas Kemna, Jan Vanderborght, Bernd Kulessa, and Harry Vereecken. Imaging and characterisation of subsurface solute transport using electrical resistivity tomography (ert) and equivalent transport models. *Journal of Hydrology*, 267(3-4):125–146, 2002.

Weston J Koehn, Stacey E Tucker-Kulesza, and David R Steward. Conceptualizing groundwater-surface water interactions within the ogallala aquifer region using electrical resistivity imaging. *Journal of Environmental and Engineering Geophysics*, 24(2):185–199, 2019.

Abhishes Lamsal, Stephen M Welch, Jeffrey W White, Kelly R Thorp, and Nora Bello. Problems with estimating anthesis phenology parameters in zea mays: Consequences for combining ecophysiological models with genetics. *bioRxiv*, page 087742, 2016.

Hamed Layssi, Pouria Ghods, Aali R Alizadeh, and Mustafa Salehi. Electrical resistivity of concrete. *Concrete International*, 37(5):41–46, 2015.

M.H. Loke. *Tutorial: 2-D and 3-D Electical Imaging Surveys*, 2011.

M.H. Loke, Ian Acworth, and Torleif Dahlin. A Comparison of Smooth and Blocky Inversion Methods in 2D Electrical Imaging Surveys. *Exploration Geophysics*, 34(3):182–187, 2003. doi: 10.1071/EG03182.

M.H. Loke, J.E. Chamber, D.F. Rucker, O. Kuras, and P.B. Wilkinson. Recent Developments in the Direct-Current Geoelectrical Imaging Method. *Journal of Applied Geophysics*, 95:135–156, 2013. doi: 10.1016/j.jappgeo.2013.02.017.

Peter R Mcgillivray and DW Oldenburg. Methods for calculating fréchet derivatives and sensitivities for the non-linear inverse problem: A comparative study 1. *Geophysical prospecting*, 38(5): 499–524, 1990.

Peter Robert McGillivray. *Forward modeling and inversion of DC resistivity and MMR data*. PhD thesis, University of British Columbia, 1992.

AJ Merritt, JE Chambers, W Murphy, PB Wilkinson, LJ West, DA Gunn, PI Meldrum, M Kirkham, and N Dixon. 3d ground model development for an active landslide in lias mudrocks using geophysical, remote sensing and geotechnical methods. *Landslides*, 11(4):537–550, 2014.

James Kenneth Mitchell, Kenichi Soga, et al. *Fundamentals of soil behavior*, volume 3. John Wiley & Sons Hoboken, NJ, 2005.

Parry Moon and Domina Eberle Spencer. Field theory for engineers. *American Journal of Physics*, 29(10):717–717, 1961.

John R. Nimmo, Richard W. Healy, and David A. Stonestrom. Aquifer rechare. Technical report, United States Geological Survey, 2006.

J.E. Nyquist, P.A. Freyer, and L. Toran. Stream Bottom Resistivity to Map Ground Water Discharge. *Groundwater*, 46(4):561–569, 2008. doi: 10.1111/j.1745-6584.2008.00432.x.

Richard Ogilvy, Philip Meldrum, Jon Chambers, and Geoffrey Williams. The use of 3d electrical resistivity tomography to characterise waste and leachate distribution within a closed landfill, thriplow, uk. *Journal of Environmental & Engineering Geophysics*, 7(1):11–18, 2002.

Douglas W Oldenburg and Yaoguo Li. Estimating depth of investigation in dc resistivity and ip surveys. *Geophysics*, 64(2):403–416, 1999.

Ender Ozcan and Chilukuri K Mohan. Analysis of a simple particle swarm optimization system. *Intelligent engineering systems through artificial neural networks*, 8:253–258, 1998.

GJ Palacky. Clay mapping using electromagnetic methods. *First Break*, 5(8):295–306, 1987.

Millie Pant, Radha Thangaraj, Crina Grosan, and Ajith Abraham. Improved particle swarm optimization with low-discrepancy sequences. In *2008 IEEE Congress on Evolutionary Computation (IEEE World Congress on Computational Intelligence)*, pages 3011–3018. IEEE, 2008.

Ertan Pekşen, Türker Yas, and Alper Kıyak. 1-d dc resistivity modeling and interpretation in anisotropic media using particle swarm optimization. *Pure and Applied Geophysics*, 171(9): 2371–2389, 2014.

TE Peterson. Eliminating gibb's effect from separation of variables solutions. *SIAM review*, 40(2): 324–326, 1998.

Riccardo Poli, James Kennedy, and Tim Blackwell. Particle swarm optimization. *Swarm intelligence*, 1(1):33–57, 2007.

A. J. Pullan. The quasilinear approximation for unsaturated porous media flow. *Water Resources Research*, 26(6):1219–1234, June 1990. doi: 10.1029/WR026i006p01219.

AE Reisenauer. Methods for solving problems of multidimensional, partially saturated steady flow in soils. *Journal of Geophysical Research*, 68(20):5725–5733, 1963.

A Revil and Nicolas Florsch. Determination of permeability from spectral induced polarization in granular media. *Geophysical Journal International*, 181(3):1480–1498, 2010.

DA Robinson, Andrew Binley, N Crook, FD Day-Lewis, TPA Ferré, VJS Grauch, R Knight, M Knoll, V Lakshmi, R Miller, et al. Advancing process-based watershed hydrological research using near-surface geophysics: A vision for, and review of, electrical and magnetic geophysical methods. *Hydrological Processes: An International Journal*, 22(18):3604–3635, 2008.

A Roy and A Apparao. Depth of investigation in direct current methods. *Geophysics*, 36(5): 943–959, 1971.

Carsten Rücker, Thomas Günther, and Klaus Spitzer. Three-dimensional modelling and inversion of dc resistivity data incorporating topography—i. modelling. *Geophysical Journal International*, 166(2):495–505, 2006.

D. Rucker. A Coupled Electrical Resistivity-Infiltration Model for Wetting Front Evaluation. *Vadose Zone Journal*, 8(2):383–388, 2009. doi: doi:10.2136/vzj2008.0080.

Benjamin F. Schwartz and Madeline E. Schreiber. Quantifying Potential recharge in Mantled Sinkholes Using ERT. *Groundwater*, 47(3):370–381, 2009. doi: 10.1111/j.1745-6584.2008.00505.x.

Christoph Schwarzbach, Ralph-Uwe Börner, and Klaus Spitzer. Two-dimensional inversion of direct current resistivity data using a parallel, multi-objective genetic algorithm. *Geophysical Journal International*, 162(3):685–695, 2005.

Mrinal K Sen and Paul L Stoffa. *Global optimization methods in geophysical inversion*. Cambridge University Press, 2013.

Margaret Shanafield, Peter G Cook, Philip Brunner, James McCallum, and Craig T Simmons. Aquifer response to surface water transience in disconnected streams. *Water Resources Research*, 48(11), 2012.

P. Sharma. *Environmental and Engineering Geophysics*. Cambridge University Press, 1997.

Ranjit Shaw and Shalivahan Srivastava. Particle swarm optimization: A new tool to invert geophysical data. *Geophysics*, 72(2):F75–F83, 2007.

Yuhui Shi and Russell Eberhart. A modified particle swarm optimizer. In *1998 IEEE international conference on evolutionary computation proceedings. IEEE world congress on computational intelligence (Cat. No. 98TH8360)*, pages 69–73. IEEE, 1998.

Lee Slater. Near Surface Electrical Characterization of Hydraulic Conductivity: From Petrophysical Properties to Aquifer Geometries - A Review. *Surveys in Geophysics*, 28:169–197, 2007. doi: 10.1007/s10712-007-9022-y.

Lee Slater and David P. Lesmes. Electrical-Hydraulic Relationships Observed for Unconsolidated Sediments. *Water Resources Research*, 38(10), 2002. doi: 10.1029/2001WR001075.

Lee Slater, Warren Barrash, Jeanette Montrey, and Andrew Binley. Electrical-Hydraulic Relationships Observed for Unconsolidated Sediments in the Presences of a Cobble Framework. *Water Resources Research*, 50(7):5721–5742, 2014. doi: 10.1002/2013WR014631.

Marios Sophocleous. Interactions Between Groundwater and Surface Water: The State of the Science. *Hydrogeology Journal*, 10:52–57, 2002. doi: 10.1007/s10040-001-0170-8.

Marios Sophocleous. Groundwater Recharge and Sustainability in the High Plans aquifer in Kansas, USA. *Hydrogeology Journal*, 13(2):351–365, 2005. doi: 10.1007/s10040-004-0385-6.

ASTM Standard. D2487-11. *Standard Practice for Classification of Soils for Engineering Purposes (Unified Soil Classification System), ASTM International, West Conshohocken, PA*, 2011.

Steward, Bruss D. R., X. P. J., Yang, S. A. Staggenborg, S. M. Welch, and M. D. Apley. Tapping Unsustainable Groundwater Stores for Agricultural Production in the High Plains Aquifer of Kansas, Projections to 2110. *Proceedings of the National Academy of Sciences of the United States of America,*, 110(37), 2013. doi: 10.1073/pnas.1220351110.

David R. Steward. Analysis of discontinuities across thin inhomogeneities, groundwater/surface water interactions in river networks, and circulation about slender bodies using slit elements in the Analytic Element Method. *Water Resources Research*, 51(11):8684–8703, November 2015. doi: 10.1002/2015WR017526.

David R. Steward. Analysis of vadose zone inhomogeneity towards distinguishing recharge rates: Solving the nonlinear interface problem with newton method. *Water Resources Research*, 52 (11), 2016. doi: 10.1002/2016WR019222.

David R Steward. Wave resonance and dissipation in collections of partially reflecting vertical cylinders. *Journal of Waterway, Port, Coastal, and Ocean Engineering*, 144(4):04018004, 2018.

David R. Steward. *Analytic Element Method: Complex Interactions of Boundaries and Interfaces*. Oxford University Press, 2020a.

David R. Steward. Waves in collections of circular shoals and bathymetric depressions. *Journal of Waterways, Ports, Coastal, and Ocean Engineering (ASCE)*, forthcoming:1–, 2020b. doi: 10.1061/(ASCE)WW.1943-5460.0000570.

David R Steward, X Yang, SY Lauwo, Scott A Staggenborg, GL Macpherson, and Stephen M Welch. From precipitation to groundwater baseflow in a native prairie ecosystem: a regional study of the konza lter in the flint hills of kansas, usa. *Hydrology and Earth System Sciences*, 15 (10):3181–3194, 2011.

D.R. Steward and A.J. Allen. The analytic element method for rectangular gridded domains, benchmark comparisons and application to the high plains aquifer. *Advances in Water Resources*, 60: 83–99, 2013.

D.R. Steward and A.J. Allen. Peak Groundwater Depletion in the High Plains Aquifer, Projections from 1930 to 2110. *Agricultural Water Management*, 170:36–48, 2016. doi: 10.1016/j.agwat.2015.10.003.

Otto DL Strack. Theory and applications of the analytic element method. *Reviews of Geophysics*, 41(2), 2003.

A Tikhonov and V Arsenin. Solutions of ill-posed problems (winston, washington, dc). *Multiscale decomposition of velocity structure and application to first-arrival travel-time tomography*, 1977.

Stacey Tucker-Kulesza, Cassandra Rutherford, and Michelle Bernhardt-Barry. Electrical resistivity at internal erosion locations in levees. *ISSMGE International Journal of Geoengineering Case Histories*, 5(2):55–69, 2019.

Monroe H Waxman, LJM Smits, et al. Electrical conductivities in oil-bearing shaly sands. *Society of Petroleum Engineers Journal*, 8(02):107–122, 1968.

D.O. Whittemore. Water Quality of the Arkansas River in Southwest Kansas. Technical report, Kansas Geological Survey, 2000.

D.O Whittemore. Ground-Water Recharge in the Upper Arkansas River Corridor in Southwest Kansas. Technical report, Kansas Geological Survey, 2002.

DO Whittemore, DP Young, and JM Healey. Multi-level observation well sites of the upper arkansas river corridor study: Kansas geol. *Survey Open-File Report*, 42:59, 2000.

Donald O. Whittemore. Hydrologic responses to pumping in the upper arkansas basin and effects of the conservation reserve enhancement program. Technical report, Kansas Geological Survey, 2007.

Paul B Wilkinson, Meng Heng Loke, Philip I Meldrum, Jonathan E Chambers, Oliver Kuras, David A Gunn, and Richard D Ogilvy. Practical aspects of applied optimized survey design for electrical resistivity tomography. *Geophysical Journal International*, 189(1):428–440, 2012.

Cort J Willmott and Kenji Matsuura. Advantages of the mean absolute error (mae) over the root mean square error (rmse) in assessing average model performance. *Climate research*, 30(1): 79–82, 2005.

Yang Xian, Menggui Jin, Yanfeng Liu, and Aonan Si. Impact of lateral flow on the transition from connected to disconnected stream–aquifer systems. *Journal of hydrology*, 548:353–367, 2017.

Yueqing Xie, Peter G Cook, Philip Brunner, Dylan J Irvine, and Craig T Simmons. When can inverted water tables occur beneath streams? *Groundwater*, 52(5):769–774, 2014.

D.P Young, D.O Whittemore, J.L. Grauer, and J.M. Witmer. Lithologic Characterization of Unconsolidated Deposits along the Arkansas River Corridor in Southwest Kansas. Technical report, Kansas Geological Survey, 2000.